REPORT DOCUMENTATION PAGE

1. REPORT DATE (DD-MM-YYYY)	2. REPORT TYPE	3. DATES COVERED (From - To)
29-10-2010	Final technical (USC 53-4514-1073)	01/01/2009–30/09/2010

4. TITLE AND SUBTITLE	5a. CONTRACT NUMBER
The Near Wake of Bluff Bodies in Stratified Fluids and the Emergence of Late Wake Characteristics	N00014-06-1-1073

5b. GRANT NUMBER

5c. PROGRAM ELEMENT NUMBER

6. AUTHOR(S)	5d. PROJECT NUMBER
Julian Andrzej Domaradzki, Principal Investigator	

5e. TASK NUMBER

5f. WORK UNIT NUMBER

7. PERFORMING ORGANIZATION NAME(S) AND ADDRESS(ES)	8. PERFORMING ORGANIZATION REPORT NUMBER
Department of Aerospace and Mechanical Engineering University of Southern California 854 W. 36th Pl, RRB 101 Los Angeles, CA 90089-1191	

9. SPONSORING / MONITORING AGENCY NAME(S) AND ADDRESS(ES)	10. SPONSOR/MONITOR'S ACRONYM(S)
Office of Naval Research Regional Office San Diego 4520 Executive Dr., Suite 300 San Diego, CA 92121-3019	
	11. SPONSOR/MONITOR'S REPORT NUMBER(S)

12. DISTRIBUTION / AVAILABILITY STATEMENT

Approved for public release; distribution unlimited

20101112020

13. SUPPLEMENTARY NOTES

14. ABSTRACT

The primary goal of our work was to provide accurate information about velocity and density field in the near wake region of a flow around a sphere in a stratified fluid. This is a canonical configuration used in investigating a structure of stratified wakes in experiments and in numerical simulations. One of the difficulties in comparing results of numerical simulations with experiments is lack of detailed information about near wake that is needed to initialize simulations. Despite importance of this configuration it appears that only one numerical investigation has been performed that contains an actual sphere in the computational domain (Hanazaki, 1988). However, the simulated flow in that work is at low Reynolds number (Re=200), well below turbulent regime. Our research work was designed to fill this gap and to provide additional information useful for numerical simulations, turbulence modelling, and the interpretation of some experimental techniques.

15. SUBJECT TERMS

Stratified Wake; Numerical Simulations; Flow Around a Sphere

16. SECURITY CLASSIFICATION OF:			17. LIMITATION OF ABSTRACT	18. NUMBER OF PAGES	19a. NAME OF RESPONSIBLE PERSON J.A. Domaradzki
a. REPORT	b. ABSTRACT	c. THIS PAGE			19b. TELEPHONE NUMBER (include area code)
Unclassified	Unclassified	Unclassified		101	(213) 740-5357

The Near Wake of Bluff Bodies in Stratified Fluids and the Emergence of Late Wake Characteristics

J.A. Domaradzki
Department of Aerospace and Mechanical Engineering
University of Southern California
Los Angeles, CA 90089-1191

October 29, 2010

1

The primary goal of our work was to provide accurate information about velocity and density field in the near wake region of a flow around a sphere in a stratified fluid. This is a canonical configuration used in investigating a structure of stratified wakes in experiments (e.g., Spedding et al. 1997, 2001, 2002) and in numerical simulations (e.g., Dommermuth et al. (2002), Diamessis et al. (2005), Brucker and Sarkar (2009)). One of the difficulties in comparing results of numerical simulations with experiments is lack of detailed information about near wake that is needed to initialize simulations. Despite importance of this configuration it appears that only one numerical investigation has been performed that contains an actual sphere in the computational domain (Hanazaki, 1988). However, the simulated flow in that work is at low Reynolds number (Re=200), well below turbulent regime. Our research work was designed to fill this gap and to provide additional information useful for numerical simulations, turbulence modelling, and the interpretation of some experimental techniques.

1   Summary of Research Activities

The computations in the project were supervised by Prof. J.A. Domaradzki. A PhD student in the AME department, Trevor Orr, has worked on the project full time; this is the topic of his Ph.D. Thesis, with Qualifying Exam passed in September 2010. We have established collaboration with Prof. George Constantinescu and acquired a serial code for simulating a flow around a sphere in curvilinear coordinates using detached eddy simulations (DES) approach. The code was first implemented and tested for the flow without stratification. Subsequently, it has been modified to include effects of stratification, again in the framework of DES. Since the modified code already contained turbulence model we were able to move directly to simulating flows at experimental Reynolds numbers where comparisons with a single existing dataset of Spedding for a near wake are possible (Re=5000). The numerical results for the mean wake velocity were found to be in good agreement with experiments but rms velocities showed poor agreement. The initial hypothesis was that observed results for rms velocities were caused by internal waves reflecting from the computational boundaries. To decrease this effect various numerical absorbing layers were implemented and tested but no significant improvement has been observed. We undertook a systematic analysis of possible origins of the rms turbulent kinetic energy build up in the DES simulations for stratified wake: is it caused by numerical resolution?; by the turbulence model?; by the boundary conditions?; by stratification and internal waves? To increase the numerical resolution a parallel version of the code has been implemented on the USC Linux cluster. To determine the influence of the model we have initiated DNS runs (without a model) for a stratified case. To determine the effects of boundary conditions we have initiated DNS and DES for an unstratified case. The results for stratified flow cases for Re=200 and Fd= 0.125 and 0.250 compare very well with Hanazaki (1988); for unstratified flow cases for Re=300 we obtain a good comparison with Johnson and Patel (1999). All relevant results are summarized in a separate section below.

During the duration of the project PI was involved in additional, related research with

2

unsupported Ph.D. student on subject of LES modeling. The relevant paper (attached) acknowledges partial ONR support for that work. Another invited review paper, currently in print, on subject of LES modeling without eddy viscosity models also acknowledges ONR support and is attached.

2 Publications/Presentations during the duration of the Contract

1. T. Tantikul and J.A. Domaradzki, " Large Eddy Simulations Using Truncated Navier-Stokes Equations with the Automatic Filtering Criterion", J. Turbulence **11**, 1-24 (2010).

2. J.A. Domaradzki, "Large eddy simulations without explicit eddy viscosity models", invited review for Int. J. Comp. Fluid Dyn., in print (2010).

3. T.S. Orr, J.A. Domaradzki, and G.S. Contantinescu, "Detached Eddy Simulation of Separated Flow in the Near-Wake of a Sphere Moving Through a Stratified Fluid", *Bull. Am. Phys. Soc.* **54**, 208 (2009).

3 Research Personnel

1. J.A. Domaradzki (Principal Investigator), Professor, Department of Aerospace and Mechanical Engineering, University of Southern California, Los Angeles, CA 90089-1191. Dates supported: 01/01/2009-30/09/2010.

2. Trevor Orr, Ph.D. Student, Department of Aerospace and Mechanical Engineering, University of Southern California, Los Angeles, CA 90089-1191. Dates supported: 01/01/2009-30/09/2010.

Degrees Granted: None

Honors/Awards/Promotions: None

4 Research Results

This section consists of Trevor Orr's Ph.D. Proposal and journal papers which provide detailed information about research results summarized above.

Dissertation Proposal

Proposal for Qualifying Exam

Trevor Orr

Department of Aerospace & Mechanical Engineering
University of Southern California

Chapter 1

Introduction and Background

1.1 Introduction

1.1.1 A Description of the Physical Problem

The physical problem involves the numerical modeling of a sphere traveling horizontally through a stable, linearly stratified fluid of constant density gradient at moderate Reynolds (Re) numbers for a range of Froude (Fd) numbers. The investigation will study the effects seen by the presence of stratification in both laminar (low to moderate Re) and turbulent (moderate to high Re) regimes, but sphere motion at very low speeds (creeping flow) is not included in this work.

Investigation of behavior of the flow around a body in a stratified fluid is of interest to engineering applications as well as some flows at the geophysical scale; flows over mountain ridges for instance. Engineering applications may involve flow around a submarine. Because the applications of these flows are quite varied, there are so-called canonical geometries which aid computational modelers in verifying the behavior of the computational models. The sphere is generally accepted to be one of these canonical problems because of its simple geometric shape as it contains a perfect symmetry about its center point.

Flow around a submersed object in a stably stratified fluid has several physical features that are not found in a similar flow without density stratification; i.e. a homogeneous flow. This is because of restorative buoyancy forces within the fluid that return any disturbances in the stratification profile to its previously undisturbed, "at rest," condition.

1.1.2 The Governing Equations

Equations of motion and assumptions

The problem of the sphere traveling horizontally through a continuously stratified fluid is governed by a particular set of the Navier-Stokes equations of motion and the equation of continuity:

$$\left[\frac{\partial \rho u_i}{\partial t} + \frac{\partial \rho u_i u_j}{\partial x_j} + \frac{\partial P}{\partial x_i} + f_i - \mu \frac{\partial^2 u_i}{\partial x_j^2} \right] \vec{e}_i = 0, \quad f_i = \rho g \delta_{i3} \tag{1.1}$$

$$\frac{\partial \rho}{\partial t} + \frac{\partial \rho u_i}{\partial x_i} = 0 \tag{1.2}$$

where $\vec{e}_i$ represents the orthnormal coordinate vectors in a Cartesian coordinate system, $\vec{u} = u_i \vec{e}_i$ is the velocity vector field, P is pressure, ρ is the density, and f_i is the component of body forcing due to gravity acting on individual fluid particles per unit volume.

It is desirable to decompose both the pressure and density field:

$$\rho(\vec{x}, t) = \rho_0 + \rho(z) + \rho'(\vec{x}, t) \tag{1.3}$$

$$P(\vec{x}, t) = P_0 + P(z) + p'(\vec{x}, t) \tag{1.4}$$

This decomposition uses the concept of hydrostatic balance between a background pressure, $p(z)$, and a background density distribution, $\rho(z)$. Physically, this translates into a balance between the gravity force acting on a fluid particle and the restoring buoyancy forces exerted by any surrounding fluid particles while the fluid is at rest such that only disturbances to this equilibrium exhibit any net effect. Mathematically, the hydrostatic balance aids in the proper construction of boundary conditions, especially in fluids of infinite depth. Without the hydrostatic balance, the pressure conditions must be explicitly set at the boundaries. The primed quantities P' and ρ' are referred to as the perturbation pressure and perturbation density, respectively.

The equation of continuity, Eq. 1.2, enforces the conservation of mass. The Boussinessq approximation is used [26]. This assumes that any changes in density are only accounted for in the body forcing term. In addition, any effect of a fluid particles' density change on the equation of continuity is negligible and leaves the continuity equation as stating that the velocity field is divergence free.

Substituting the two ideas above into the Eqs. 1.1 and 1.2:

$$\left[\frac{\partial u_i}{\partial t} + u_j \frac{\partial u_i}{\partial x_j} + \frac{\partial p'}{\partial x_i} - \frac{\mu}{\rho_0} \frac{\partial^2 u_i}{\partial x_j^2} \right] \vec{e}_i + \left(\frac{\rho' g}{\rho_0} \right) \vec{e}_3 = 0 \tag{1.5}$$

$$\frac{\partial u_i}{\partial x_i} = 0 \tag{1.6}$$

An equation must also be presented for evolution of the perturbation density quantity. As stated by Kundu, an equation for the description of the density perturbations is provided by the concept of incompressibility (e.g. Kundu pg. 248 [26]); with the current formulation containing dissipative effects. The equation for the convection of density perturbations, known as "the density equation" becomes:

$$\frac{\partial \rho'}{\partial t} + u_j \frac{\partial \rho'}{\partial x_j} + u_3 - \kappa \frac{\partial^2 \rho'}{\partial x_j^2} = 0 \tag{1.7}$$

where κ is the molecular diffusion coefficient.

Non-dimensionalization of the governing equations

It is beneficial to complete a non-dimensionalization of the governing equations to distill the physics of the problem into a problem controlled by parameters of similtude. Non-dimensionalized quantities within this section will be denoted by an asterik (*); which will be dropped after this section for aesthetics of the recast equations. The diameter of the sphere, D, the speed of the sphere, U, the characteristic density, ρ_0, and the background density stratification, $\partial \rho(z)/\partial z$, are intuitive choices for the characteristic quantities of the problem. Recasting Eqs. (1.5) and (1.6) in non-dimensional form:

2

$$\left[\frac{\partial u_i^*}{\partial t^*} + u_j^* \frac{\partial u_i^*}{\partial x_j^*} + \frac{\partial p^{'*}}{\partial x_i^*} - \frac{1}{Re} \frac{\partial^2 u_i^*}{\partial x_j^{*2}} \right] \vec{e}_i + \left[\frac{\rho^{'*}}{Fd^2} \right] \vec{e}_3 = 0 \tag{1.8}$$

$$\frac{\partial u_i^*}{\partial x_i^*} = 0 \tag{1.9}$$

$$\frac{\partial \rho^{'*}}{\partial t^*} + u_j^* \frac{\partial \rho^{'*}}{\partial x_j^*} - u_3^* - \frac{1}{Pe} \frac{\partial^2 \rho^{'*}}{\partial x_j^{*2}} = 0 \tag{1.10}$$

where $t^* = Ut/D$, $\vec{x}^* = \vec{x}/D$, $\vec{u}^* = \vec{u}/U$, $p^{'*} = p'/\rho_0 U^2$, $\rho^{'*} = \rho' / \left[-D\, \partial\rho(z)/\partial z \right]$, $Re = DU/\nu$, $Fd = U/(ND)$, $Sc = \kappa/\nu$, and $Pe = 1/ScRe$ have been used as non-dimensionalization parameters.

Here, $N(z)^2 = \left[-\partial\rho(z)/\partial z \right] g/\rho_0$ is the Brunt-Väisälä frequency. In this study, the density stratification is continuous and linear in undisturbed conditions, resulting in $N(z) = N = $ constant, but no generality has been lost in the governing equations. Through non-dimensionalization, if the Schmidt number is taken to be unity, it is apparent that Eqs. (1.8)-(1.10) are controlled by the parameter of the Froude and Reynolds number.

1.1.3 Stratified Fluids

The fluid may be a liquid or gas of a varying density where the continuum approximation is a valid assumption. If an infinite-in-the-horizontal volume of stationary fluid is positioned directly above a second similarly constructed volume of fluid, and the density of the fluid in the first volume is less than that contained in the second, and this pattern is repeated for all layers in the vertical, then the fluid may be considered stably stratified. A stable, continuously stratified fluid is the occurrence where these stacked layers become infinitesimally thin in the vertical direction, and the density gradient of the stratification maintains the stable condition for all these layers.

The density gradient of the stratification is embodied within the so-called Brunt-Väisälä frequency which is commonly denoted as $N(z)$. Physically, the Brunt-Väisälä frequency represents the frequency at which a fluid particle that has been vertically displaced by some amount will oscillate about its original equilibrium state. As the stratification gradient of the continuously stratified fluid becomes increasingly severe, the Brunt-Väisälä frequency increases proportionally to the value of the local density gradient. For the steady motions of submersed bodies, the Froude number becomes the analogue of the Brunt-Väisälä frequency , and as the Froude number decreases, the stratification of the fluid becomes increasingly severe.

In low enough Froude number flows, a unique effect of stratification (excluding creeping flow) is referred to as the "blocking phenomenon." The blocking phenomenon is not a primary focus of this work but may be encountered for some flows contained within this investigation and mention of the physics of these flows is prudent. The blocking phenomenon is a result of the flow lacking enough kinetic energy to convert into the potential energy required to move vertically over a submersed obstacle. In two-dimensional flows, the effect of this energy deficit is that fluid particles are trapped on the upwind side of the object and are forced to move in unison with the obstacle's motion. The fluid behaving in this fashion is referred to as "blocked." In three-dimensional flows, the fluid has the ability to flow around the sides of the object if there is not enough kinetic energy to overcome the potential energy required to move over the object, but even in this case some blocking effects

may still be seen in some planes of symmetry. A review article by Baines in 1987 [2] provides a review into the topic of the blocking phenomena.

As the Froude number increases, the effects of stratification become less apparent, the Brunt-Väisälä frequency decreases, and as the Froude number approaches the infinite limit, the flow behaves as a homogeneous fluid flow.

1.2   Stratified Flow Around a Sphere

A submersed body is assumed to be in a steady non-oscillatory motion. References to the flow around the body indicate that the observer's reference frame is fixed with respect to the body as it moves through a stationary fluid, and variances to this convention are otherwise noted. References to "the sphere" are intended to reference the sphere traveling horizontally through the linearly stratified fluid at a constant speed. Flows that maintain an orderly, predictable behavior insensitive to perturbations or initial conditions are called laminar. Flows that do not maintain these properties are generally referred to as turbulent; although there is no universally accepted definition of turbulence. A sketch of the physical problem is seen in Figure 4.1.

1.2.1   Behavior of Flow Around the Sphere

The first region of physical interest is the behavior of the flow around the body, including the flow close to the surface of the sphere. Early focus on the flow upwind and around a submersed obstacle in a stratified fluid is typified by the flow over mountains or hill-shaped objects, especially in some of the earliest work on the topic. Although physically focused on a geophysical problem, these studies are typically intended to describe the behavior of fluid particles as they approach and eventually attempt to flow around a submersed obstacle, which is analogous to the flow of fluid particles around the sphere. Attempts to quantify the ability of fluid particles to traverse an obstacle is discussed by Sheppard 1956 [43] by considering energy arguments. The efforts of Drazin 1961 [17] attempt to resolve the question of whether a fluid particle will flow over or around a three-dimensional object. A review of the various attempts to quantify and refine the theories presented by [43] and [17] are discussed in Hanazaki 1988 [21]. The relevant summaries to these works as applied to the sphere case is that fluid particles in the region affected by the presence of the sphere gain a directional preference as to whether they will flow over or around the side of the sphere because of the addition of the buoyancy forcing due to gravity. The further away from the sphere's region of influence, the less this preferred-direction effect is seen and the free stream motions of the fluid are generally considered to be unaffected. Thus, the flow around the sphere is mainly concerned with particle paths. The behavior of these particle paths becomes more effected by the presence of the sphere the closer the flow advects the particles to the sphere surface.

Within this region close to the sphere, the fluid particles on the surface of the sphere are assumed to be "stuck" to the surface and cannot be advected away from the surface. This is referred to as the "no-slip condition," and is used for both homogeneous and stratified flows. The no-slip condition forces the relative velocity of the attached fluid to be zero with respect to the surrounding free stream flow. Viscous forces develop within the fluid due to this momentum mismatch near the surface of the sphere. This region is referred to as the boundary layer [40]. The Reynolds number is the ratio of momentum to viscous effects and serves as an indicator of the behavior of fluid flow near physical boundaries and subsequent flow development downstream of these boundaries.

4

The boundary layer of the sphere exhibits different characteristics depending upon the Reynolds number, the Froude number, and possibly the diffusivity [22] of the flow. In turn, the engineering characteristics (e.g. drag or shedding cycles) of the sphere may depend on the characteristics of the boundary layer. The boundary layer on the surface of the sphere may be roughly characterized by two regimes separated by a "critical" Reynolds (Re_{crit}) number [26]. In this study, focus will be maintained in the "sub-critical" regime, $Re < Re_{crit}$, where the boundary layer flow is laminar.

In a homogeneous fluid, viscosity affects the flow around the sphere in the laminar boundary flow around the sphere below a Reynolds number of approximately 25 such that the particles close to the surface of the sphere travel a path parallel to the contour of the sphere surface in an axisymmetric manner [52]. Above a Reynolds number of 25, and below a Reynolds number of roughly 200 [25], the flow behaves in a steady, axisymmetric manner, but the flow creates a so-called recirculation bubble, or vortex ring, that forms behind the sphere [52]. In this case, the convecting fluid particles within the flow do not follow the contour of the sphere's surface. Instead, the particles are convected away from the surface of the sphere, and the flow velocity field creates a stationary region of vorticity behind the sphere known as a "separation bubble." The point at which the fluid particles traveling within the boundary layer stop following the surface contour is commonly referred to as the "separation point," and the boundary layer after the separation point itself is often referred to as being "separated."

These two particular cases of boundary layer behavior dependent on the Reynolds number provide an opportunity to discuss separation in the context of boundary layer flows. Qualitatively, separation is the terminology given to the process of the fluid particle within the boundary layer erupting into the free stream [54]. The exact definition of a separation point is continually evolving within literature starting with the original definition of Prandtl [39] with additional modifications to account for behavior of unsteady flows (e.g. [42] or [20]). These modified definitions all tend to collapse back to the original Prandtl definition for the case of steady, or near-steady flows. Thus, in this study, the choice for the definition of the "separation point" is where the surface skin friction coefficient initially approaches zero, and a "separation line" is the interpolation between the individual separation points. Boundary layers are then considered "separated" after the separation point, except in the rare exception of reversed boundary layer flows that do not qualitatively coincide with the physical description of [54]. The separation behavior of the sphere traveling through the stratified fluid is of interest, especially as it relates to the separation behavior seen in a homogeneous fluid.

Claims to the first study of the relationship between the separation line on the sphere in continuously stratified fluid arrives from Lofquist & Purtell 1984 [34]. There is additional work done by Sysoeva & Chashechkin 1986 [51]; and qualitative results again by Chashechkin & Sysoeva in 1988 [8], specifically at that time with $Fd < 0.2$. The first computational work done in the area of the stratified fluid's effect on separation is from Hanazaki 1988 [21]. The result of these investigations is that separation behavior in the vertical plane is delayed as compared to the homogeneous case as the separation point moves further and further downstream on the surface of the sphere. However as the severity of the stratification increases, the vertical separation point tends to move slightly upwind as the flow approaches a quasi two-dimensional regime induced by the extreme stratification.

According to Hanazaki 1988, at $Re = 200$, $Fd = 0.5$, separation in both vertical and horizontal planes is totally suppressed although Sysoeva & Chashechkin 1986 do not see a total suppression of separation at that Reynolds number. Lofquist & Purtell 1984 do not register a total suppression

5

of separation at $700 < Re < 1000$, $Fd = 0.5$ either but do measure a maximum separation angle of 160 degrees. Additional work by Chomaz *et al.* in 1992 [10] present separation studies at both low and high Reynolds numbers. Their experimental results indicate that a difference in Reynolds number accounts for the discrepancy of separation suppression between [34] and [21]. They also discount the discrepancy at $Re = 200$ between Hanazaki and Sysoeva & Chashechkin as likely due to the apparent inability of the shadowgraph technique to accurately capture separation location [10].

The sketch of Figure 5 in Chomaz *et al.* [10] extends the earlier two dimensional outlook from the vertical and horizontal planes and is a qualitative interpretation of how stratification affects the separation line on the lee side of the sphere. Generally, as the Reynolds number is decreased, the surface area in the separated region decreases [10]. There have been no computational studies of the effects of stratification on the shape of the separation line for the sphere at any Reynolds numbers other than what may be implied from the data from Hanazaki 1988 at a Reynolds number of 200.

1.2.2   The Wake Region

The second physical region of interest is the wake region located on the downwind, lee, side of the sphere. There are several types of laminar wake behaviors behind the sphere; depending generally on the value of the Reynolds number and Froude number. The various types of wakes found in homogeneous fluids will be listed as: steady asymmetric vortex, unsteady symmetric vortex shedding, asymmetric vortex shedding, but reviews of the Reynolds numbers these occur at may be found in [25] or [10]. The properties of the wake may change depending on Froude number as well, but most structures present in the stratified wake are identifiable as some form of the previously mentioned homogeneous wake behaviors. One unique regime found in the stratified fluid flows is the existence of the standing lee wave, which is a laminar mechanism. Above a Reynolds number of 2000, it is expected that the wake region will become turbulent for all Froude numbers higher than 2. Below a Froude number of 2, the balance between strength of stratification and inertial effects (suggested as $Fd \geq C * Re^{-1/2}$ by [31] where C is a calibrated constant) will determine whether the wake is turbulent or laminar according to Figures 2 & 3 in Lin *et al.* [32]; reproduced here for convenience as Figure 4.5.

Theoretical work done in the wake of the sphere utilizes linear theory in the context of a moving point source that is naturally generating internal waves (e.g. Lighthill [28]). Internal waves may exist for all stratified flows. For flows involving a density interface of layered fluids, the internal waves are concentrated along the density interface between layers whereas for continuously stratified flows, internal waves may propagate freely throughout the fluid. The result of linear theory gives insight into the behavior of the internal waves. Linear analyses are generally presented in terms of the lines of constant phase of any waves that propagate outward from the sphere. Linear theory may also be used as a reference to measure the wavelength of any waves present behind the sphere. Because of this, comparisons of experimental and computational observations are often made in some fashion with linear theory.

As mentioned, a unique characteristic of the flow in a stratified fluid is the existence of dominant lee waves. A stationary lee wave is an internal wave propagating with a phase speed relative to that of the sphere it follows such that in the frame of reference to the body, it is stationary. The existence of a standing lee wave is seen in the work of Hanazaki 1988. Hanazaki 1988 [21] conducted simulations at a steady Reynolds number of 200 for a range of Froude number of 0.15 to 200, which

6

is effectively an unstratified flow at that Reynolds number. Hanazaki's work makes comprehensive numerical study of the relationship between the drag on the sphere by standing lee wave behavior in the near wake as well as provides qualitative information about the flow field surrounding a sphere in a continuously stratified fluid. The conclusion of the Hanazaki work is that the linear theory predictions are generally well represented [21].

The work of Lofquist & Purtell in 1984 [34] also investigates the drag coefficient of a sphere moving through a linearly stratified fluid. Lofquist & Purtell 1984 suggest that regardless of Reynolds number, the lee wave, which is dependent on the stratification, induces drag [34]. It is suggested that there is an increase in drag coefficient that is independent of Reynolds number as the fluid becomes increasingly stratified until a Froude number of about 0.125. Below that Froude number, the drag coefficient begins to decrease as Froude number decreases. This is shown in Figure 4 of that work [34]. A general agreement to this trend is stated by Hanazaki, presented as Figure 8 in that work [21]. However, the Hanazaki work suggests the decrease in drag coefficient begins to occur after $Fd = 0.25$.

In turbulent stratified flows around a sphere, the wake region can be broken down into three regions: the near wake, the non-equilibrium regime, and the far wake (e.g. Spedding 1997 [49]). The near-wake is located where the flow exhibits similar characteristics to the unstratified case. After the near-wake regime, there is the so-called non-equilibrium (NEQ) region, where buoyancy effects become apparent as the flow begins to exhibit a reduction in vertical velocity fluctuations. Finally, there is the far-wake quasi-2D regime (Q2D), where the flow characteristics become quasi two-dimensional as "pancake" eddies form. The near-wake region typically exists for $Nt < 2$; the NEQ region for $2 < Nt < 50$, and the Q2D regime from $Nt > 50$ according to Spedding 1997 [49].

The stratification is believed to have little influence on the turbulence of the near-wake. The phenomenological argument is made that in the very near wake at high Reynolds number, the kinetic energy in the wake is high compared to the potential energy required to move a fluid particle vertically in the wake. This is the characteristic of the near-wake behavior. The work by Hopfinger *et al.* [23] gives interesting insight into the behavior of the flow at a Reynolds number of 3000. The Froude number parameter denotes a possible change in the mechanism for generating internal waves. If the Froude number is less than 2, then the wake is dominated by lee waves. If the Froude number is greater than 2, then the internal wave field is dominated by the turbulent wake and internal waves produced are seemingly random. This suggests that even at high Reynolds number flows, the stratification has the ability to influence the flow characteristics even when stratification is not considered severe.

As the kinetic energy from the near-wake decays, the available surplus in converting kinetic to potential energy decreases and as a result, the growth rate of the wake's vertical height decreases so that the wake spreads faster in the horizontal than the vertical. This is the essence of the NEQ regime. Schooley & Stewart 1963 [41] first noticed this behavior, is also noted by Pao & Kao 1977 [38] and reviewed by Lin & Pao 1979 [30]. The NEQ region is often referred to as the "collapse" of the wake. This phraseology is not globally accepted as an accurate description of the physical behavior in this region. Once the vertical velocity perturbations are negligible when compared to the horizontal ones, the wake has evolved into the far-wake region according to Bonnier *et al.* 1998 [5].

Recent interest in continuously stratified flows around submersed bodies is partially focused on turbulent far-wakes and whether the far-wake exhibits any characteristics dependent on the shape of the submersed body. In 2004, Meunier and Spedding speculated that the momentum induced by

a towed body, and not the particular shape, is important for the characteristics exhibited by the far wake [35]. In 2006, Meunier and Spedding generalized that result to include the effective momentum diameter hypothesis to encompass self-propelled submersed bodies [36]. Thus, all submersed bodies traveling through a stratified fluid, whether towed or self-propelled, may be appropriately scaled by an effective momentum diameter [36]. As a result, a sphere traveling horizontally and steadily through a continuously stratified fluid is, by geometry, its own effective diameter and the canon of the sphere is confirmed.

Recent computational investigations have been typically focused on effects of stratification in the far wake behind the sphere. Currently, far-wake numerical simulations require an initialization procedure to create an initial turbulent flow-field to begin integration of the governing equations in time ([16] [15]). Dommermuth et al. 2002 [16] initialized far wake simulations based in-part on the results of Bevilaqua & Lykoudis 1978 [3]. The data available is a Gaussian distribution of the average turbulent kinetic energy [3]. Diamessis et al. 2005 also followed this initialization procedure [15], and recent researchers have also used a similar scheme [7]. It should be noted that results in [3] are not collected from stratified flow experiments.

None of the aforementioned simulations have included the sphere explicitly within the domain. This is because the computational cost to both model the proper fluid mechanics on the sphere and reproduce the far-wake is prohibitively expensive with current computational resources. Through non-dimensionalization and algebraic relationships, the regimes become separated by $N * t$, or equivalently $Fd^{-1} x/D$. In a study where $Fd = 5$, for example, the near-wake regime may not end until roughly 20 body lengths downstream of the body, and the Q2D regime does not begin until 250 body lengths downstream. By comparison, the boundary layer at the stagnation point of a sphere at a Reynolds number of 10,000 is roughly one-hundredth of a body length thin.

Brucker & Sarkar 2010 [7] suggest that there still is "no dataset which characterizes the full state of the turbulence in the near wake region." There is then an opportunity to explicitly account for the sphere within the computational domain and provide detailed information about turbulent fluctuations as well as the density field in the near-wake. The density perturbation field in particular is challenging to collect experimentally. Bonneton *et al.* 1996 [4] explore the behavior of density stratification in the wake of the sphere and show a strong correlation between the density and the vertical velocity perturbations. There is also work by Bonnier *et al.* 2000 [6] collecting time dependent density field information in the far wake, but that work is limited to measurement via conductivity probe. Many early experiments rely on shadowgraph or dye dispersion techniques (e.g. [31]) not able to detect perturbation velocities, and other optical techniques have difficulties in collecting information about the three dimensional density field.

According to the literature (e.g.[27] [15] [7]), the only known simulation to explicitly account for the sphere within the computational domain while modeling the physical problem under discussion is that of Hanazaki in 1988 [21]. Whilst the Froude number range is considerable in Hanazaki's 1988 work, the chosen Reynolds number and solution method negates any unsteady effects, let alone the required turbulent fields of the near-wake that may be of interest to far-wake modelers. The proposed investigation fits an unfilled niche between existing experimental work done in the near wake and Q2D regimes and the investigations of computational modelers in the far wake.

Chapter 2

Numerical Method

2.1 Numerical Method

The numerical model is solved on a discretized grid that is fitted to a fixed, structured body-fitted coordinate system. The Cartesian coordinates x_i are transformed into generalized coordinates ξ_i but the flow components u_i and density perturbation ρ' in the governing equations remain in the Cartesian coordinates. This is the so-called partial transformation formulation of the governing equations (e.g. Constantinescu 1998 [12]). The effective result of this transformation is that the physical grid is transformed into a computational grid by the transformation relations such that the Cartesian coordinate derivatives are represented in the transformed coordinates: $\vec{x} = <x(\xi, \eta, \zeta), y(\xi, \eta, \zeta), z(\xi, \eta, \zeta)>$. This formulation has been used successfully in several studies of varying geometric configuration [25], [12], [11], [13], [14].

The governing equations must again be recast to reflect the new body-fitted coordinate system. A review of these transformations can be found in Appendix A of Sortiropolous 1991 [45] or in Chapter 2 of Liseikin 1999 [33].

The Jacobian of the general transformation between coordinate systems is denoted:

$$J_{ij} = \frac{\partial x_i}{\partial \xi^j} \tag{2.1}$$

The determinant of the Jacobian is simply denoted as J. Here, x_i represents the Cartesian coordinates and ξ^j represents the coordinates of the transformed computational grid. Equations (1.8)-(1.10) are transformed:

$$\frac{\partial u_i}{\partial t} + V^j \frac{\partial u_i}{\partial \xi^j} + \frac{\partial \xi^j}{\partial x_i} \frac{\partial p'}{\partial \xi^j} - \frac{1}{Re} \left[J \frac{\partial}{\partial \xi^j} \left(\frac{1}{J} g^{jk} \frac{\partial u_i}{\partial \xi^k} \right) \right] + \frac{\rho'}{Fd^2} \delta_{i3} = 0 \tag{2.2}$$

$$\frac{\partial u_i}{\partial \xi^i} = 0 \tag{2.3}$$

$$\frac{\partial \rho'}{\partial t} + V^j \frac{\partial \rho'}{\partial \xi^j} - u_3 - \frac{1}{Pe} \left[J \frac{\partial}{\partial \xi^j} \left(\frac{1}{J} g^{jk} \frac{\partial \rho'}{\partial \xi^k} \right) \right] = 0 \tag{2.4}$$

where

$$V^j = u_i \frac{\partial \xi^j}{\partial x_i}$$

9

and V^j is the contravariant velocity. Also, in Eq. (2.2), the Cartesian unit vector has been dropped from the explicit statement of the equation and is presumed to be understood.

2.1.1 Computational Domain

The numerical model is discretized using finite difference schemes, generally of 2nd or 5th order for the momentum equations and 1st order for density. Finite difference calculations are performed on the computational grid. For this study, the physical grid is constructed in spherical coordinates in an O-O topology, where there are known relations between $<r, \theta, \phi>$ and $\vec{x}$ such that there are also known relations between $\vec{x}$ and $\vec{\xi}$, similar to what is done in [25]:

$$r = \frac{D}{2} + \left(R_{max} - \frac{D}{2}\right)\left(\frac{\tanh\left(k_1 * \frac{\zeta - 1}{\zeta_{max} - 1} - 1\right)}{\tanh k_1} + 1\right) \tag{2.5}$$

$$\theta = \pi \frac{\xi - 1}{\xi_{max} - 1} \tag{2.6}$$

$$\phi = 2\pi \frac{\eta - 1}{\eta_{max} - 2} \tag{2.7}$$

where subsequently:

$$x = r\cos\theta, \;\; y = r\sin\theta\cos\phi, \;\; z = r\sin\theta\sin\phi \tag{2.8}$$

R_{max} is chosen to approximate a far-field condition in the simulations. Figure 4.2 gives a graphical representation of a typical physical grid used in this study. A sketch of the body fitted coordinate system as related to the sphere is found in Figure 4.3.

The computational grid is then constructed from the known relations of Eqs. (2.5)-(2.8). A visualization of the computational grid is in Figure 4.4. There is a periodic overlap of one grid point in the azimuthal direction such that $\eta_1 = \eta_{max-1}$ and $\eta_2 = \eta_{max}$. Additionally, a grid singularity is created by the choice of coordinates in the physical domain, located at $\theta = \{0 = \xi_{min}, \pi = \xi_{max}\}$.

2.1.2 Numerical Solver

The governing equations are integrated by an added transient term in pseudo-time such that when the solution exhibits a steady state in pseudo-time, the governing equations have also converged in real time. This is the main concept of a so-called dual-time stepping scheme, and the implementation by Arnone *et al.*[1] is followed.

Shorthand notation for specific operators within the governing equation is introduced:

$$CONV(\;) = V^j \frac{\partial}{\partial \xi^j}$$

$$PRESS(\;) = \frac{\partial \xi^j}{\partial x_i} \frac{\partial}{\partial \xi^j}$$

$$VISC(\;) = \frac{1}{Re}\left[J\frac{\partial}{\partial \xi^j}\left(\frac{1}{J}g^{jk}\frac{\partial}{\partial \xi^k}\right)\right]$$

and the explicit discretizations of the continuous operators $CONV(\;)$, $PRESS(\;)$, and $VISC(\;)$ are found in Constantinescu 1998 [12].

10

Flow quantities are linearized for implicit treatment of flow variables in pseudo-time integration.

$$Q^{m+1} = Q^m + \Delta Q \tag{2.9}$$

Then the momentum equation (2.2) becomes:

$$
\begin{aligned}
\frac{u_i^{m+1} - u_i^m}{\Delta \tau} + \frac{u_i^m - u_i^n}{\Delta t} + CONV^m(u_i^{m+1}) \\
+ PRESS(p'^{m+1}) - VISC(u_i^{m+1}) + \frac{\rho'^{m+1}}{Fd^2}\delta_{i3} = 0
\end{aligned}
\tag{2.10}
$$

"m" indicates the m-th discrete point in pseudo-time integration and "n" indicates the previous level in the discretized physical time integration. Each iteration begins with $m = n$, and as $\lim_{\Delta Q \to 0} Q^{m+1} = Q^m$, implying $Q^{m+1} = Q^{n+1}$.

The momentum equation is split in psuedo-time to solve for both the momentum and pressure variables. The details are available in Constantinescu 1998 [12]. Once the momentum and pressure field are projected to level "m+1", the additional equations for the turbulence model and the density perturbation are advanced in pseudo-time. The superscript in Eq. (2.10) for the density variable is denoted level "m" for this reason.

The solver uses a non-staggered formulation that stores both pressure and velocity at the nodal grid points. Without a proper formulation, this can create the now-famous "checkerboarding" problem. To counter this potential issue, the solver uses the method of Sortiropolous and Patel [46], which adds an artificial dissipation term to the pressure equation. Values of the pressure dissipation coefficient used in this study were usually 0.05-0.1. The details of its implementation within the numerical integration scheme can be found in Constantinescu 1998 [12].

2.1.3 Turbulence Modeling

As discussed in Section 1.2.2 the Reynolds number ranges investigated in this proposal are anticipated to exhibit turbulent wake behavior. Because of the finite discretized nature of the numerical experiment and present limits on computational resources, the turbulent motions must be approximately modeled. Turbulence modeling is a still-active area of research, and discussion will be kept to the type of modeling employed in this numerical experiment.

Reynolds Averaged Navier Stokes (RANS) formulations are an extensively used method to model turbulent flows. They are particularly suited for flows where only the mean flow properties are desired (e.g. Wilcox pg. 30 [55]). RANS formulations are based on the idea of averaging flow field properties, and they tend to "average-out" the temporal features in the flow as the number of samples or length of averaging time increases. RANS formulations are particularly useful in exploring the behavior of separated boundary layers; assuming the separation point exhibits a quasi-steady nature. RANS formulations are unsuitable if the time-dependent, spatially developing structures of the flow away from the boundary are of interest, especially in the axisymmetric case of the sphere [13].

An alternative approach that attempts to represent the aforementioned large-scale motions is referred to as Large Eddy Simulation (LES). Large eddy simulation attempts to spatially and temporally resolve large-scale motions in space and time but to model any motion that is spatially unresolvable. These spatially unresolvable motions are commonly referred to as the sub-grid scale motions. A major drawback of LES occurs in modeling flows in the presence of a wall, and

11

consequently boundary layers. This is because the scales that exist within boundary layers are very small compared to the other large-scale motions in the flow. As such, the spatial resolution required in pure LES is very fine, and computational costs can be comparable to Direct Numerical Simulation; which is very costly. Thus LES flows near boundaries can be cost-prohibitive and current research in LES simulations deals with wall-modeling close to boundaries.

Instead of RANS or LES alone, Detached Eddy Simulation (DES) is used in this investigation. The essence of DES is that it uses RANS as a wall-model within boundary layers and an LES sub-grid scale type model for resolution of the flow away from walls. DES has, on its own, a variety of formulations (e.g. Spalart *et al.* 1997 [48] or Strelets 2001 [50]) and is not specific to a particular turbulence modeling formulation; only that it behaves in the prescribed RANS/LES manner.

The current investigation uses the Spalart-Allmaras DES (SA-DES) formulation of Constanti-nescu 2004 [14]. Near solid boundaries, where separation occurs, SA-DES uses the one-equation Spalart-Allmaras RANS formulation [47] to predict boundary layer behavior; including separation. Outside of the boundary layer region, the model automatically switches to an eddy resolving LES-type mode. The LES-type model behaves like a Smagorinsky model, which in itself attempts to represent the Kolmogorov spectrum for sub-grid scales as determined by Lilly in 1967 [29]. With this formulation, computational costs can remain closer to LES even with the sphere present in the simulation. It should also be noted that the SA-DES eddy viscosity may be used for the density perturbation's eddy viscosity since the both the molecular Schmidt number and the turbulent Schmidt number are taken to be unity in the turbulent cases as is alluded to in Section 1.1.2.

The addition of the DES turbulence model to the equations of motion, Eq. (2.10), modifies the viscous operator to be time dependent; i.e. $VISC(\ ) \rightarrow VISC^m(\ )$ in the following way:

$$VISC^m(\ ) = \left(\frac{1}{Re} + \frac{1}{Re_T^m} \right) \left[J \frac{\partial}{\partial \xi^j} \left(\frac{1}{J} g^{jk} \frac{\partial}{\partial \xi^k} \right) \right]$$

where $\frac{1}{Re_T^m} = \nu_t^m/(UD)$, where ν_t is the eddy viscosity.

Consequently, Eq. (2.10) stays effectively unmodified to the user, and the turbulence model is turned off as the term $\frac{1}{Re_T} \rightarrow 0$. The SA-DES formulation for the eddy viscosity is reproduced from Nikitin *et al.* 2000 [37] as follows:

$$\frac{\partial \tilde{\nu}}{\partial t} + V^j \frac{\partial \tilde{\nu}}{\partial \xi^j} = c_{b1} \tilde{S} \tilde{\nu} + \frac{1}{\sigma} \left[\left(\nabla \cdot (\nu + \tilde{\nu}) \nabla \tilde{\nu} \right) + c_{b2} \left(\nabla \tilde{\nu} \right)^2 \right] \\ - c_{w1} f_w \left[\frac{\tilde{\nu}}{\tilde{d}} \right]^2 \tag{2.11}$$

where:

$$\nu_t = \tilde{\nu} f_{\nu 1}, \quad f_{\nu 1} = \frac{\chi^3}{\chi^3 + c_{\nu 1}^3}, \quad \chi = \frac{\tilde{\nu}}{\nu}$$

$$\tilde{S} = S + \left(\tilde{\nu}/\kappa \tilde{d}^2 \right), \quad f_{\nu 2} = 1 - \chi/\left(1 + \chi f_{\nu 1}\right)$$

$$f_w = g \left[\frac{1 + c_{w3}^6}{g^6 + c_{w3}^6} \right]^{\frac{1}{6}}, \quad g = r + c_{w2} \left(r^6 - r \right), \quad \tilde{r} = \frac{\tilde{\nu}}{\tilde{S} \kappa^2 \tilde{d}}$$

$$\tilde{d} = min \left(d_w, C_{DES} \triangle \right)$$

12

and S is the magnitude of the vorticity; d_w is the physical distance to the wall; Δ is the local grid spacing; $c_{b1} = .1355$, $\sigma = 2/3$, $c_{b2} = 0.622$, $\kappa = .41$, $c_{w1} = c_{b1}/\kappa^2 + (1 + c_B 2)/\sigma$, $c_{w2} = 0.3$, $c_{w3} = 2$, and $c_{\nu1} = 7.1$ are modeling constants. The value of C_{DES} is generally set at 0.65 following the work done by Shur *et al.* [44] for homogeneous turbulence.

2.1.4 Boundary Conditions

Momentum, Turbulence Model, and Density B.C.'s

On the surface of the sphere, $R_{min} = \zeta_{min}$, Dirichlet boundary conditions are enforced for momentum and the turbulence model variable, whilst density perturbations use the zero-normal gradient boundary condition to enforce incompressibility within the diffusive density equation:

$$\vec{u} = \vec{0}, \quad \tilde{\nu} = 0, \quad \frac{\partial \rho^{'}}{\partial n} = 0 \tag{2.12}$$

At the domain boundary far from the sphere, mixed boundary conditions are used due to the geometry of the physical grid. The first condition is referred to as an "inflow" boundary and has a Dirichlet condition for the velocity, the turbulent variable, and any density perturbations for the surface along $\{\xi_{min} = 0 \leq \theta < .55\pi, \ \zeta_{max} = R_{max}\}$:

$$\vec{u} = \vec{e_1}, \quad \tilde{\nu} = 0, \quad \rho^{'} = 0 \tag{2.13}$$

If the inflow boundary is far upstream from the sphere, it is considered sufficient to use the Dirichlet conditions for low Reynolds number, stratified cases, according to Hanazaki 1988[21]. Hanazaki used an outer domain distance of 20 sphere diameters [21]. In the current study, the domain boundary is set 14.5 sphere diameters away from the surface of the sphere. This distance was found sufficient for low Reynolds simulations in [25] and was also found sufficient for turbulent, high Reynolds number ($Re > 10^5$) simulations [14]. Both [25] and [14] were simulations of a sphere traveling steadily through a fluid of a uniform density.

The second condition on the domain boundary away from the sphere is considered an "outflow" boundary condition. Outflow boundary conditions rely on information from inside the computational domain. The outflow boundary is contained on the surface where $\{.55\pi \leq \theta \leq \pi = \xi_{max}, \ \zeta_{max} = R_{max}\}$:

$$\frac{D u_i}{Dt} + \frac{\rho^{'}}{Fd^2}\delta_{i3} = 0, \quad \frac{D\tilde{\nu}}{Dt} = 0, \quad \frac{D\rho^{'}}{Dt} - u_3 = 0 \tag{2.14}$$

For momentum, these conditions allow a fluid particle to accelerate in the vertical due to buoyancy forcing but without accelerating in the horizontal. Incompressibility is applied via the density equation; leaving u_3 in the formulation of the boundary condition to represent the transport of the background fluid density (e.g. Kundu pg. 249 [26]).

On the singularity lines present at $\theta = \{0, \pi\}$, all variables for momentum, the turbulence model, and density are extrapolated from the interior and averaged over the repeated nodes. Along the periodic overlap in the η direction, periodicity is applied to each respective flow variable.

Pressure B.C.'s

The pressure boundary condition is controlled by using the normal component of the momentum equation Eq. (2.2) on the computational boundaries located at R_{min} and R_{max} to enforce

13

conservation of mass [19]:

$$\left[\nabla \left(P \right) = -\frac{\partial \vec{u}}{\partial t} - CONV(\vec{u}) + VISC(\vec{u}) - \frac{\rho'}{Fd^2} \right] \cdot \vec{\zeta} \tag{2.15}$$

This provides an explicit equation for the pressure variable when put into discretized form along both the sphere surface and the far field domain boundary.

Along the singularity lines present at $\theta = \{0, \pi\}$, the pressure is extrapolated from the interior; subject to the conservation of mass constraints and similar to what is recommended in Johnson 1999 [25]. Along the periodic overlap in the η direction, periodicity is applied to the pressure field as well.

2.1.5 Computational Outflow Boundary Treatments

The physical problem being modeled exists within an infinite domain and may contain internal waves that propagate from within the turbulent wake structure (see Section 1.2.2). An infinite domain would allow any internal waves to propagate out towards infinity, which is the expected behavior (e.g. Lighthill, Section 4.9 [28]). This is known as the radiation condition.

Introducing an artificial boundary at the edge of the physical domain complicates computational simulations containing waves because the radiation condition may not be appropriately met. Turbulent wakes produce waves close to the computational boundary. The exact correction required to ensure the radiation condition to be completely satisfied is as-yet elusive, and several approaches are actively under investigation (e.g. Givoli 2004 [18]).

Viscous Damping

It is desirable to find a method capable of reducing these potentially reflected waves while at the same time maintaining a certain simplicity in its implementation. A tempting methodology is to introduce some artificial viscous damping to the equations of motion, Eq. (2.2), near the region of the boundary, but far enough from the region of interest so as not to adversely affect the investigation's observations:

$$NS(q) = -\nu\left(x\right)q \tag{2.16}$$

$$NS(q) = \mu\left(x\right)\frac{\partial^2 q}{\partial x^2} \tag{2.17}$$

where $NS(q)$ represents the original Navier-Stokes bracketed term in Eq. (2.2) operating on any desired quantity q that is to be damped. $\nu(x)$ and $\mu(x)$ are the damping coefficients which are allowed to vary spatially. Israeli and Orszag 1981 [24] show that the damping term must vary smoothly in space to avoid reflections off of the damper interface itself, and they show that Eq. (2.16) is superior in its wave damping properties. In flows with turbulent quantities where fluctuations may be centered about some mean profile value, Eq. (2.16) may be extended to what is used in Brucker 2010 [7]:

$$NS(q) = -\nu\left(x\right)\left(Q - q\right) \tag{2.18}$$

where Q represents the characteristic mean quantity of the flow variable q that is to be attained within the damping region.

14

Damping with Zonal DES

An original unpublished method that may be viable is to use the eddy viscosity of the turbulence model itself, rather than an arbitrary addition to the equations of motion, to damp out any oscillations towards or near the boundary. The idea is to use the "switch" inherent to the DES formulation Eq. (2.11) to explicitly turn off the LES mode towards the outflow boundary and return the turbulence modeling to RANS; explicitly:

$$\tilde{d} = d_w \text{ for } \vec{x} \in \Omega(\vec{x}_{damp}) \tag{2.19}$$

where d_w is the physical distance to the wall as in the original SA-RANS model [47] and $\Omega(\vec{x}_{damp})$ is the domain in which damping is desired. This would create a RANS simulation at the outflow and would maintain the DES behavior desired in the separation and wake region.

An additional possibility of using the DES formulation as a damper is to increase the value of C_{DES} found in Section 2.1.3 for areas near the computational outflow boundary. Constantinescu and Squires 2004 [11] show that by increasing the value of C_{DES} the smaller scales in the energy spectra decay as C_{DES} is increased. Conceptually, for high enough vales of C_{DES}, damping acts similar to RANS.

Chapter 3

Preliminary Results

3.1 Laminar Regime

3.1.1 Re=200 DNS Results

In order to ensure the code produces viable results for stratified flow cases, it is important to compare code results with existing data sets. Since Hanazaki 1988 [21] is related to the proposed work, it is a natural benchmark to compare the current numerical code against.

Perhaps a natural starting point is in comparison of the drag coefficients. Results in Figure 4.8 are in excellent agreement with those of Hanazaki, except for the low $Fd = 0.125$ case. This is an interesting discrepancy between the two works as they tend toward agreement in all other cases at $Re = 200$.

Figure 4.7, which is a measure of the change in stream-wise drag coefficient as function of the Froude number at a Reynolds number of 200. Here, after a value of $Fd = 0.25$ ($1/Fd = 4$), the data of Hanazaki sees a sharp decline in the drag coefficient as the affect of stratification on the surrounding flow becomes more severe, whereas the value of the current work trends to capture experimental trends more closely. The experimental data of both Mason and Lofquist and Purtell show an increasing trend until $Fd \simeq 0.15$ ($1/Fd = 7$); followed by a gradual decline in ΔC_D as $1/F$ approaches a value of 10.

Hanazaki suggests that the discrepancy between the computational results and prior experimental data is due to Reynolds number difference. The experimental data of Lofquist & Purtell 84 [34] show that experiments were conducted at a Reynolds number of approximately 220 for the low Froude number cases. This is not a far departure from the numerical simulations at the Reynolds number of 200 reported by Hanazaki. Hanazki does not report on vortex shedding present at these low Reynolds numbers [21], an observation also noted by Chomaz et al. 1993 [9].

The simulations presented in this investigation do capture the vortex shedding behavior regime. Analysis of the drag coefficient curves presented in Figure 4.9 shows that there is a strong lateral (y-plane) periodic force indicative of vortex shedding. Spectral analysis of the lateral drag coefficient signal shows that there is a Strouhal number of 0.18 for the Fd=0.125 case. Strouhal numbers for this case's drag signals can be seen in Table 3.1.

The shedding of the vertical component of vorticity, ω_z, over the course of 1 shedding cycle is presented in Figure 4.11. Qualitatively, it is apparent that the sign of ω_z on either side of the x-axis alternates every quarter period in the wake region.

In homogeneous fluid flows around a sphere, drag coefficients may also depend on the location

16

	St	Power
x:	$\{0.035, 0.355\}$	$\{28, 16.23\}$
y:	0.18	426.5
z:	No significant peaks.	

Table 3.1: Drag coefficient Strouhal numbers: Re=200, Fd=0.125

of the separation point/line on the sphere. To locate the separation point on an azimuthal plane of the sphere, the skin friction coefficient is used as an indicator for separation. The skin friction coefficients for a range of Fd are shown in Figure 4.12.

As mentioned in Section 1.2.1, a zero skin friction coefficient may not be the best absolute indicator for separated flow. A qualitative idea of what is physically occurring in these steady flows can be derived by looking at the streamlines close to the sphere as in Figure 4.14. The necessity of this additional information may be seen in in Figure 4.12 (c), where there is an apparent crossing of the zero value for polar values of roughly 145° and 160° for the vertical azimuthal plane. Inspection of Figure 4.14 (c) shows that particles in the flow eject away from the body of the sphere, and indeed the separation point is located at 145° where this first occurs.

In Figure 4.13, comparison is made of the vertical and horizontal separation points' location as compared to the data of Hanazaki 1988. It becomes apparent from this figure that there are differences between the two cases.

As suggested in Section 1.2.2, one of the main advantages of computational investigations into stratified flows is the relative ease which it is possible to obtain instantaneous density profiles of the entire flow field. In Hanazaki 1988, isopycnals are presented and that trend is followed here.

An advantage of the linear density stratification is that with non-dimensionalization, the actual density gradient term "drops out" of the governing equations. Thus, any linear gradient may be imposed on the density perturbation field to represent the more physically intuitive isopycnals; the numerical values of which are then arbitrary. Isopycnals from the simulations are presented in Figure 4.15. From this figure, the flow slowly becomes more two dimensional as the Froude number decreases; signifying the tendency of the flow to begin its pseudo two dimensional layered behavior.

Finally, contours of vertical components of velocity, w, are presented in Figure 4.16. These contours for this low Reynolds number case serve as contrast contours to identify lines of constant phase. Lines of constant phase are located where the vertical component of velocity is zero according to linear theory as $\omega = N * sin(\theta)$ [28]. Here, θ is the angle of the motion of the fluid particle with respect to the horizontal; making lines of $w = 0$ equivalent to lines of constant phase.

Perhaps the most striking feature in comparing Figure 4.16 (a)-(d) is that the lines of constant phase appear to have similar patterns in the free stream portion of the flow, but different spacing depending on Froude number. Figure 4.16 hints that reported values for flow behind the sphere in stratified flow simulations should perhaps be given in terms of possibly $\sim \frac{1}{Fd}\frac{x}{D}$ versus $\frac{x}{D}$.

3.1.2 Re=1000 Preliminary Results

Comparisons are initially made with the laminar, unsteady unstratified case at a Re=300 of Johnson [25] to verify the unsteady behavior of the numerical solver. The resulting stream-wise drag coefficient in the prepared case is $Cd_x = .654\pm.004$, $Cd_y = -.054\pm.015$, and $Cd_z = -.035\pm.01$. As is shown in Table 3.2, the average drag coefficient in the stream-wise direction and the drag

17

coefficient on a rotated plane of symmetry (the lateral plane, denoted by the L subscript) compare favorably to Johnson's results.

	Orr '10	Johnson '99
C_{D_x}	0.654 ± 0.004	$0.656 \pm .0035$
C_{D_L}	0.064 ± 0.019	$0.069 \pm .0016$
St_x	0.13	0.137
St_L	0.13	0.137

Table 3.2: Drag Coefficient and Strouhal Number at Re=300, Fd=∞

	Orr '10	Lee '00
C_{D_x}	0.555 ± 0.04	0.545
C_{D_y}	-0.022 ± 0.08	N/R
C_{D_z}	-0.017 ± 0.155	N/R
St_x	{0.04 to 0.05, 0.135 to 0.15}	{0.043, 0.164}

Table 3.3: Drag Coefficient and Strouhal Number at Re=500, Fd=∞. N/R: not reported

Further comparison to the work of Lee 2000 [27] is made to compare the unsteady behavior at a Reynolds number of 500. The time series drag coefficient data is again compared in Table 3.3. Results appear to compare favorably against this data set. Strouhal numbers associated with both the unsteady motion of the separation point and the unsteady vortex shedding produce similar temporal behavior; within a 10% error of what is produced by Lee. There are inherent differences between the numerical method of Lee 2000 and the current study, and it is possible that either grid resolution, or the discretization scheme, or even the solution method may account for this discrepancy. Of interest is that the ratio of peak Strouhal numbers between Lee and the current study is within a few percent; suggesting that whatever the discrepancy in exact value of Strouhal numbers, the relations between the various physical mechanisms of the simulations seem to be in agreement.

After the above comparisons to check unsteady behavior, the Reynolds number is further increased to 1000. The general approach for Re=200 is followed as a guide for the analysis of Re=1000. At this Reynolds number, there are four distinct regimes of the wake reported by Lin *et al.* [32]: the lee wave instability, the non-axisymmetric vortex, the symmetric vortex shedding, and the non-symmetric vortex shedding. Data is presented at Froude numbers of 2, 0.5, and 0.25. These points correspond to non-symmetric vortex shedding, non-axisymmetric vortex, and lee wave instability regions, respectively. The data for the expected symmetric vortex shedding region is not available at this time.

The relationship for the drag coefficients as seen in Figure 4.17 remain relatively unchanged from the Re=200 cases presented in the Figure 4.7 counterparts. It will be of interested to examine the Fd=0.125 case to see if the trend at Re=1000 is continued as is seen at Re=200 for the stream-wise drag coefficient.

Inspection of the Re=1000, Fd=0.25 case warrants further explanation as unsteady effects were observed whereas the guide of Lin *et al.* suggests a steady lee wave formation behind the sphere.

Evidence of unsteady vortex shedding is seen by inspection of the drag coefficient time-series in Figure 4.22 and supported by the strong spectral peak contained in Figure 4.23. Qualitative appearance of vortex shedding similar to the behavior in Figure 4.11 has been confirmed and is not reproduced here.

Inspection of the pressure coefficients in the vertical ($z \geq 0$) and horizontal ($y \leq 0$) in Figure 4.18 suggest that while general relationships between the two planes remain roughly the same, there are a few quantitative differences between the Re=200 and Re=1000 case as the Froude number decreases. This is especially clear at a Froude number of 0.25, where an internal hydraulic jump (as defined by Hanazaki 1988 [21] is seen for the Re=1000 case, whereas it is not seen for the Re=200, Fd=0.25 case.

By comparing Figure 4.12 and Figure 4.19, interesting agreement is seen in the behavior of the separation point at a Reynolds number of 1000 is qualitatively similar to the Reynolds number of 200 case for varying Froude numbers. The separation point is notably delayed in the vertical plane by the stratification. The separation point also does not seem to move as rapidly downwind in the horizontal as compared to the vertical planes, just as in the Reynolds number 200 case. This may be inferred from Figure 4.20, but a more diverse range of Froude numbers for data collection would be prudent. Comparison between Figure 4.13 and Figure 4.20 is a challenge due to lack of available data at Re=1000. It does appear that the variance of vertical and horizontal separation point decreases between the two Reynolds numbers, which may owe to the higher energy contained in the higher Reynolds number flows. The data point at Re=200, Fd=0.5 for the horiztonal separation has been verified as a simulation result, but the reason for this "odd" data point location is not yet known. Separation points may be qualitatively inferred from inspection of the instantaneous velocity vector field as the boundary layer point at separation is assumed to be quasi-steady. This is available in Figure 4.21.

The largest difference between the Re=1000 cases and the Re=200 cases is the ability to observe unsteady effects. Time series signals are then used as the analysis tool, particularly for the density perturbation field. A probe is placed at an $Fd^{-1} \, x/D \simeq 4$ (Fd=2) to observe the unsteady behavior of the flow in the near-wake. By inspection of Figure 4.24 and Figure 4.25 it is possible to see that there is a clear correlation between the vertical velocity, w', and the density perturbation field, ρ'. Note that inspection between Figure 4.24 (a) and (b) at $t^* \simeq 130$ show a slight difference in signal values, indicating they are not perfectly correlated, but the two signals do remain highly correlated. Figure 4.25 serves as an additional qualitative indicator of this and clearly w' is a leading order term in Equation 1.10, but analyses of the phase lag of the two signals may be required as complete evidence of this claim.

Inspection of the lines of constant phase in Figure 4.26 indicates that the variance in Reynolds number does not appear to affect the internal wave properties in the free stream as is also seen in Section 3.1.1.

19

3.2 Turbulent Regime

3.2.1 Re=5000 SA-DES Results

Based on available data, this investigation is also performed at a Reynolds number of 5000, Froude number of 2, and Schmidt number of 1 while using the SA-DES formulation discussed in Section 2.1.3. All discussion within this section uses these parameters. Two sets of data are used to benchmark the behavior of the simulation at this Reynolds number.

First, the perturbation velocities of the simulations are measured against the current computational standard procedure of using the azimuthally averaged velocities u', v', w'. Both the average and perturbation velocities of the simulation is compared against the Gaussian profiles of Diamessis et $al.$ [15]. All data is averaged in the azimuthal direction, ϕ, then spatially averaged along the x-direction. The radial perturbation velocities here are defined as:

$$u'(r) = \overline{\left(\overline{(u(\vec{x}, t) - U_x(r))_\phi} \right)_x}$$

$$v'(r) = \overline{\left(\overline{(v(\vec{x}, t))_\phi} \right)_x}$$

$$w'(r) = \overline{\left(\overline{(w(\vec{x}, t))_\phi} \right)_x}$$

$$U_x(r) = \overline{\left(\overline{(u(\vec{x}, t))_\phi} \right)_x}$$

where u, v, w represent the Cartesian vector components of the velocity vector field and $U_x(r)$ is the stream-wise averaged velocity dependent only on radial distance from the x-axis. u' is also referred to as the stream-wise perturbation velocity.

The data is collected at the same location that Diamessis et $al.$ initialize their simulations [15] at $Nt = 3$, which is the equivalent downstream distance of $(1/Fd)(x/D) = 3$, taken from the center of the sphere. The mean streamwise velocity profile is compared in Figure 4.27. The mean average velocity compares relatively well to the Gaussian profile fit. This appears to indicate that the SA-DES model does a relatively good job of predicting the mean flow properties in the wake.

Further comparison is made against the Gaussian fitted profile of [15], where the perturbation velocities u', v', w' are averaged together. This is the assumption made for the velocity perturbation initial condition field by Dommermuth et $al.$ [16] and Diamessis et $al.$ [15] as well as Bruker & Sarkar [7]. The comparison can be seen in Figure 4.29. There is the expected drop in turbulent fluctuations at the center of the core, indicating a relatively lower region of turbulent production there. This trend is also reflected by the Gaussian fit. Again, the computational result appears to compare favorably to the Gaussian averaged profile currently used by computational modelers.

The individual perturbation velocities are also investigated. The result can be seen in Figure 4.29. As seen, the perturbation velocities are not equally contributing to the average profile seen in Figure 4.29. The components of the perturbation velocities make up the turbulent kinetic energy, i.e. $k = 1/2 (u^2 + v^2 + w^2)^{1/2}$, and thus, the question is raised of whether the assumption of the equipartition of the turbulent energy remains valid for [15], [16], and [7]. It appears here that stream-wise fluctuations contribute the most to the average turbulence profile; followed by the vertical velocity perturbations and the lateral velocity perturbations. As the distance from the x-axis increases, stream-wise fluctuations decrease quickly, whereas both lateral and vertical velocity perturbations appear not to decay until well away from the x-axis. If there is this anisotropy in

the perturbation profiles, it is perhaps natural to seek experimental data which is not azimuthally averaged.

For this reason, a second comparison is made against an available experimental data set ($y = 0$) produced by Spedding at USC. Because of the experimental techniques used to collect the data, specific planes must be chosen to investigate the flowfield. Thus, the velocity field in the vertical plane is available for comparison (i.e. $U_x(z)$, $u'(z)$ and $w'(z)$). The perturbation quantities are defined as:

$$u'(z) = [u(\vec{x}, t) - U_x(z)]_x$$
$$v'(z) = [v(\vec{x}, t)]_x$$
$$w'(z) = [w(\vec{x}, t)]_x$$
$$U_x(z) = [u(\vec{x}, t)]_x$$

where $U_x(z)$ is now the mean profile in the vertical slice, the subscript x indicates spatial averaging in that direction, and there is no azimuthal averaging for any flow variable. The general pattern of comparison from before is continued with the experimental data. Initial comparisons are made for the predicted mean steam-wise velocity profile against the experimental profile as seen in Figure 4.30. Again, without the azimuthal averaging the DES simulation appears to predict the mean profile with some degree of accuracy.

Additional comparisons are made for the available perturbation velocities, u' and w'. The simulations prediction of u' against experimental data is seen in Figure 4.31. The model appears to over-predict the turbulent fluctuations in the "core" ($|z| \leq 1$) of the wake region. However, the model still captures the drop in fluctuations near the center of the core at $z = 0$ for u' seen in earlier comparisons. For the most part, the stream-wise fluctuations are located within the core region. Although there is some minor diffusion of stream-wise fluctuation seen out of the core for $z \leq -1$, perturbations appear fully decayed at $z = -2$.

Remaining comparisons against the data of Spedding may then be made for the vertical velocity fluctuations, w'. In the Guassian profile, there was some apparent diffusion out of the turbulent core for w' as seen in 4.29, and when compared to experimental data in the vertical plane in Figure 4.32, this diffusion of w' out of the core becomes even more obvious. The SA-DES model appears to capture the turbulent levels contained within the core $|z| \leq -1$ reasonably well. Once again, the reduction of turbulence near the center of the core at $z = 0$ is seen. Major levels of vertical perturbation velocities are seen outside of the core and decay of these perturbations is very slow compared to the stream-wise fluctuation profile of Figure 4.31. This region of high vertical velocity shall be referred to as the "tails" of the vertical perturbation velocity profiles.

This appears to indicate some issue with the SA-DES modeling as the simulation trend does not appear to correctly follow the experimental data trend produced by Spedding. In light of Section 2.1.5, which was in turn guided by conversations with other investigators in this field, the suggestion is made that internal waves are, at this point, a main suspect in the cause of these w' tails due to the reflection of the internal waves off of the domain boundary.

To assess this suggestion, the method of Section 2.1.5, a zonal DES damper, was utilized to investigate the possibility of a quick fix to this behavior. An example of results of this attempt are seen in Figure 4.33. It is clear by comparing Figures 4.32 and 4.33 that some degree of w' is removed from outside the core region. However, it also appears that now fluctuations have increased inside the core region. This result gives indication that some boundary treatment may be beneficial to the accuracy of the numerical simulation. Because of the apparent failure of the

21

SA-DES RANS damper, a more recognized method is pursued in the form of the artificial viscous dampers of Section 2.1.5.

Viscous damping to the w' equation is investigated. Viscous dampers are applied to the region within the computational domain where no data collection is desired. An example region of viscous damping is shown in Figure 4.34, although the damping region may be applied as needed but guided by the discussion of Section 2.1.5. An example effect of the addition of the viscous damping term is shown in Figure 4.35. Here, the perturbation velocities are presented in the azimuthal average fashion to include a more three dimensional view of the effects of the damper. Clearly, energy has been added to the core of the wake while the "tails" of the perturbation velocity have not even decayed as in the SA-DES RANS case. This trend was observed for a wide range O(0.1)-O(100) of the $\nu(x)$ coefficient seen in Eq. (2.16) for a variety of damping region shapes.

These attempts at boundary conditions leave the question of the origin of the "tails" unanswered as of yet. Further discussions with researchers in the field of stratified turbulence have suggested that grid resolution is perhaps an additional reason for the poor comparison with experiments. Qualitative inspection compared to the grid resolution may be compared in Figure 4.34. The turbulent regime investigations are left with four potential "tail" inducing culprits: the artificial domain, the damper type, the grid resolution, and the turbulence model itself.

Chapter 4

Future Work

4.1 Laminar Regime

There is quite a possibility that the impact of the Schmidt number on the flow around the sphere on a sphere traveling horizontally through a stratified fluid has not yet been investigated completely. This problem may be particularly difficult for experimentalists to accomplish: a water tank is not set up to work with air, and a wind-tunnel is not particularly adept at investigations using water as its working fluid. This puts the current investigation in a unique position to possibly expand knowledge in this niche area.

4.2 Turbulent Regime

A two-tiered approach is planned:

First, DNS parallelized computations will be made at a Reynolds number of 5000 across a range of Froude number. As shown in Section 3.2, comparison with data from USC is available as a benchmark for computational agreement. This approach has a major advantage over other proposed approaches, despite its high computational cost, in that there is no reliance on any turbulence modeling. Thus, a degree of complexity is removed from the numerical investigation, which will allow the first tier of the proposed work to focus on the underlying physics of the problem.

A second benefit of the DNS approach is that because resolution requirements are already high, the question of internal wave reflection either due to grid coarsening or the limitations of the finite boundary may be alleviated. If the grid is found to be sufficiently fine, but reflections are still encountered due to the location of the domain boundary, then the resolution requirements will still aid in implementation of the boundary treatments as discussed in Section 2.1.5.

The second step of the two-tiered approach is to return to utilization of turbulence modeling. For all its benefits, DNS has an overwhelming drawback: with current world-wide computational resources, DNS is not a tool that can be applied for geophysical flows, or even many engineering-based flows. Ultimately, a viable turbulence model must be located within the engineering community for the simulation of the turbulent near-wake of flow behind a sphere traveling horizontally through a stratified fluid.

The choice of turbulence model with which to continue investigation is currently under consideration. The Spalart Allmaras Detached Eddy Simulation (SA-DES) method as shown in Section 3.2 has not produced necessarily successful results. However, a proclamation of the SADES method inappropriate model.for near-wake flows may be a mistake. Indeed, its "ease" in implementation, especially for pre-written SA-RANS based codes, makes it highly tempting as a turbulence model. However, investigations utilizing SA-DES may prove as difficult as investigations with any other types of turbulence model. A second possible choice for turbulence modeling is Large Eddy Simulation using the Truncated Navier-Stokes (LES-TNS) method (e.g. Tantikul & Domaradzki 2010 [53]). This has an advantage over the SA-DES method in that USC houses the resident experts in the LES-TNS method.

Figures

$\rho_{\circ} + \rho(z)$
$\rho' = 0$
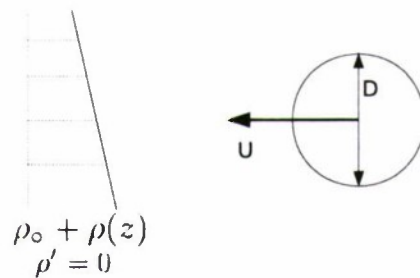
Figure 4.1: Sketch of Physical Problem
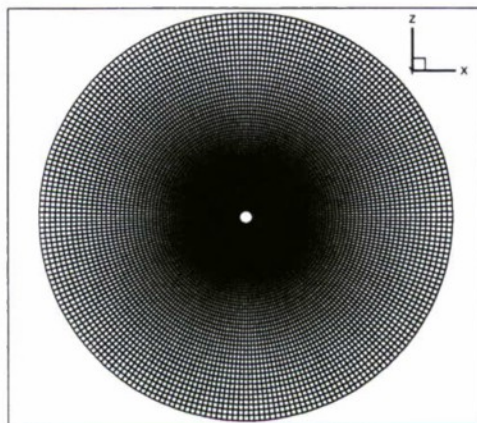
Figure 4.2: Example of O-O grid topology
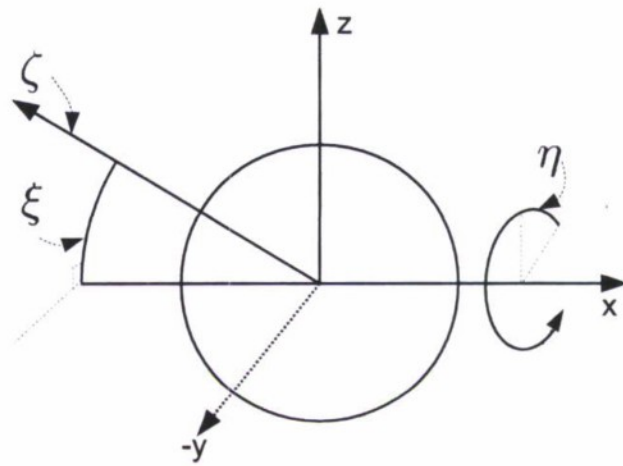
Figure 4.3: Sketch of Body-Fitted Coordinate System
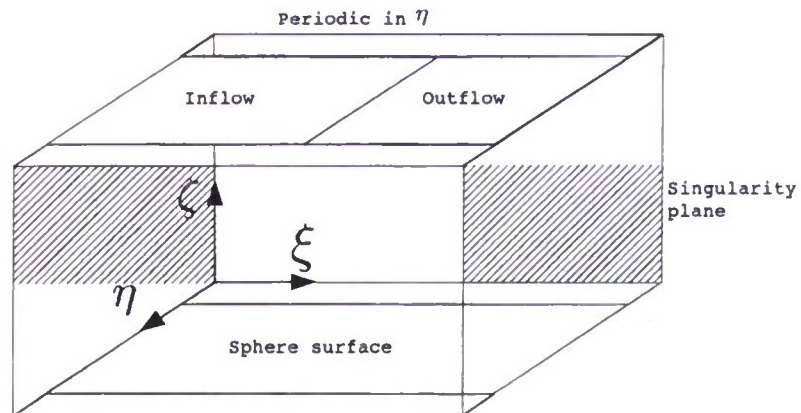
Figure 4.4: Sketch of Computational Grid

26
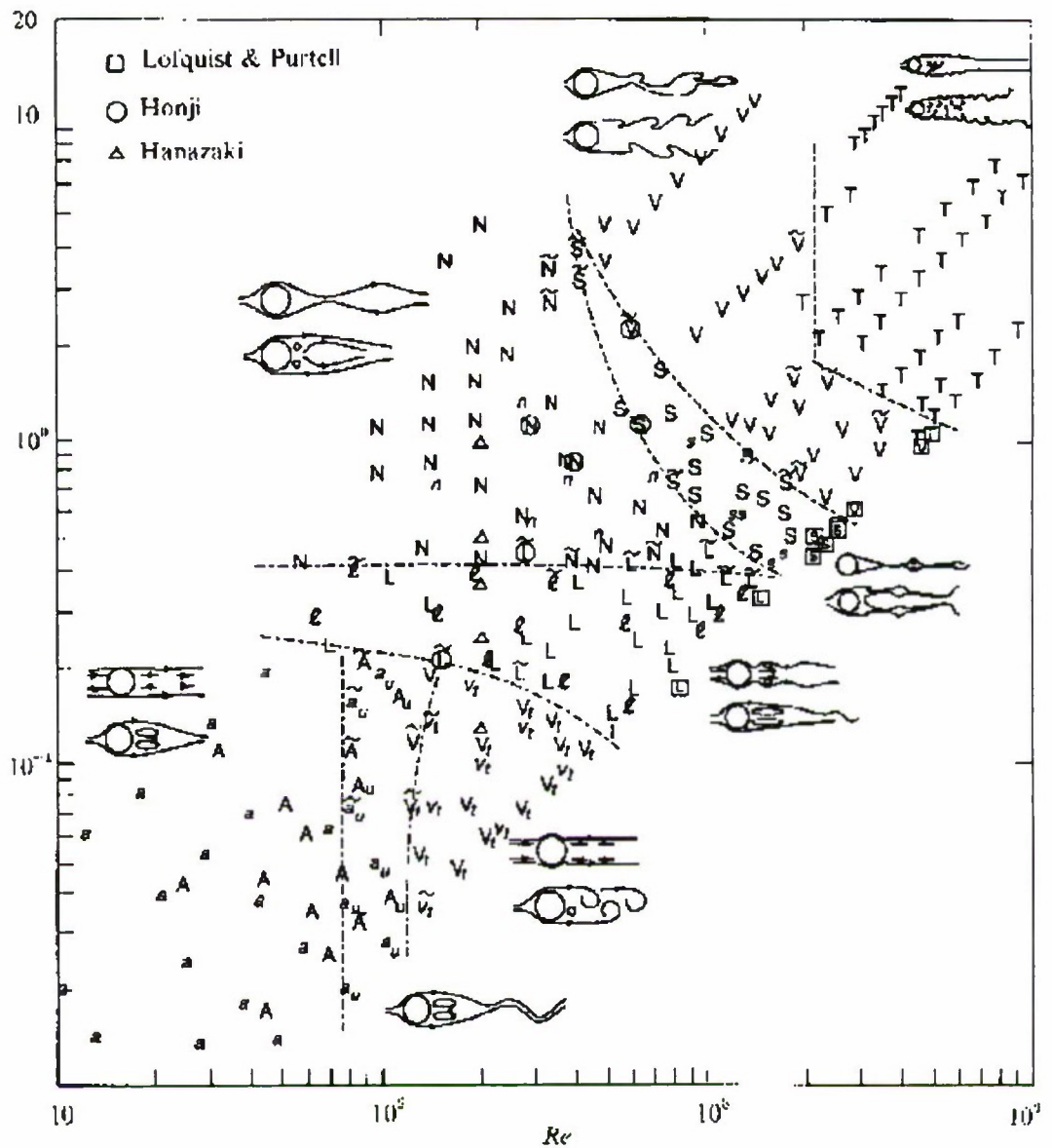
FIGURE 2. Flow regime diagram; Fi vs. Re.

Figure 4.5: Figure 2 of Lin *et al.* 92 [32], (Fi = Fd); reproduced here for convenience.

27
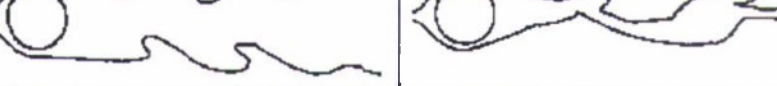
A, a steady two-dimensional attached vortices		
A_u, a_u unsteady two-dimensional attached vortices		
V_t, v_t two-dimensional vortex shedding		
L, ℓ lee-wave instability		
N, n non-axisymmetric attached vortex		
S, s symmetric vortex shedding		
V non-symmetric vortex shedding		
T turbulent wake		

FIGURE 3. Interpretive sketches of flow regimes.

Figure 4.6: Figure 3 of Lin *et al.* 92 [32], (Fi = Fd); reproduced here for convenience.

28
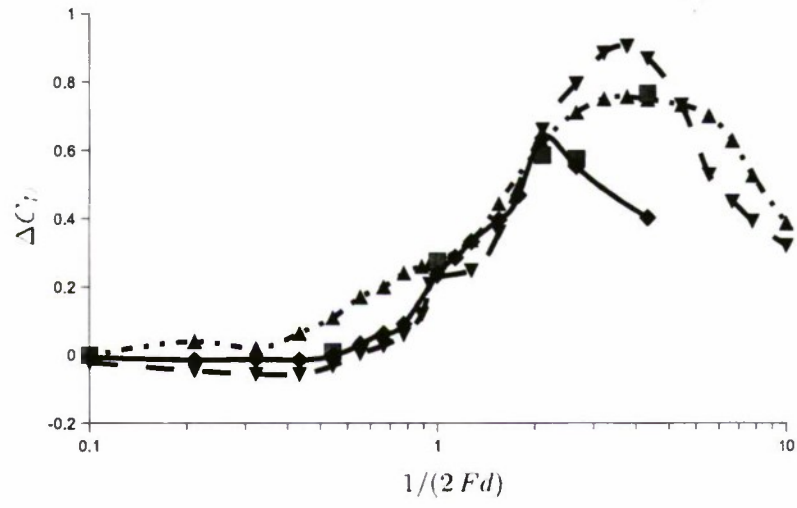
Figure 4.7: Re=200, Sc=1: ΔC_D vs. $1/(2\,Fd)$. ($\square$) Orr '10, ($-$ with $\diamond$) Hanzaki '88, ($-\cdots-$ with $\triangle$) Lofquist & Purtell '84, ($-$ with ∇) Mason '77.
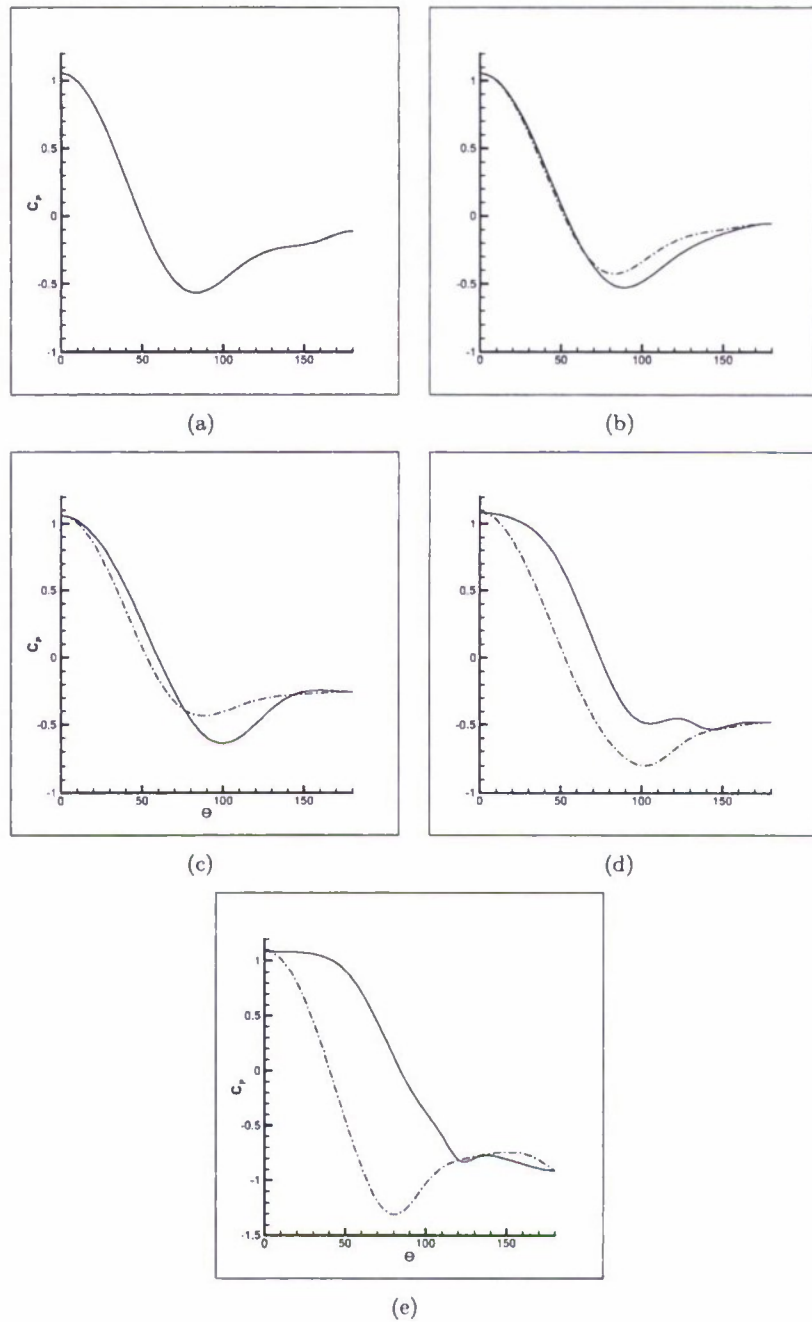
Figure 4.8: Re=200, Sc=1: Surface pressure coefficient, C_P, vs. angle, θ, in the $(-)$ vertical$(z \geq 0)$ and $(- \cdot -)$ horizontal $(y \leq 0)$ plane. θ is taken from the negative x-axis. (a) Fd=∞ (b) Fd=1 (c) Fd=0.5 (d) Fd=0.25 (e) Fd=0.125
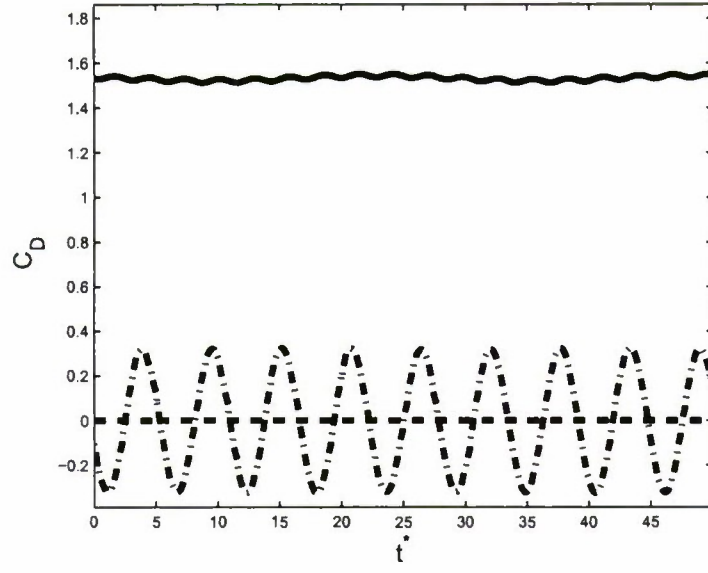
30

Figure 4.9: Re=200, Sc=1, Fd=0.125: Drag coefficient time series. $- C_{D_X}$, $- \cdot - C_{D_Y}$, $-- C_{D_Z}$.
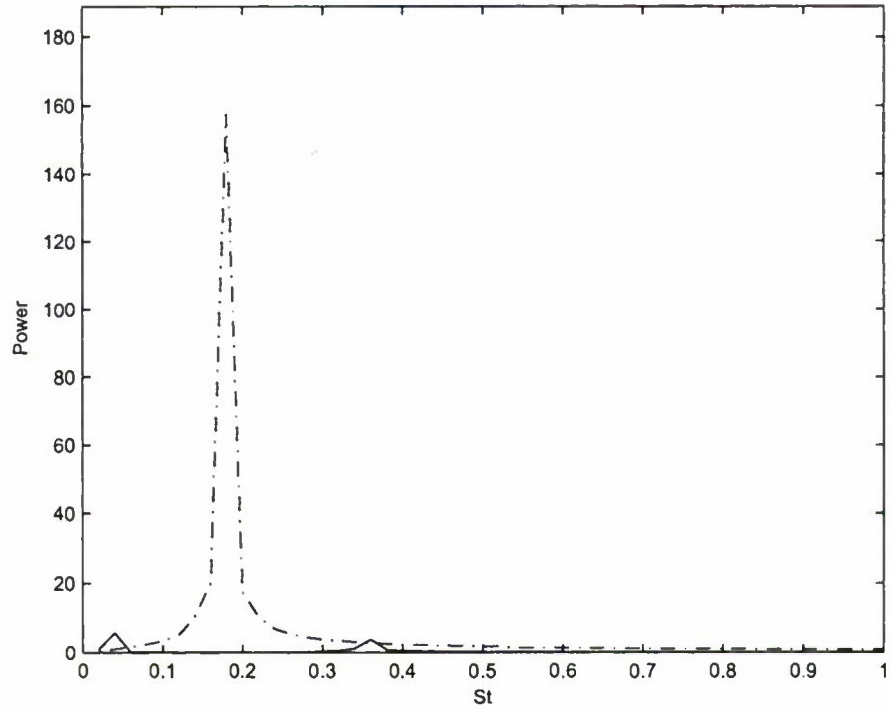
Figure 4.10: Re=200, Sc=1: Drag coefficient power spectra. $- C_{D_x}$, $- \cdot - C_{D_y}$, $-- C_{D_z}$.
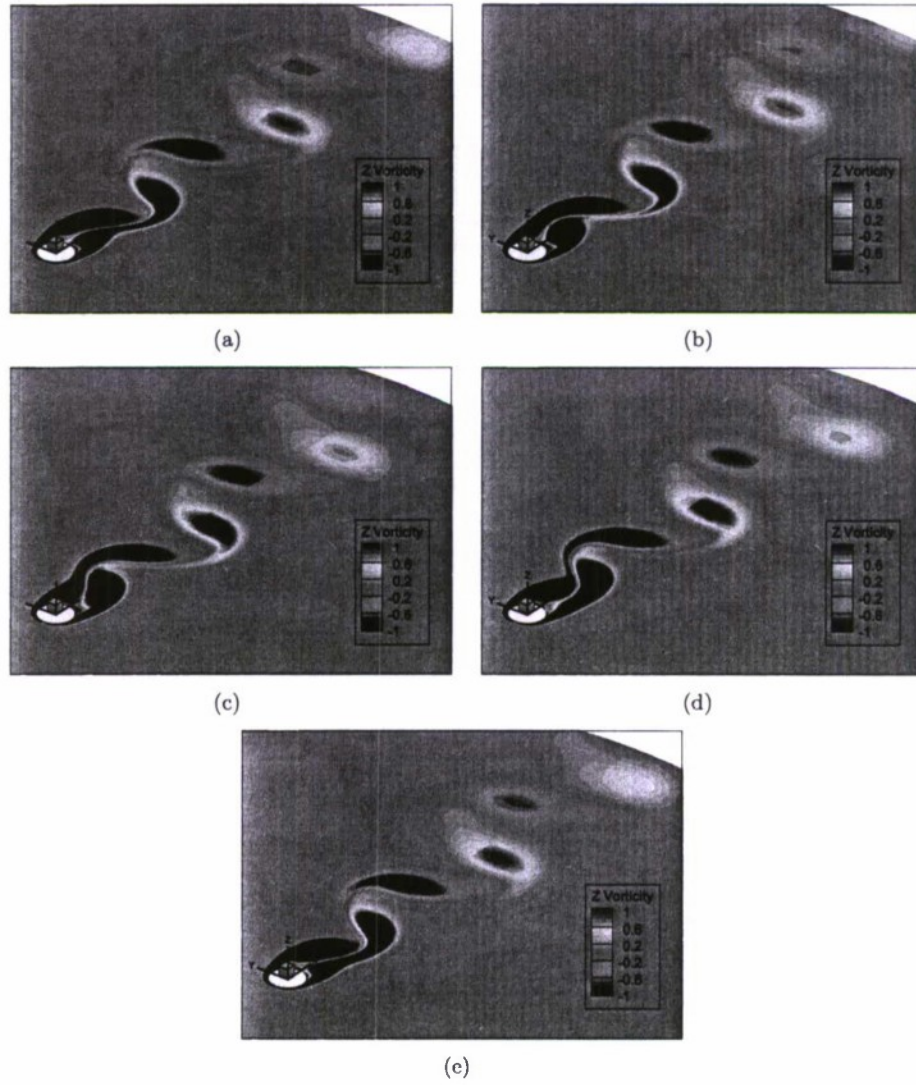
(a)

(b)

(c)

(d)

(e)

Figure 4.11: Re=200, Sc=1, Fd=0.125: Vertical vorticity contours in the horizontal plane at z=0. Contours of ω_z are leveled between ± 1 in increments of 0.1
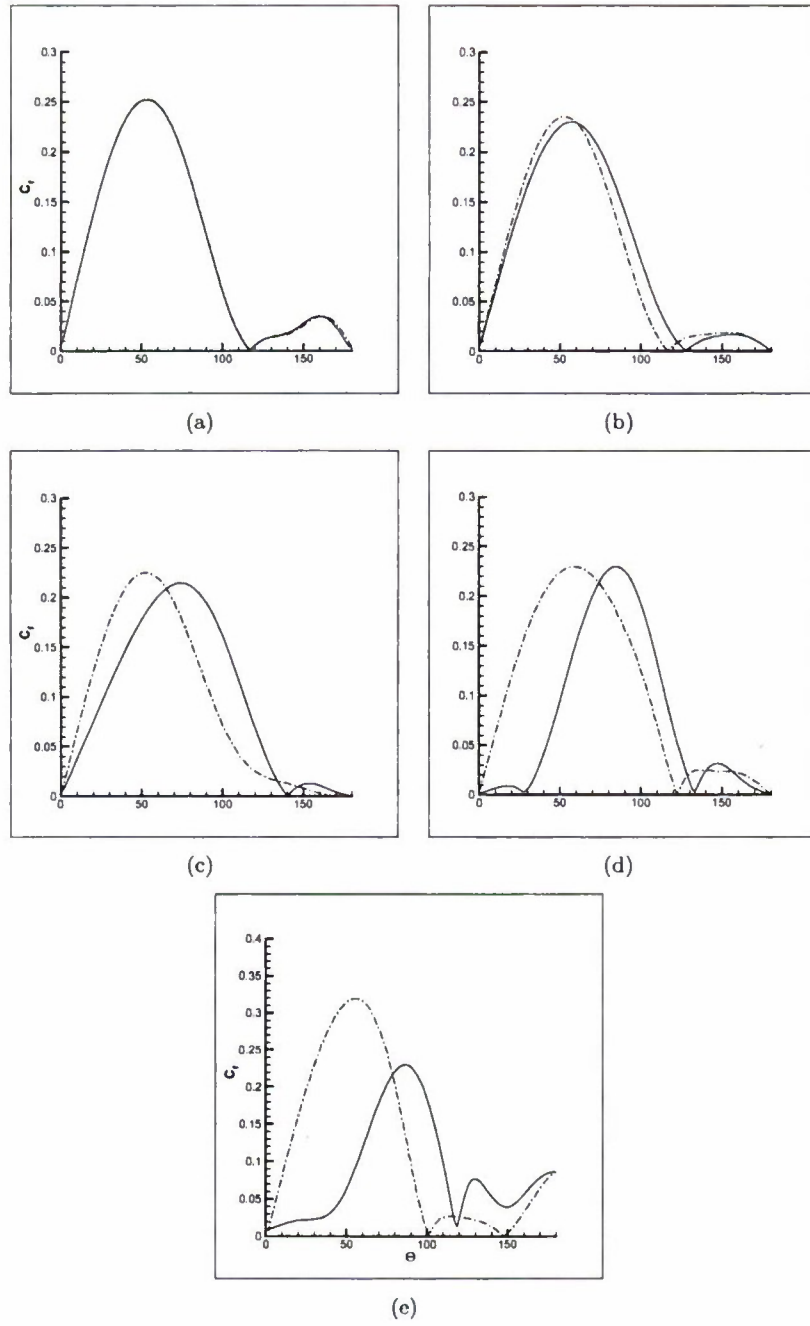
Figure 4.12: Re=200, Sc=1: Surface skin friction coefficient, C_f, vs. angle, θ, in the $(-)$ vertical($z \geq 0$) and $(-\cdot-)$ horizontal $(y \leq 0)$ plane. θ is taken from the negative x-axis. (a) Fd=∞ (b) Fd=1 (c) Fd=0.5 (d) Fd=0.25 (e) Fd=0.125
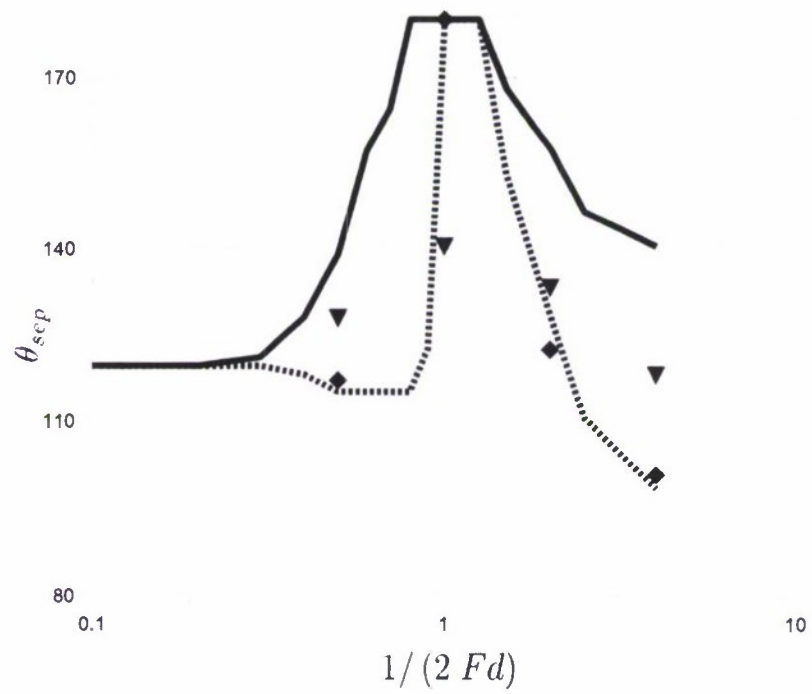
33

Figure 4.13: Re=200 Separation point location vs. $1/(2\,Fd)$. Orr '10 (Sc=1): ($\triangledown$) vertical, ($\diamond$) horizontal. Hanazaki '88 (Sc=∞): ($-$) vertical, ($--$) horizontal.
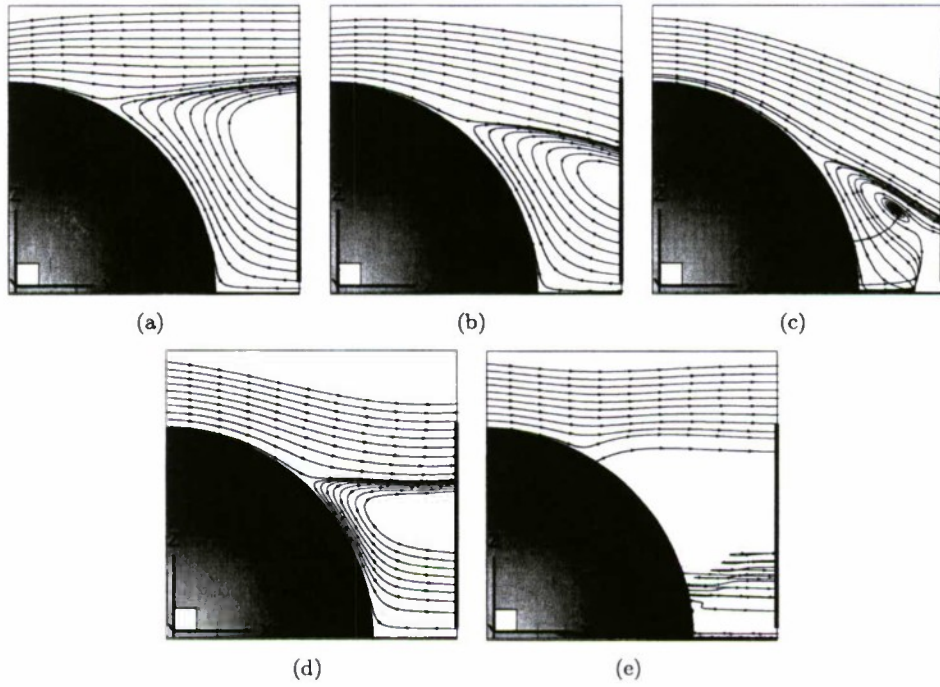
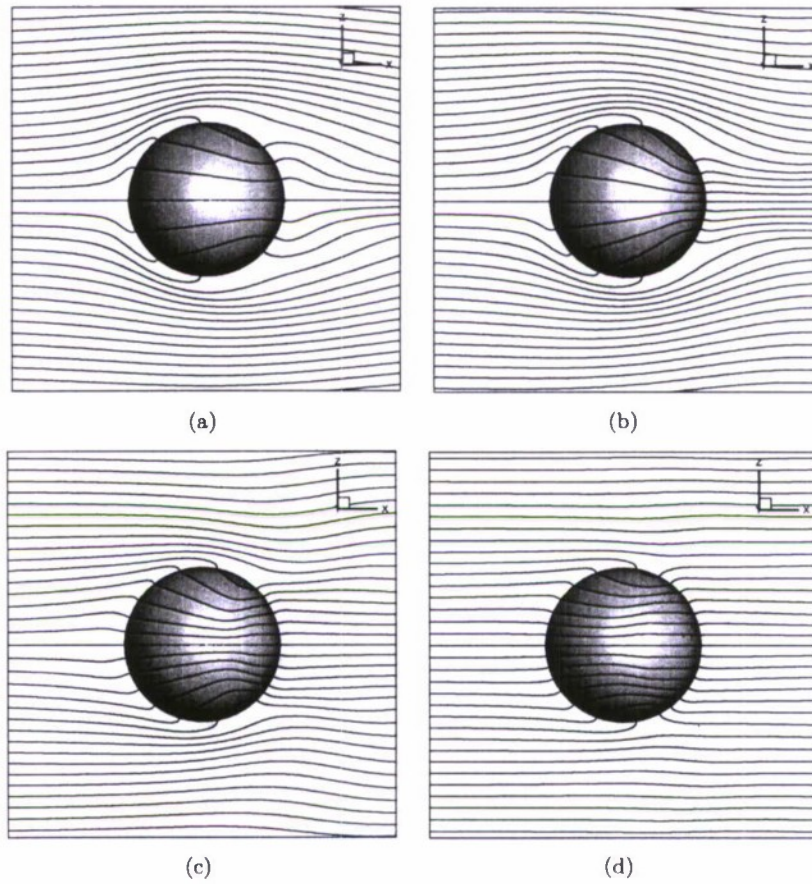Figure 4.14: Re=200, Sc=1: Streamlines on the lee side of the sphere. (a) Fd=∞, (b) Fd=1.0,(c) Fd=0.5, (d) Fd=0.25, (e) Fd=0.125

Figure 4.15: Re=200, Sc=1: Isopycnal lines. Levels of density are chosen between ±1.5 in increments of 0.075. (a) Fd=1 (b) Fd=0.50 (c) Fd=0.25 (d) Fd=0.125

36

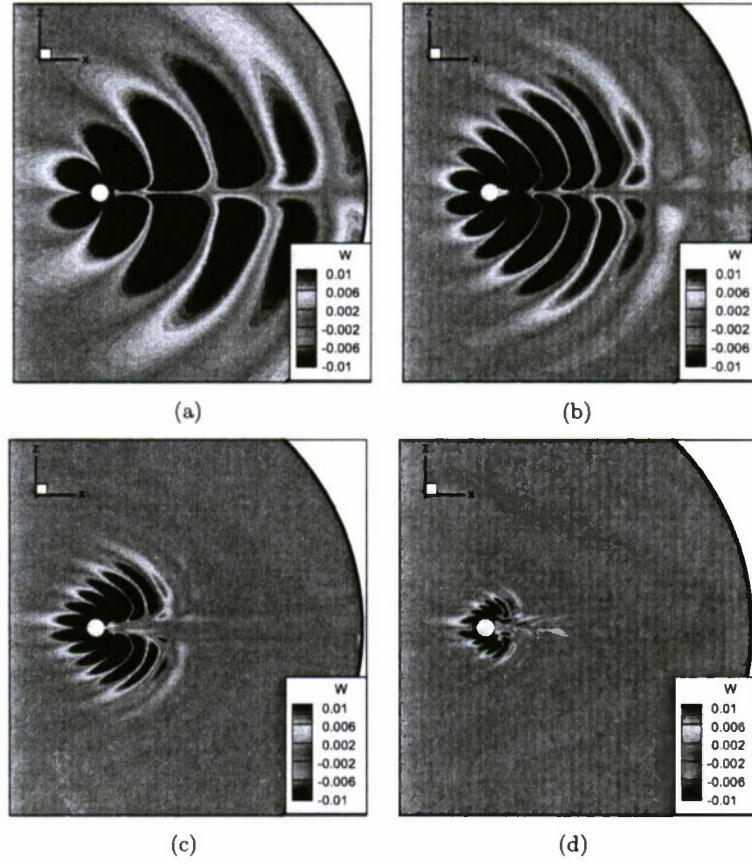Figure 4.16: Re=200, Sc=1: Contours of vertical velocity, w. Levels are between $\pm.01$ in increments of 0.001. (a) Fd=1, (b) Fd=0.50, (c) Fd=0.25, (d) Fd=0.125
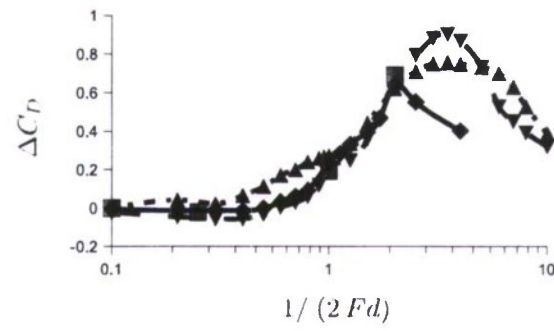
37

Figure 4.17: Re=1000, Sc=1: ΔC_D vs. $1/\left(2\,Fd\right)$. ($\square$) Orr '10, ($-$ with $\diamond$) Hanzaki '88, ($-\cdot\cdot-$ with $\triangle$) Lofquist & Purtell '84, ($-$ with ∇) Mason '77.
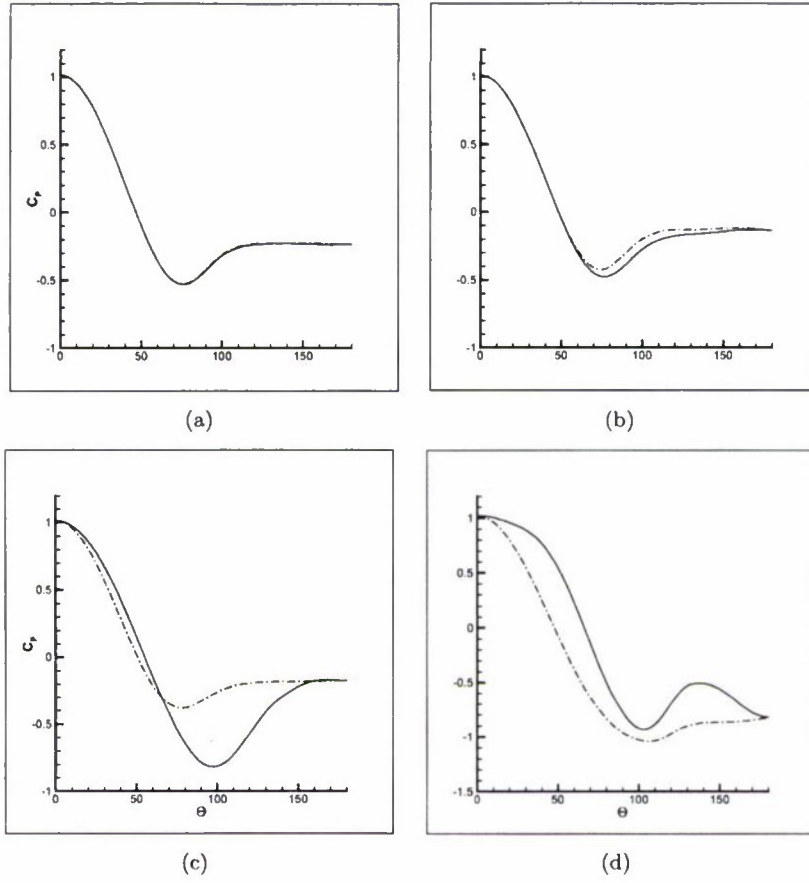
Figure 4.18: Re=1000, Sc=1: Time-averaged surface coefficient of pressure, C_P, vs. angle, θ, in the $(-)$ vertical$(z \geq 0)$ and $(- \cdot -)$ horizontal $(y \leq 0)$ plane. θ is taken from the negative x-axis. (a) Fd=∞ (b) Fd=2 (c) Fd=0.50 (e) Fd=0.25
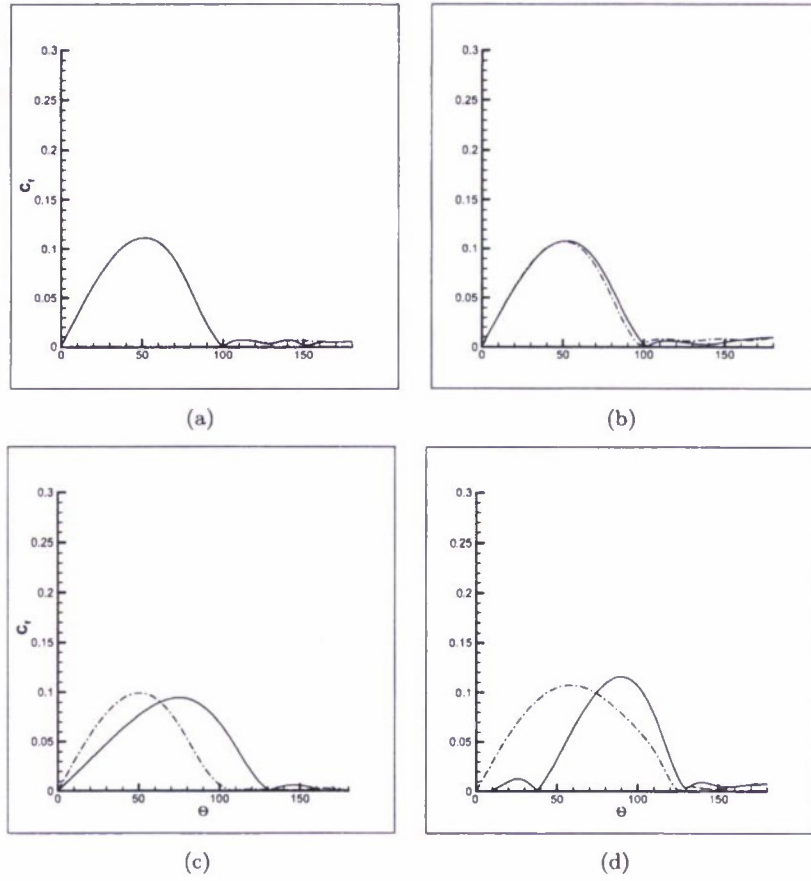
Figure 4.19: Re=1000, Sc=1: Surface skin friction coefficient, C_f, vs. angle, θ, in the $(-)$ vertical$(z \geq 0)$ and $(- \cdot -)$ horizontal $(y \leq 0)$ plane. θ is taken from the negative x-axis. (a) Fd=∞ (b) Fd=2 (c) Fd=0.50 (e) Fd=0.25
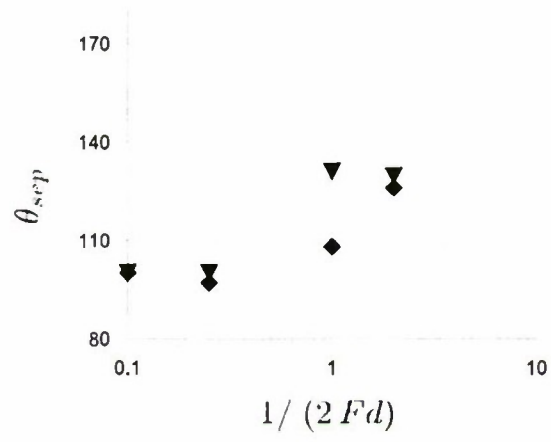
Figure 4.20: Re=1000, Sc=1: Separation point location vs. $1/(2\,Fd)$. ($\triangledown$) vertical, ($\diamond$) horizontal.
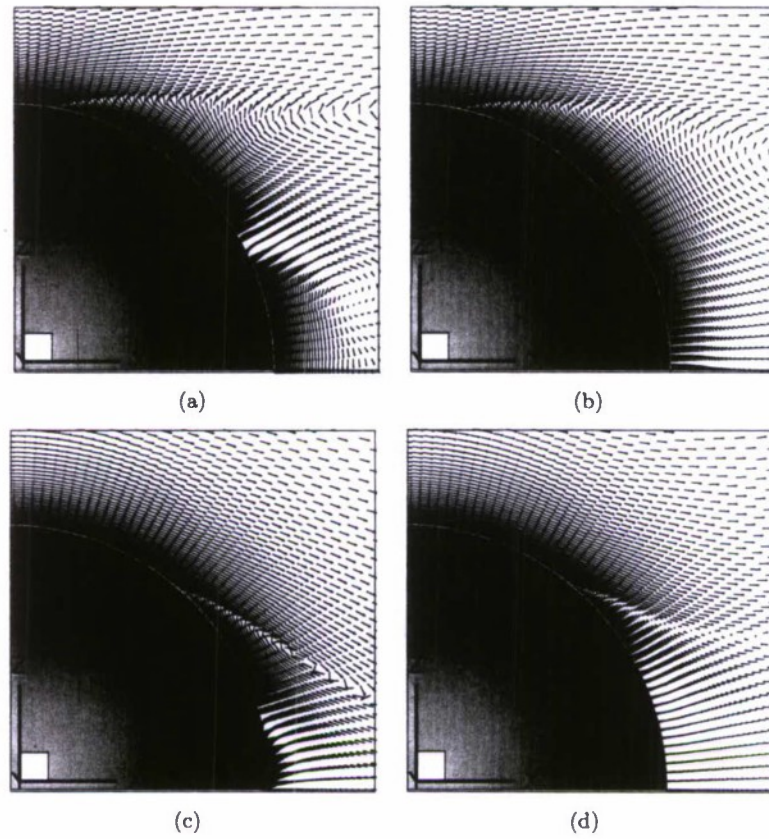
Figure 4.21: Re=1000, Sc=1: Instantaneous vectors in vertical plane ($z \geq 0$) on lee side of sphere. (a) Fd=∞ (b) Fd=2 (c) Fd=0.50 (d) Fd=0.25
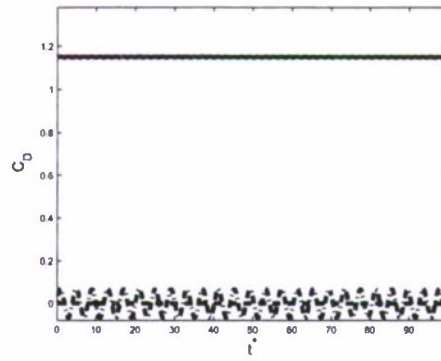
Figure 4.22: Re=1000, Sc=1, Fd=0.25: Drag coefficient time series. $- C_{D_X}$, $- \cdot - C_{D_Y}$, $- - C_{D_Z}$.
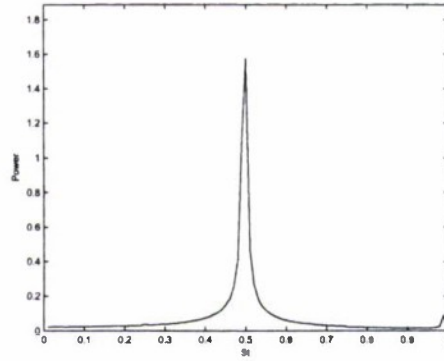
Figure 4.23: Re=1000, Sc=1, Fd=0.25: Drag coefficient power spectra. $- C_{D_x}$, $- \cdot - C_{D_y}$, $--$ C_{D_z}.

(a)

(b)
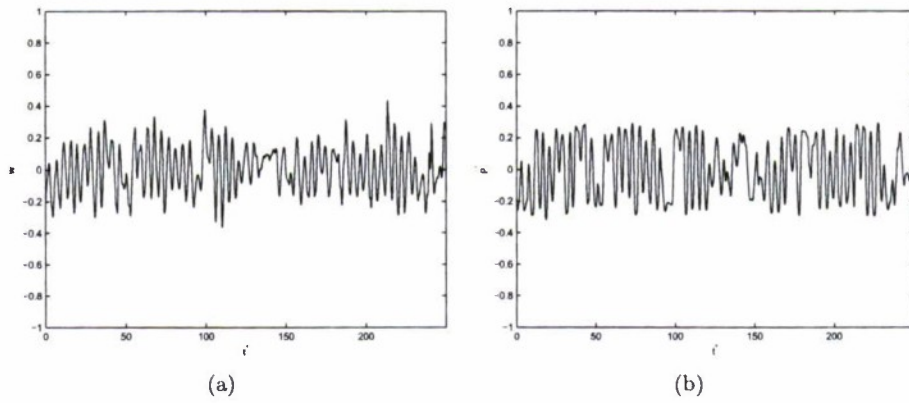
Figure 4.24: Re=1000, Sc=1, Fd=2: Time history of data signal at x/D≃2. (a) w (b) ρ'

(a)

(b)
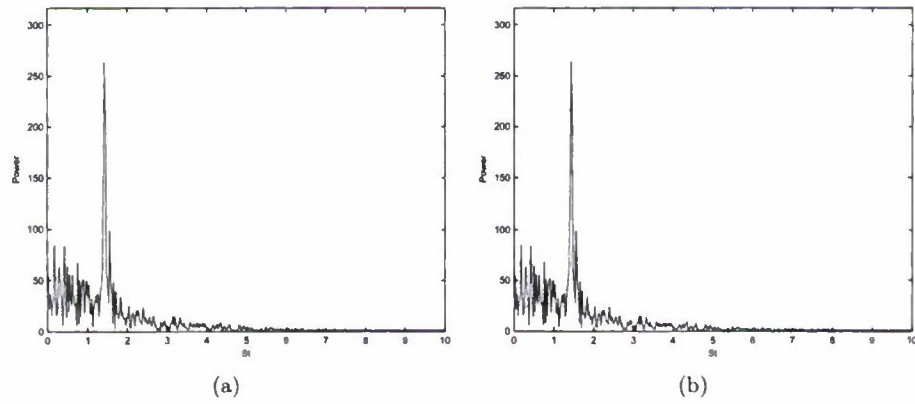
Figure 4.25: Re=1000, Sc=1, Fd=2: Power spectra of data signal at x/D≃2. (a) w (b) ρ'

43
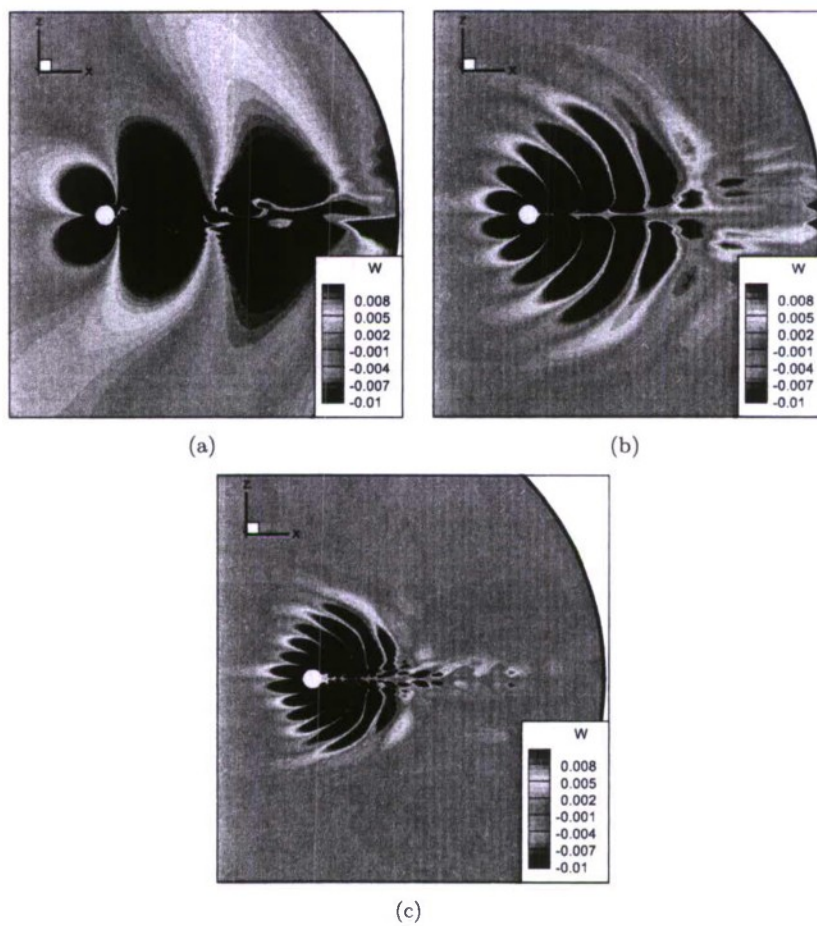
Figure 4.26: Re=1000, Sc=1: Contours of vertical velocity, w. Levels are between $\pm.01$ in increments of 0.001. (a) Fd=2, (b) Fd=0.50, (c) Fd=0.25
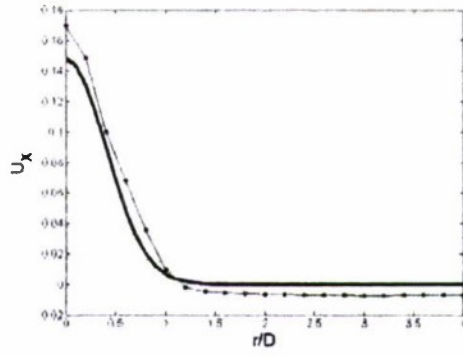
Figure 4.27: Re=5000, Sc=1, Fd=2: Azimuthally averaged stream-wise velocity profile. $- \cdot -$ Orr '10, $-$ Diamessis '05. (i.c.)
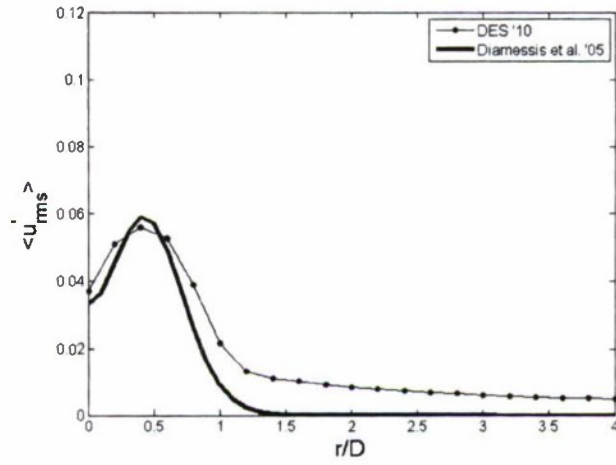
Figure 4.28: Re=5000, Sc=1, Fd=2: Azimuthally and spatially averaged (u_i') velocity profile at $(1/Fd)(x/D) = 3$. $(- \cdot -)$ Orr '10, $(-)$ Diamessis '05. (i.c.)
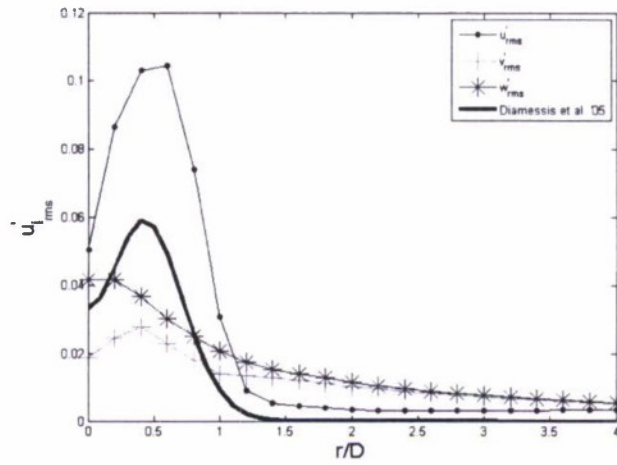
Figure 4.29: Re=5000, Sc=1, Fd=2: Azimuthally and spatially averaged u'_i velocity profile at $(1/Fd)(x/D) = 3$. $(\langle u' \rangle, \langle v' \rangle, \langle w' \rangle)$ Orr '10, $(-)$ Diamessis '05. (i.c.)
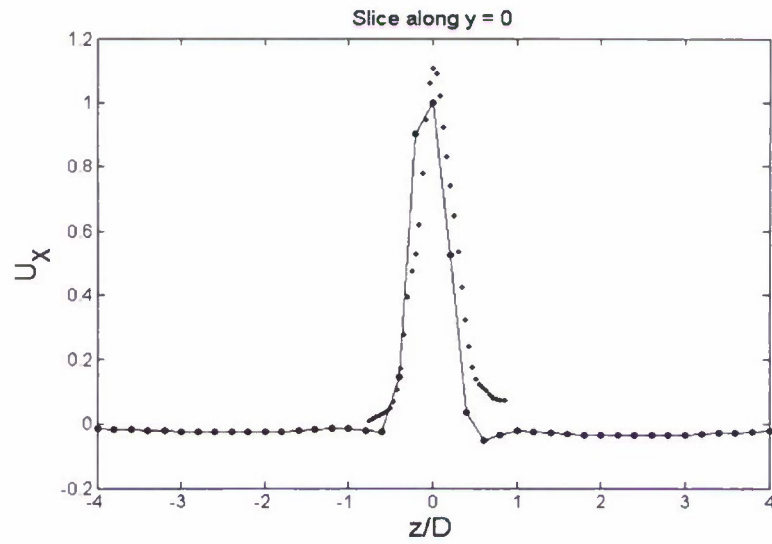
Figure 4.30: Re=5000, Sc=1, Fd=2: Spatially averaged u_x velocity profile in vertical center-plane $(y = 0)$ at $(1/Fd)(x/D) = 3$. $(- \cdot -)$ Orr '10, $(\cdot)$ Spedding

46
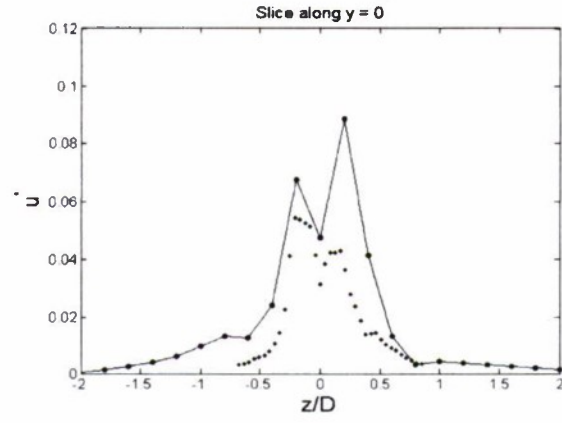
Figure 4.31: Re=5000, Sc=1, Fd=2: Spatially averaged u' velocity profile in vertical center-plane $(y = 0)$ at $(1/Fd)(x/D) = 3$. $(- \cdot -)$ Orr '10, $(\cdot)$ Spedding
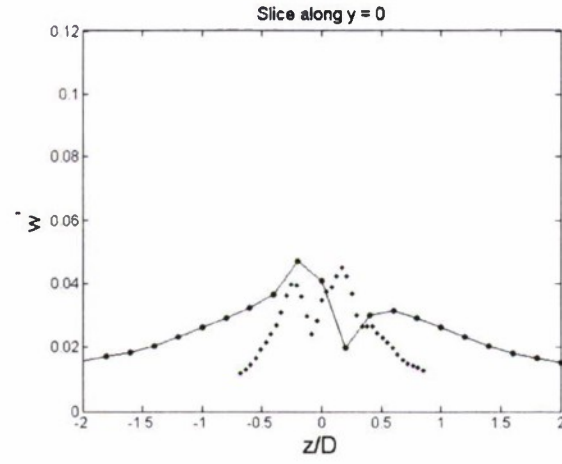
Figure 4.32: Re=5000, Sc=1, Fd=2: Spatially averaged w' velocity profile in vertical center-plane $(y = 0)$ at $(1/Fd)(x/D) = 3$. $(- \cdot -)$ Orr '10, $(\cdot)$ Spedding
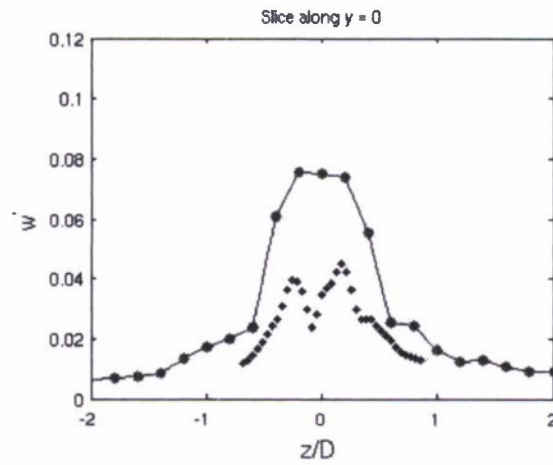
Figure 4.33: Re=5000, Sc=1, Fd=2: Example of SA-DES RANS damper affect on w' velocity profile in vertical center-plane ($y = 0$) at $(1/Fd)(x/D) = 3$. $(- \cdot -)$ Orr '10, $(\cdot)$ Spedding
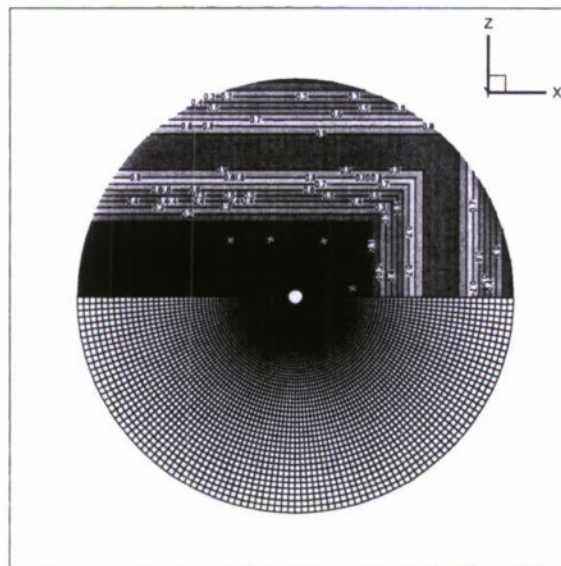
Figure 4.34: Example of viscous damping layer region in the vertical plane ($z \geq 0$); 0 indicates no damping, 1 indcates full damping. Mesh density visible in vertical plane ($z \leq 0$) for qualitative comparison.

48
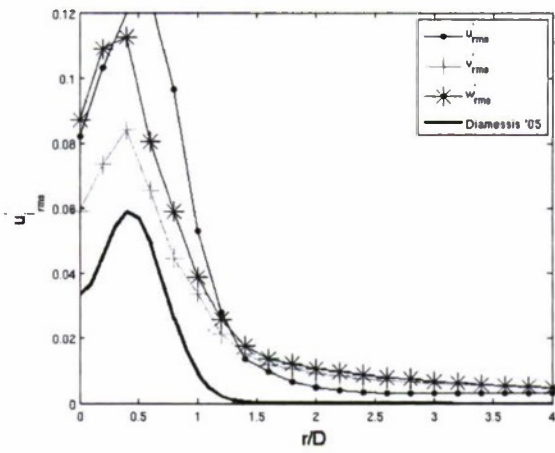
Figure 4.35: Re=5000, Sc=1, Fd=2: Example of viscous damper affect on w' velocity profile in vertical center-plane $(y = 0)$ at $(1/Fd)(x/D) = 3$. $(- \cdot -)$ Orr '10, $(\cdot)$ Spedding

Bibliography

[1] A. Arnone, M.S. Liou, and L.A. Povinelli. Integration of Navier-Stokes equations using dual time stepping and a multigrid method. *AIAA Journal*, 33:985–990, 1995.

[2] P.G. Baines. Upstream blocking and airflow over mountains. *Annual Review of Fluid Mechanics*, 19:75–97, 1987.

[3] P.M Bevilaqua and P.S. Lykoudis. Tubulence memory in self-preserving wakes. *Journal of Fluid Mechanics*, 89:589–606, 1978.

[4] P. Bonneton, J.M. Chomaz, E.J. Hopfinger, and M. Perrier. The structure of the turbulent wake and the random internal wave field generated by a moving sphere in a stratified fluid. *Dynamics of Atmospheres and Oceans*, 23:299–308, 1996.

[5] M. Bonnier, P. Bonneton, and O. Eiff. Far-wake of a sphere in a stably stratified fluid: Characterization of the vortex structures. *Applied Scientific Research*, 59:269–281, 1998.

[6] M. Bonnier, O. Eiff, and P. Bonneton. On the density structure of far-wake vortices in a stratified fluid. *Dynamics of Atmospheres and Oceans*, 31:117–137, 2000.

[7] K.A. Brucker and S. Sarkar. A comparative study of self-propelled and towed wakes in a stratified fluid. *Journal of Fluid Mechanics*, 652:373–404, 2010.

[8] J. D. Chashechkin and H. J. Sysoeva. Fine structure and symmetry of the wake past a sphere in a stratified liquid. *Proceedings of 17th Session of B.S.H.C.*, 1:10–1, 1988.

[9] J.M. Chomaz, P. Bonneton, and E.J. Hopfinger. The structure of the near wake of a sphere moving horizontally in a stratified fluid. *Journal of Fluid Mechanics*, 254:1–21, 1993.

[10] J.M. Chomaz, P. Bonneton, M. Perrier, and E.J. Hopfinger. Froude number dependence of the flow separation line on a sphere towed in a stratified fluid. *Physics of Fluids*, 4:254–258, 1992.

[11] G.S. Constantinescu, M. Chapelet, and K.D. Squires. Turbulence modeling applied to flow over a sphere. *AIAA Journal*, 41:1733–1742, 2003.

[12] G.S. Constantinescu and V.C. Patel. Numerical model for simulation of pump-intake flow and vortices. *Journal of Hydraulic Engineering*, 124:123–134, 1998.

[13] G.S. Constantinescu and K.D. Squires. LES and DES investigations of turbulent flow over a sphere at re = 10,000. *Flow, Turbulence and Combustion*, 70:267–298, 2003.

[14] G.S. Constantinescu and K.D. Squires. Numerical investigations of flow over a sphere in the subcritical and supercritical regimes. *Physics of Fluids*, 16:1449–1466, 2004.

[15] P.J. Diamessis, J.A. Domaradzki, and J.S. Hesthaven. A spectral multidomain penalty method model for the simulation of high reynolds number localized incompressible stratified turbulence. *Journal of Computational Physics*, 202:298–322, 2005.

[16] D.G. Dommermuth, Rottman J.W., G.E. Innis, and E.A. Novikov. Numerical simulation of the wake of a towed sphere in weakly stratified fluid. *Journal of Fluid Mechanics*, 473:83–101, 2002.

[17] P.G. Drazin. On the steady flow of a fluid of variable density over an obstacle. *Tellus*, 8:239–251, 1961.

[18] D. Givoli. High-order local non-reflecting boundary conditions: a review. *Wave Motion*, 39:319–326, 2004.

[19] M.P. Gresho and R.L. Sani. On pressure boundary conditions for the incompressible Navier-Stokes equations. *International Journal for Numerical Methods in Fluids*, 7:1111–1145, 1987.

[20] G. Haller. Exact theory of unsteady separation for two-dimensional flows. *Journal of Fluid Mechanics*, 512:257–311, 2004.

[21] H. Hanazaki. A numerical study of three-dimensional stratified flow past a sphere. *Journal of Fluid Mechanics*, 192:393–419, 1988.

[22] H. Hanazaki, K. Konishi, and T. Okamura. Schmidt-number effects on the flow past a sphere moving vertically in a stratified diffusive fluid. *Physics of Fluids*, 21:1–8, 2009.

[23] E.J. Hopfinger, J.-B. Flor, J.-M. Comaz, and P. Bonneton. Internal waves generated by a moving sphere and its wake in a stratified fluid. *Experiments in Fluids*, 11:255–261, 1991.

[24] M. Israeli and S. A. Orszag. Approximation of radiation boundary conditions. *Journal of Computational Physics*, 41:115–135, 1981.

[25] T.A. Johnson and V.C. Patel. *Flow past a sphere up to a Reynolds number of 300*. PhD thesis, University of Iowa, 1999.

[26] Pijush Kundu and Ira Cohen. *Fluid Mechanics, Third Edition*. Elsevier Inc., 2004.

[27] S. Lee. A numerical study of the unsteady wake behind a sphere in a uniform flow at moderate reynolds numbers. *Computers & Fluids*, pages 639–667, 2000.

[28] James Lighthill. *Waves in Fluids*. Cambridge University Press, New York, NY, 1978.

[29] D.K. Lilly. The representation of small-scale turbulence in numerical simulation experiments. In *Proc. IBM Sci. Comput. Symp. Environ. Sci.*, pages 195–210, White Plains, N.Y., 1967. IBM Data Process. Div.

[30] J.T. Lin and Y.H. Pao. Wakes in stratified fluids. *Annual Review of Fluid Mechanics*, 11:317–338, 1979.

[31] Q. Lin, D.L. Boyer, and H.J.S. Fernando. Turbulent wakes of linearly stratified flow past a sphere. *Physics of Fluids A*, 4:1687–1696, 1992.

[32] Q. Lin, W.R. Lindberg, D.L. Boyer, and H.J.S. Fernando. Stratified flow past a sphere. *Journal of Fluid Mechanics*, 240:315–354, 1992.

[33] Vladimir Liseikin. *Grid Generation Methods*. Springer, 1999.

[34] K.E. Lofquist and L.P. Purtell. Drag on a sphere moving horizontally through a stratified liquid. *Journal of Fluid Mechanics*, 148:271–284, 1984.

[35] P. Meunier and G.R. Spedding. A loss of memory in stratified momentum wakes. *Physics of Fluids*, 16(2):298–305, February 2004.

[36] P. Meunier and G.R. Spedding. Stratified propelled wakes. *Journal of Fluid Mechanics*, 552:229–256, 2006.

[37] N.V. Nikitin, F. Nicoud, B. Wasistho, K.D. Squires, and P.R. Spalart. An approach to wall modeling in large-eddy simulations. *Physics of Fluids*, 12(7):1629–1632, July 2000.

[38] H.-P. Pao and T.W. Kao. Vortex structure in the wake of a sphere. *The Physics of Fluids*, 20:187–191, 1977.

[39] L. Prandtl. Über flüssigkeitsbewegung bei sehr kleiner reibung. *Int. Math. Kongr. Heidelberg*, pages 484–451, 1904.

[40] H. Schlichting. *Boundary-Layer Theory*. McGraw-Hill Book Company, 7 edition, 1979.

[41] A. H. Schooley and R. W. Stewart. Experiments with a self-propelled body submerged in a fluid with a vertical density gradient. *Journal of Fluid Mechanics*, 9:83–96, 1963.

[42] W.R. Sears and D.P. Telionis. Boundary-layer separation in unsteady flow. *SIAM Journal on Applied Mathematics*, 28:215–235, 1975.

[43] P.A. Sheppard. Airflow over mountains. *Quarterly Journal of the Royal Meteorological Society*, 82:528–529, 1956.

[44] M. Shur, P.R. Spalart, M. Strelets, and A. Travin. Detached-eddy simulation of an airfoil at high angle of attack. In *Proceedings of 4th international symposium on engineering turbulence modelling and measurements*. Elsevier, May 1999.

[45] F. Sortiropoulos. *A primitive variable method for the solution of external and internal incompressible flow-fields*. PhD thesis, University of Cincinnati, 1991.

[46] F. Sortiropoulos and S. Abdallah. The discrete continuity equation in primitive variable solutions of incompressible flow. *Journal of Computational Physics*, 95:212–227, 1991.

[47] P.R. Spalart and S.R. Allmaras. A one-equation model for aerodynamic flows. *La Recherch Aerospatiale*, 1:1, 1994.

[48] P.R. Spalart, W-H. Jou, M. Strelets, and S.R. Allmaras. Comments on the feasibility of les for wings, and on a hybrid rans/les approach. In *1st AFOSR Int. Conf. on DNS/LES*. 1st AFOSR Int. Conf. on DNS/LES, Aug. 4-8 1997.

[49] G.R. Spedding. The evolution of initially turbulent bluff-body wakes at high internal froude number. *Journal of Fluid Mechanics*, 337:283–301, 1997.

[50] M. Strelets. Detached eddy simulation of massively separated flows. In *39th AIAA Aerospace Sciences Meeting and Exhibit*. 39th AIAA Aerospace Sciences Meeting and Exhibit, Jan. 8-11 2001.

[51] E. Ya. Sysoeva and Yu. D. Chashechkin. Vortex structure of a wake behind a sphere in a stratified fluid. *J. Appl. Mech. Theor. Phys. (Novosibirsk)*, 2:190–196, 1986.

[52] S. Taneda. Experimental investigation of the wake behind a sphere at low reynolds numbers. *Journal of the Physical Society of Japan*, 11:1104–1108, 1956.

[53] T. Tantikul and J.A. Domaradzki. Large eddy simulations using truncated Navier-Stokes equations with the automatic filtering criterion. *Journal of Turbulence*, 11, 2010.

[54] L.L. Van Dommelen and S.J. Cowley. On the lagrangian description of unsteady boundary-layer separation. part1. general theory. *Journal of Fluid Mechanics*, 210:593–626, 1990.

[55] D. Wilcox. *Turbulence Modeling for CFD*. DCW Industries, Inc., 1998.

Large eddy simulations using truncated Navier–Stokes equations with the automatic filtering criterion

T. Tantikul* and J.A. Domaradzki

Department of Aerospace and Mechanical Engineering, University of Southern California, Los Angeles, CA, 90089-1191, USA

We propose a large eddy simulation (LES) technique based on the previously developed Trancated Navier–Stokes (TNS) method. In TNS, the Navier–Stokes equations are solved through a sequence of direct numerical simulation runs and a periodic processing of small scales to provide the necessary dissipation. In the simplest case, the processing is accomplished by filtering the turbulent fields with a properly chosen filter. In the previous work, the period for processing was selected in advance for each case using heuristic arguments validated by trial and error. In this work, we develop a criterion that automates the selection of a time instant in simulations when the processing occurs. The criterion is based on the relationship between the energy of the flow field and the energy of the same field filtered with the chosen filter. The procedure is tested in LES of the turbulent channel flow performed at various Reynolds numbers and in domains of different sizes for which Direct Numerical Simulations (DNS) and experimental data are available for comparisons.

Keywords: large eddy simulations; truncated Navier–Stokes equations; explicit filtering; automatic filtering criterion

1. Introduction

Several classifications of the subgrid-scale (SGS) models for large eddy simulations (LES) have been proposed in the literature on the subject. In a review paper of Domaradzki and Adams [1], the SGS models are divided into two general categories: the traditional models that use the explicit expressions for the SGS terms, the SGS stress tensor in particular and the models that construct the unknown primitive variables, such as velocity, in order to use these variables to compute the SGS terms directly from the definitions. The traditional SGS modeling approaches can be subdivided into three groups: the eddy viscosity models, the similarity models and the mixed models. The examples of the models in the other group are the velocity estimation model proposed by Domaradzki et al. [2,3] and Stolz et al.'s [4] approximate deconvolution model (ADM). Kosovic et al. [5], characterized by the use of explicit filtering, divided SGS models into three groups. First are the models that use an explicit SGS expression but do not employ explicit filtering; for instance, the classical Smagorinsky eddy viscosity model. Second are the models that use an explicit SGS expression and employ explicit filtering, e.g. the dynamic Smagorinsky model. The third category are the so-called implicit models because equations of motion are solved without

---

*Corresponding author. Email: tantikul@usc.edu

neither explicit filtering nor explicit SGS terms. Such approaches rely on the properties of the numerical scheme to provide implicit dissipation and are known as the Monotone Integrated Large Eddy Simulations (MILES) or the Implicit Large Eddy Simulations (ILES). An in depth review of the ILES is given in the monograph edited by Grinstein et al. [6]. For high-order, nondissipative numerical schemes, this classification can be extended to include models that do not use the explicit SGS terms but employ the explicit filtering to model the effects of the SGS dissipation. The modeling approach discussed in this paper belongs to this group and originated from the SGS velocity estimation model proposed by Domaradzki and Saiki [2]. The model was developed in spectral space representation and later implemented in the physical space by Domaradzki and Loh [7].

The original velocity estimation model encountered difficulties in the LES of high Reynolds number flows because it did not produce enough SGS dissipation. To address this shortcoming, Domaradzki et al. [3] have introduced the modification of the velocity estimation model that solves LES equations in parallel with the Truncated Navier–Stokes (TNS) equations on a finer mesh; TNS provides the estimated velocity that is used to compute the SGS stress tensor needed in LES. More specifically, the TNS equations are just Navier–Stokes equations discretized on a mesh by a factor of two smaller than the LES equations of interest. The estimated velocity to be advanced in TNS is obtained in two steps. First, the velocity from LES is 'de-filtered', providing large-scale velocity represented on a coarse LES mesh. Second, the small-scale perturbation velocity is created by nonlinear interaction of the reconstructed field. The total estimated velocity is a sum of both parts and is represented on a finer TNS mesh. The estimated velocity is advanced in time using TNS equations, i.e. using a Navier–Stokes solver on the fine mesh. The velocity field from TNS is then used at each time-step to the SGS stress model directly from the TNS field, and this stress model is used to advance in time the LES equations. This process of two parallel runs is continued for some fixed time period T until the accumulation of energy in the small scales of the TNS begins to affect the large scales. To assure the accurate large-scale results, the whole process has to be reinitialized every time period T, with reduced energy in the small-scale region obtained by a low-pass filter. The results from LES for homogeneous turbulence and turbulent channel flow test cases are in a very good agreement with the Direct Numerical Simulations (DNS) and the experimental data. The disadvantage of this approach is that the procedure is quite complicated and requires more computational time compared to other the LES modeling approaches because additional TNS equations must be solved. However, a significant speed up of computations is possible for a simplified version of the model that employs only the TNS equations as shown by Domaradzki et al. [3]. Such a simplification is based on the observation that the TNS velocity on the fine mesh already contains information about large scales of the flow and thus the LES equations are redundant. Since the small scales of TNS fields are subjected to periodic filtering, the physical meaning is ascribed only to the large TNS scales given on the coarse LES mesh. In this approach the estimated small-scale velocity field provides the SGS effects on the large scales via nonlinear interactions in the Navier–Stokes equations. The approach is less complicated in terms of the numerical implementation and retains the same quality of the results as the original method. However, the user still needs to specify the time period T for filtering and re-initialization of the TNS in order to prevent the accumulation of energy in the small scales and the resulting error propagating toward the large scales and contaminating them. Our goal in this work is to investigate a procedure that determines the time period T automatically, without a need to provide its value as a parameter by the user. Once the procedure is defined in the next section it will be subsequently tested in LES of the turbulent channel flow problem in the following sections.

The explicit filtering as a LES tool has been employed in different forms previously, usually as a method to control numerical instabilities. Visbal and Rizzetta [8], [9] studied the application of a high-order finite difference method to the LES of compressible flows. They used fourth- and sixth-order compact differencing schemes for spatial discretization and different explicit and implicit time marching methods. The simulations were performed with the unfiltered Navier–Stokes equations and the high-order, Pade-type, low-pass spatial filter was employed at each time-step to remove spurious high-frequency modes which arise because of the lack of the dissipation in the spatial discretization. It was found that the compact/filtering scheme performed better or comparably to the constant coefficient and dynamic Smagorinsky models for a number of different turbulent flows. Bogey and Bailly [10] investigated jet flows using LES with explicit filtering. The numerical simulations were performed using a low-dissipation numerical scheme with the explicit fourth-order 13-point centered finite differences for spatial discretizations and the second-order six-stage low-storage Runge–Kutta algorithm for time integration. The explicit selective/high-order filtering was employed to emulate the dissipative effects of the neglected SGS. Interestingly, the filtering was not applied at every time-step but every second or third time-step. The results from the simulations with the filtering applied at every two or three iterations exhibit no relationship between the frequency of application of the filtering and the quality of the results. When spectral methods, which have negligible numerical dissipation, are employed to simulate high Reynolds number flows, explicit filters and penalty techniques must be used to stabilize numerics, e.g. in Diamessis et al. [11], and in Minguez and Pasquetti [12]. Such methods are known as the stabilized LES and use filtering at each time step. The numerical dissipation associated with one of these methods has been investigated recently by Diamessis et al. [13]. In using such techniques one must recognize that achieving numerical stability does not necessarily imply physically correct results. Therefore, such techniques must always be validated by comparing results they produce with experiments and DNS results.

In the work described here, we use spectral methods stabilized by the weak, explicit filter applied at each time step and much less frequent periodic filtering that is used not as a stabilization tool but primarily as an SGS modeling tool based on physical considerations of the energy transfer and the spectra in developed turbulence.

2. Filtering and filtering criterion

In LES, the filtering operation is applied to a full and turbulent velocity field, to separate it into the large, resolved scales and the small SGS. Ideally, the filter should retain complete information about the large scales and substantially remove or attenuate the small scales, allowing the user to focus the computational power on the large scales. Since the computational space in the simulations is discrete, filters are given in the discrete form as well. A convenient filter with desirable properties has been proposed by Stolz et al. [4] for the Approximate Deconvolution Model (ADM). If G represents the primary filter used, the filtering operation can be written in the physical space as

$$\bar{u}(x) = G * u = \int_{-\infty}^{\infty} G(x - x')u(x')dx' \tag{1}$$

and in the spectral space as

$$\hat{\bar{u}}(k) = \hat{G}(k)\hat{u}(k), \tag{2}$$

where u is the one-dimensional velocity component, $\bar{u}$ is the filtered velocity, $G(x)$ is the filter kernel in the physical space and $\hat{G}(k)$ is the filter kernel or the filter transfer function in Fourier space. The approximate deconvolution of the primary filter is given as

$$Q_N \approx G^{-1} = \sum_{\nu=0}^{N} (I - G)^{\nu}. \tag{3}$$

The secondary filter, which affects only the small resolved scales, is constructed in ADM as a product of Q_N and G [4] and the corresponding filtered velocity is expressed as follows:

$$\tilde{u} = (Q_N G) * u. \tag{4}$$

The numerical evaluation of the filter operation, Equation (1), requires the quadrature rule. We select the box filter with filter width Δ as the primary filter and the trapezoidal integration rule and $\Delta = 2h$ for physical LES scales. For this choice, the one-dimensional transfer function is

$$\hat{G}(k) = \frac{1}{2}(1 + \cos kh). \tag{5}$$

The discrete filter on equidistant mesh in the x direction is

$$\bar{u}(x_i) = d_0^u u(x_i) + \sum_{l=-1, l \neq 0}^{1} d_l^u u(x_{i+l}), \tag{6}$$

where d_l^u are filter coefficients computed by Loh et al. [14] using the numerical integration with trapezoidal rule over interval Δ spanning three neighboring points on a uniform mesh, i.e. $\Delta = 2h$, where Δ is the filter width. The filtering in the simulations is done sequentially in each Cartesian direction. For the nonuniform mesh in the vertical direction, the discrete filter has the same form as given in Equation (6) but the filter coefficients are different, d_l^n, with the explicit formulas given in Loh et al. [14].

Jeanmart and Winckelmans [15] proposed a significant simplification of the filtering procedure in Equation (4), which dispenses entirely with the the Van Cittert approximate deconvolution in Equation (3). Indeed, using the formula for the sum of a geometric sequence

$$\sum_{\nu=0}^{N} r^{\nu} = \frac{1 - r^{N+1}}{1 - r}, \quad r \neq 1, \tag{7}$$

Equation (3) is expressed formally as

$$Q_N = \frac{I - (I - G)^{N+1}}{G}, \tag{8}$$

and the transfer function of the ADM filter in Equation (4) becomes

$$Q_N G = I - (I - G)^{N+1}, \tag{9}$$

i.e. the ADM filter $Q_N G$ on the LHS is easily implemented through the recursive application of the $(I - G)$ filter on the RHS. Also, the Equation (5), which is the transfer function of the stencil-3, second-order filter, can be rearranged as follows:

$$\hat{G}(k) = 1 - \left(\frac{1 - \cos(kh)}{2} \right) = 1 - \sin^2 \left(\frac{kh}{2} \right), \tag{10}$$

which immediately leads to the expression for the transfer function for the ADM filter (9)

$$(\widehat{Q_N G})(k) = 1 - \sin^{2(N+1)} \left(\frac{kh}{2} \right). \tag{11}$$

Equation (11) is the transfer function of the high-order filter obtained from the recursive application of the stencil-3, low-order filter $(I - G)$. This filter can be applied sequentially in each direction in three-dimensional space. In particular, the 1-D filter selected in this work is $Q_5 G$, with the transfer function $(1 - \sin^{12}(kh/2))$.

In a simulation with general finite difference schemes, the inability to represent the high wave number modes accurately results in the undesired dispersion error. This error causes unphysical and rapid oscillations in the marginally resolved regions, which may lead to numerical instabilities and a break down of the simulation. To eliminate such spurious modes an artificial dissipation through additional damping terms is usually employed. The spectral methods used in this work are well known for high accuracy or spectral convergence. However, spectral convergence is achieved only when the spectral methods are applied to sufficiently smooth problems. The loss of fast convergence for the problems that have potential to develop non-smooth solutions in finite time undermines the advantages of spectral methods. Gottlieb and Hesthaven [16] reported the use of spectral filters acting in a similar fashion as additional dissipative terms that help to stabilize simulations without affecting the spectral convergence. Besides the ability to retain the spectral convergence and stabilize the simulation, the filtering also decreases the aliasing errors. According to Gottlieb and Hesthaven [16], there is no unique choice of the filter function as long as certain basic requirements are satisfied. The baseline DNS code employed for simulations in this work has been developed by Diamessis et al. [11] and employs the exponential filter

$$\sigma(k) = \begin{cases} 1, & 0 \le k \le k_l \\ \exp\left[-\alpha \left(\frac{k - k_l}{N - k_l} \right)^p \right], & k_l \le k \le N, \end{cases} \tag{12}$$

where p is the filter order, N is the highest mode in the spectral domain, k_l is the filter lag and $\alpha = -\log \epsilon_M$ with ϵ_M being the machine precision. The filter in Equation (12) is intentionally selected such that it affects only the high-frequency modes and its purpose is only to stabilize the numerical simulation and enhance the convergence rate of the approximation.

The filtered solution f^F may now be expressed in terms of the modes in Legendre space of the numerical solution as

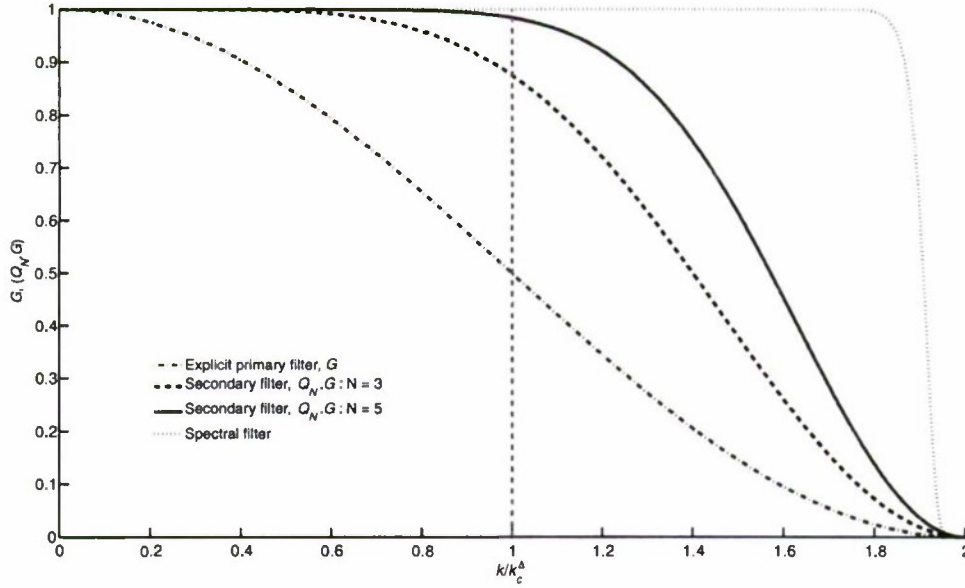$$f^F = \sum_{j=0}^{N_{k-1}} \sigma(k_j) \tilde{f}_j P_j(z_j), \tag{13}$$

Figure 1. One-dimensional transfer function. Dash-dot line: explicit primary filter; dashed line: secondary filter with N = 3; solid line: secondary filter with N = 5; dotted line: spectral filter as in Equation (12).

where k_j is the *jth* discrete Legendre mode. The filtering in Fourier space is done in the similar fashion [16].

Transfer functions for different filters described above are shown in Figure 1. By design, the exponential filter affects only modes in the vicinity of the mesh cutoff. The secondary filter in Equation (4) with N = 5 retains almost all information for scales $k \leq k_c^\Delta$, where $k_c^\Delta = \pi/(\Delta)$ is the nominal cutoff wave number for the physical LES scales. This is the an important characteristic of the secondary filter compared with other candidate filters and is chosen on this basis for the current work. The scales between k_c^Δ and the mesh cutoff $k_c^h = \pi/h$ are strongly attenuated by the filter and play a role of the estimated SGS in TNS.

The TNS equations are equivalent to the under-resolved DNS stabilized by the exponential filter given in Equation (12). In the under-resolved DNS, the energy begins to accumulate in small scales and the long-time dynamics will be incorrect. The velocity estimation model [3] removes this accumulated energy by periodic filtering with the secondary filter of the form given in Equation (4). The time interval between applications of the filter has to be manually prescribed by the user in advance. The method would gain in generality if the filtering operation could be activated automatically based on a physically established criterion.

To establish such a criterion, the combinations of an energy spectrum $E(k)$ for the full turbulent velocity field and two secondary filters are theoretically considered. The secondary filters are built from the primary filters with different filter widths. We choose two filter widths, h and Δ, where h is the mesh size used in the simulation and $\Delta = 2h$. The filter width h is related to the grid cutoff wave number, k_c^h, by the relation $k_c^h = \pi/h$, and the filter width $\Delta = 2h$ is related to the LES cutoff wave number, k_c^Δ, by the relation $k_c^\Delta = \pi/(\Delta)$. The filtered quantities obtained using the filters corresponding to the cutoff wave numbers k_c^h and k_c^Δ are denoted by tilde and hat, respectively. Figure 2 shows the attenuated spectra of the inertial, dissipation and k^{-1} ranges. If the velocity field is filtered
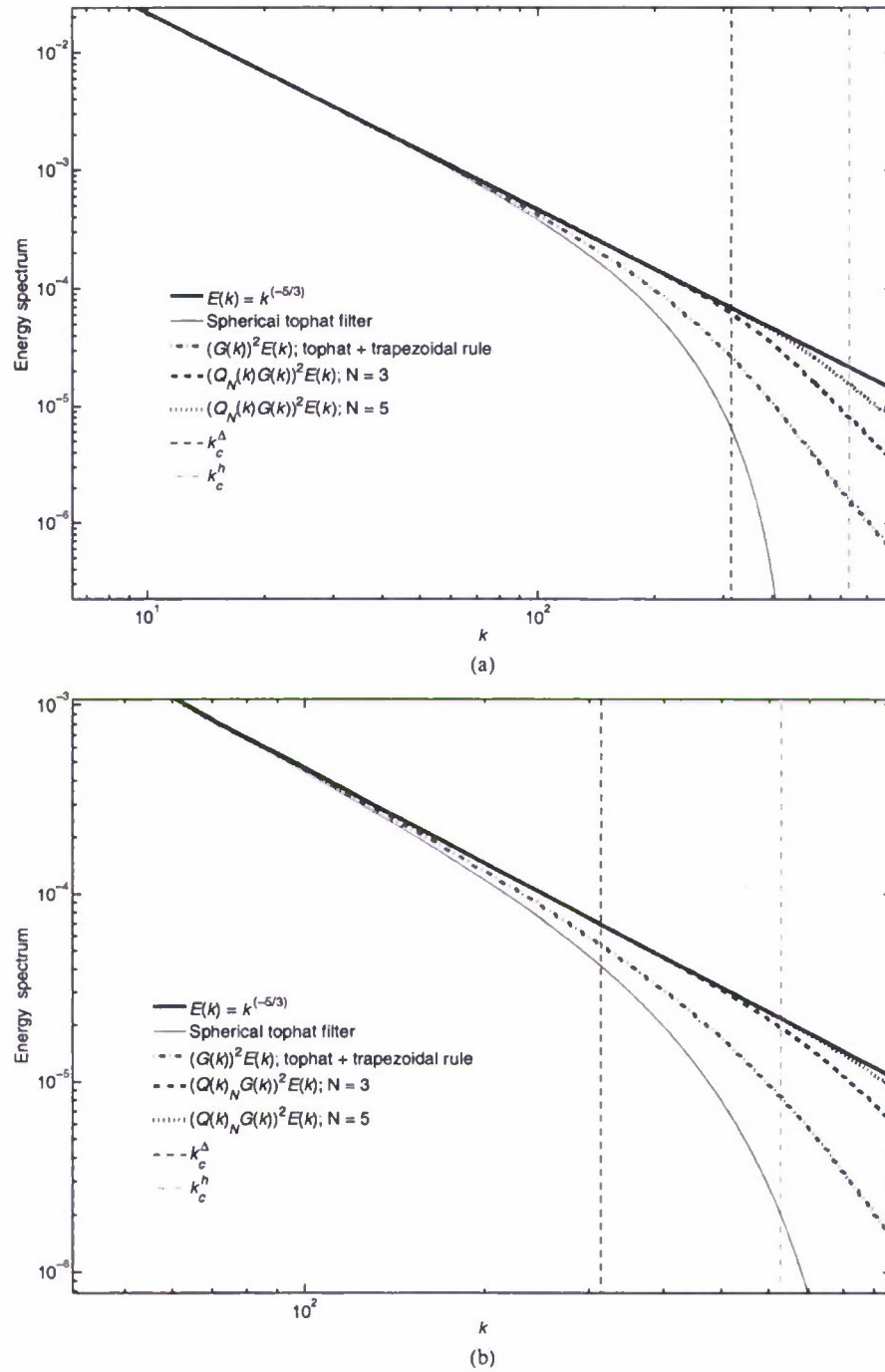
Figure 2. Energy spectrum plot of the infinite inertial range. Thick solid line: energy spectrum; thin solid line: filtered energy spectrum with spherical tophat filter; dotted line: filtered energy spectrum with secondary filter, $N = 5$; dashed line: filtered energy spectrum, $N = 3$; dash-dot: filtered energy spectrum with primary filter; vertical dashed line: k_c^Δ; vertical dash-dot line: k_c^h (a) energy spectrum plot with the filtered energy spectrum; filter with filter width Δ, and (b) energy spectrum plot with the filtered energy spectrum; filter with filter width h.

Table 1.   Filtered energy ratios.

Energy spectrum	Secondary filter; $I(\Delta)$	N = 5 $I(h)$	$\frac{I(h)}{I(\Delta)}$
Dissipation	0.0896	0.0061767	0.00689363
Inertial	0.0234	0.00021466	0.009173504
Batchelor	0.0699	0.00068	0.009728183

with the former filter, the corresponding spectrum of the filtered field is denoted as $\tilde{E}(k)$ and the energy removed by the filtering in a range of wave numbers resolved in TNS up to $k_c^h = \pi / h$ is

$$I(h) = \int_0^{k_c^h} (E(k) - \tilde{E}(k))dk, \tag{14}$$

and the similar integral for the other filter. The expression

$$\frac{I(h)}{I(\Delta)} = \frac{\int_0^{k_c^h} (E(k) - \tilde{E}(k))dk}{\int_0^{k_c^h} (E(k) - \hat{E}(k))dk} \tag{15}$$

is the ratio of energies removed by both filters in the range of wave numbers resolved in TNS. This ratio has been computed for the progressively shallower energy spectra, starting with the dissipation range spectrum form [17], the inertial range $k^{-5/3}$ spectrum and the Batchelor's k^{-1} spectrum. For illustration, in Figure 2(a) and (b) we plot the inertial range spectrum and the filtered energy spectra for two different filter widths. The results for the computed energy ratio are shown in Table 1. Depending on the spectrum, this ratio varies in the narrow range of between 0.007 and 0.010. We will use these bounds as guidelines to decide when the filtering in the simulations should be activated.

In actual TNS for turbulent channel flow, the energy ratio is computed from the simulation data using the formula

$$\left\langle \frac{I(h)}{I(\Delta)} \right\rangle_{SIM} (z) = \left\langle \frac{\frac{1}{2} \sum_{n=1}^3 [(\tilde{u}_n - \bar{\tilde{u}}_n)(\tilde{u}_n - \bar{\tilde{u}}_n)]}{\frac{1}{2} \sum_{n=1}^3 [(\tilde{u}_n - \hat{\tilde{u}}_n)(\tilde{u}_n - \hat{\tilde{u}}_n)]} \right\rangle_{SIM}, \tag{16}$$

where $\langle \rangle$ is a plane averaged quantity, followed by integrating it over z:

$$\left(\frac{I(h)}{I(\Delta)} \right)_{SIM} = \int_0^{L_z} \left\langle \frac{I(h)}{I(\Delta)} \right\rangle_{SIM} (z)dz. \tag{17}$$

When this last quantity exceeds the theoretical value $(I(h)/I(\Delta))_{Theory}$ from Table 2, it is an indication that the small scales in TNS become too energetic. Therefore, when

$$\left(\frac{I(h)}{I(\Delta)} \right)_{SIM} > \left(\frac{I(h)}{I(\Delta)} \right)_{Theory}, \tag{18}$$

the filtering will be activated to attenuate the small scales. Thus, this condition serves as the automatic filtering criterion in TNS.

3. Numerical simulations

The method is validated in this study by performing LES of the incompressible turbulent channel flow because of the wealth of the experimental and the DNS data that can be used for comparison. The fluid is contained between two solid walls separated by the distance L_z. The horizontal domain has the dimension L_x for the streamwise direction and L_y for the spanwise direction. The no-slip boundary conditions are imposed on the upper and lower walls and periodic boundary conditions are applied in the horizontal directions. The code uses a pseudospectral numerical method based on the Fourier expansions in the streamwise and the spanwise directions and the Legendre polynomials in the vertical direction (see [11]). In the numerical method used in this paper, the spectral filtering is applied in both the Fourier and the Legendre spaces to maintain the stability and spectral accuracy of the solutions, and also to help in eliminating the aliasing effects. The MPI-based parallel solver was employed in the numerical simulations presented in this paper. The assignment of different sections of the computational domain to individual processors is based on one-dimensional domain decomposition, which partitions the domain in distinct vertical slabs of thickness L_x/N_p and L_y/N_p, when operating in physical (Fourier) space, where N_p is the number of processors. The simulations were performed at the University of Southern California High Performance Computing Center's Linux cluster. In order to reduce the total computational time and cost caused by the interprocessor communication, the condition for the automatic filtering indicated in Equation (18) was checked at every 20 time steps, while the spectral filtering with the exponential filter given in Equation (12) was applied at every time step in the simulations.

The TNS equations are the standard Navier–Stokes equations for incompressible flows

$$\frac{\partial \tilde{u}_i}{\partial t} + \frac{\partial \tilde{u}_i \tilde{u}_j}{\partial x_i} = -\frac{1}{\rho}\frac{\partial \tilde{p}}{\partial x_i} + \nu \frac{\partial^2 \tilde{u}_i}{\partial x_j \partial x_j}, \tag{19}$$

$$\frac{\partial \tilde{u}_i}{\partial x_i} = 0, \tag{20}$$

where the tilde notation is used to indicate that the spectral support for a given quantity in discretized equations is not sufficient to capture all dynamically relevant scales of motion but is sufficient to resolve fields filtered with the filter given in Equation (4). The pressure term is decomposed into mean $P(x)$ and fluctuating component $\tilde{p}(\mathbf{x}, t)$. For a given, constant mean pressure gradient driving the flow, the statistically steady state is eventually established in which $\tau_0 = -\delta(dP/dx)$, where τ_0 is the wall shear stress and $\delta = L_z/2$ is the channel half width. By introducing the shear velocity $u_\tau = (\tau_0/\rho)^{1/2}$, the Navier–Stokes equations are rewritten as follows:

$$\frac{\partial \tilde{u}_i}{\partial t} + \frac{\partial \tilde{u}_i \tilde{u}_j}{\partial x_i} = -\left(\frac{1}{\rho}\frac{\partial \tilde{p}}{\partial x_i} - \frac{u_\tau^2}{\delta}\delta_{1i}\right) + \nu \frac{\partial^2 \tilde{u}_i}{\partial x_j \partial x_j}. \tag{21}$$

A statistically steady state is established much faster if the constant mass flux is imposed instead of the constant pressure gradient. The constant mass flux in the simulations is enforced by setting the mean pressure gradient to the instantaneous wall shear stress at each time step, which is equivalent to using in Equation (21) the following expression for u_τ

$$u_\tau(t) = \sqrt{-\nu \frac{\partial \langle \tilde{u}_1 \rangle}{\partial x_3}(L_z, t) + \nu \frac{\partial \langle \tilde{u}_1 \rangle}{\partial x_3}(0, t)}, \tag{22}$$

where $\langle \ldots \rangle$ indicates the plane averaged quantity. The above equations are normally nondimensionalized by the channel half width $\delta = L_z/2$ and the nominal friction velocity $u_0 = (\tau_0/\rho)^{1/2}$ for the constant pressure gradient case, i.e. $\tau_0 = -\delta(dP/dx)$, giving

$$\frac{\partial \tilde{u}_i}{\partial t} + \frac{\partial \tilde{u}_i \tilde{u}_j}{\partial x_i} = -\left(\frac{1}{\rho} \frac{\partial \tilde{p}}{\partial x_i} - u_\tau^2 \delta_{ij} \right) + \frac{1}{Re_0} \frac{\partial^2 \tilde{u}_i}{\partial x_j \partial x_j}, \tag{23}$$

$$\frac{\partial \tilde{u}_i}{\partial x_i} = 0, \tag{24}$$

where $Re_0 = \frac{u_0 \delta}{\nu}$ is the nominal Reynolds number. Note that the nominal Reynolds number Re_0 is used only as the parameter in the simulations and its value, while close, is usually different from the actual Reynolds number $Re_\tau = u_\tau \delta / \nu$ based on the actual friction velocity as shown in Equation (22). Only in the statistically steady state and in constant pressure gradient simulations $Re_0 = Re_\tau$. The actual friction velocity nondimensionalized by u_0 is

$$u_\tau(t) = \sqrt{-\frac{1}{Re_0} \frac{\partial \langle \tilde{u}_1 \rangle}{\partial x_3}(2, t) + \frac{1}{Re_0} \frac{\partial \langle \tilde{u}_1 \rangle}{\partial x_3}(0, t)}. \tag{25}$$

The parameters used in the simulations are gathered in Table 2 and the cases used for comparisons are collected in Table 3. The LES simulations were run until they reached the statistically steady state. In each case, the filtering criterion has been selected from the the range between 0.007 and 0.009 suggested by the theory. The comparison data in Table 3 are taken from the literature. Cases TNSZ1 and TNSZ2 are the results from the LES using the velocity estimation model by Domaradzki et al. [3]. The case HiDNS is from Gilbert [18] at $Re_\tau = 210$. The DNS results at $Re_\tau = 2003$ for the case HiDNS2 are from the work of Hoyas et al. [19]. The case HiDNS3 are the DNS results at $Re_\tau = 944$ from the work of Del Alamo et al. [20]. The ratio of the total number of mesh points used in TNS and DNS shown in Table 2 demonstrates that TNS resolutions can be of the order of few tenths of 1% of the DNS resolutions. This indicates significant saving in term of computational effort for TNS compared with DNS.

4. Results and discussion

In this section, the results from the simulations for all cases from Table 2 are compared with the baseline data for cases listed in Table 3. The comparisons involve mean and RMS turbulent velocities.

The Re180 case is the classical test case at $Re_\tau \approx 180$ with the domain size $4\pi \times 2\pi \times 2$ for which the detailed DNS data exist [18]. The filtering condition is set to 0.008 resulting in the filter being turned on automatically every 360 to 580 time steps. The case is run for 24,000 times steps and is well converged to a statistically steady state when the data for plotting are taken. In Figure 3(a) we plot the mean velocity, and the RMS velocities are shown in Figures 3(b)–(d). The results for the case Re180 are compared with the high resolution DNS results of Gilbert and Kleiser [18] (case HiDNS), TNS results of Domaradzki et al. [3] (case TNSZ1) and under-resolved DNS performed with the same resolution of $64 \times 64 \times 65$ as for the LES cases Re180 and TNSZ1. The mean velocity in the Re180 case agrees quite well with both HiDNS and TNSZ1 cases. Only in the range of z^+ between 7 and 15, the result from this simulation slightly over predicts results from those two baseline cases. This overshoot of the mean velocity is due to the slight under-prediction

Table 2. LES parameters.

Case	Domain size	Resolution	$\Delta x^+ \times \Delta y^+ \times \Delta z_1^{+c}$	Re_0	Re_τ	$\frac{l(\Delta)}{l(2\Delta)}$	N^a	N_T^b	$(N_{TNS}/N_{DNS})^d$
Re180	$4\pi \times 2\pi \times 2$	$64 \times 64 \times 65$	$35.34 \times 17.67 \times 0.84$	180	182	0.008	24000	$360 - 580$	0.069
Re1050	$2.5\pi \times 0.5\pi \times 2$	$96 \times 128 \times 65$	$85.93 \times 12.88 \times 4.90$	1050	923	0.007	16000	$350 - 620$	0.0056
Re1050h	$2.5\pi \times 0.5\pi \times 2$	$128 \times 128 \times 97$	$64.4 \times 12.88 \times 0.827$	1050	967	0.007	22000	$110 - 180$	0.0112
Re1050h2	$2.5\pi \times 0.5\pi \times 2$	$256 \times 128 \times 97$	$32.21 \times 12.88 \times 0.827$	1050	967	0.007	19000	$80 - 160$	0.0224
Re2000Sh	$2.5\pi \times 0.5\pi \times 2$	$256 \times 128 \times 131$	$61.4 \times 24.5 \times 0.83$	2000	1689	0.008	21000	$80 - 140$	0.0046

Note: [a]The total number of time steps until convergence to statistically steady state.
[b]The observed frequency of the filtering operation (every N_T time steps).
[c]Δz_1^+ is the distance between the first grid point and the boundary.
[d]$N = N_x \times N_y \times N_z$ in TNS and baseline DNS rescaled to the same domain size.

Table 3. Parameters for the reference simulations.

Case	Domain size	Resolution	$\Delta x^+ \times \Delta y^+ \times \Delta z^+$	Re_τ
TNSZ1	$4\pi \times 2\pi \times 2$	$64 \times 64 \times 65$	$35.73 \times 17.88 \times 0.85$	182
TNSZ2	$2.5\pi \times 0.5\pi \times 2$	$96 \times 128 \times 65$	$78.62 \times 11.79 \times 4.49$	961
HiDNS	$3.6\pi \times 1.9\pi \times 2$	$160 \times 160 \times 129$	$14.85 \times 7.83 \times 0.063$	210
HiDNS2	$8\pi \times 3\pi \times 2$	$6144 \times 4608 \times 633$	$8.3 \times 4.1 \times 8.9^a$	2003
HiDNS3	$8\pi \times 3\pi \times 2$	$3072 \times 2304 \times 385$	$7.6 \times 7.6 \times 0.032$	944

Note: [a]For HiDNS2, $\Delta z^+ = \Delta z^+_{max}$; for all other cases Δz^+ is the distance between the first grid point and the boundary.

of the energy dissipation in the buffer region. The imbalance between the kinetic energy production and the dissipation is caused by less frequent filtering compared with the TNSZ1 case. The under-resolved DNS underpredicts the mean velocity in the log region. In Figure 3(b), the streamwise RMS velocity in the simulation is plotted together with all comparison cases as in Figure 3(a). The u_{rms} from simulation compares well with both baseline cases HiDNS and TNSZ1. The same trend continues for the spanwise RMS velocity shown in Figure 3(c), but the vertical RMS velocity is somewhat underpredicted for both Re180 and TNSZ1 cases (Figure 3(d)).

The second test case Re1050 is LES performed in a domain with the size $2.5\pi \times 0.5\pi \times 2$, the resolution of $96 \times 128 \times 65$ mesh points, at $Re_0 = 1050$. The results for this case are plotted in Figure 4 together with the experimental results from Wei and Wilmarth [21], the DNS results from Del Alamo et al. [20], the LES results from Piomelli [22] obtained using the dynamic Smagorinsky model, the LES results from Domaradzki et al. [3] obtained with the velocity estimation model (the case TNSZ2) and the results from DNS without any modeling but at the same low resolution of $96 \times 128 \times 65$ as in two LES cases. The resolution chosen is the same as the one used for the case TNSZ2 in Domaradzki et al. [3] and comparable to the resolution used by Piomelli [22]. The filtering condition is set to 0.007 and the filter is found to be activated every 350 to 620 time steps. The statistically steady state was reached after about 16,000 time steps. All LES mean velocity data, including the case Re1050, are shown in Figure 4(a) and are in good mutual agreement, though they slightly overpredict the experimental data. Figure 4(b) shows the plot of the streamwise RMS velocity from simulation compared with other baseline cases. The agreement with the experimental data and the TNSZ2 data is good between $z = 0$ and $z = 0.2$, but the quality of comparison deteriorates for larger values of z. The vertical RMS velocity LES data shown in Figure 4(c) are in good agreement with the experiments throughout the entire domain. No results for the spanwise velocity are presented here because the experimental data for that velocity were not available for comparisons.

This Reynolds number was also selected to investigate in more detail the dependence of TNS on the mesh resolution. It is well known (e.g. [22]) that the predictions of the mean velocity profile, RMS velocities and high-order statistics depend on the grid resolution, particularly in the wall region. We have performed two additional TNS simulations at $Re_0 = 1050$ with increased resolutions. The case Re1050h is the LES performed in the same domain size as the one used in the case Re1050, but with the grid resolution adjusted according to the discussion in Piomelli [23], Piomelli and Balaras [24] and the recommendations by Sagaut [25]. The main effect of the changed resolution is that the first mesh point away from the wall is at $z^+ < 1$, as required for the wall-resolved LES. The Figures 5(a)–(c) show the plots obtained from the simulation for this case compared with the experimental

and DNS data from the same sources as the reference data used in Figures 4(a)–(c). Thus, the mean velocity profile shown in Figure 5(a) improves. Also, for this resolution, the mean velocity for the under-resolved case is predicted quite well. This case uses only the weak stability filter of Equation (12) at each time step and, based on the prediction of the mean velocity, provides a sufficient substitute for an explicit SGS model. The TNS filter leads to noticeable improvements in the prediction of the RMS velocities over the lower resolution

(a)

(b)
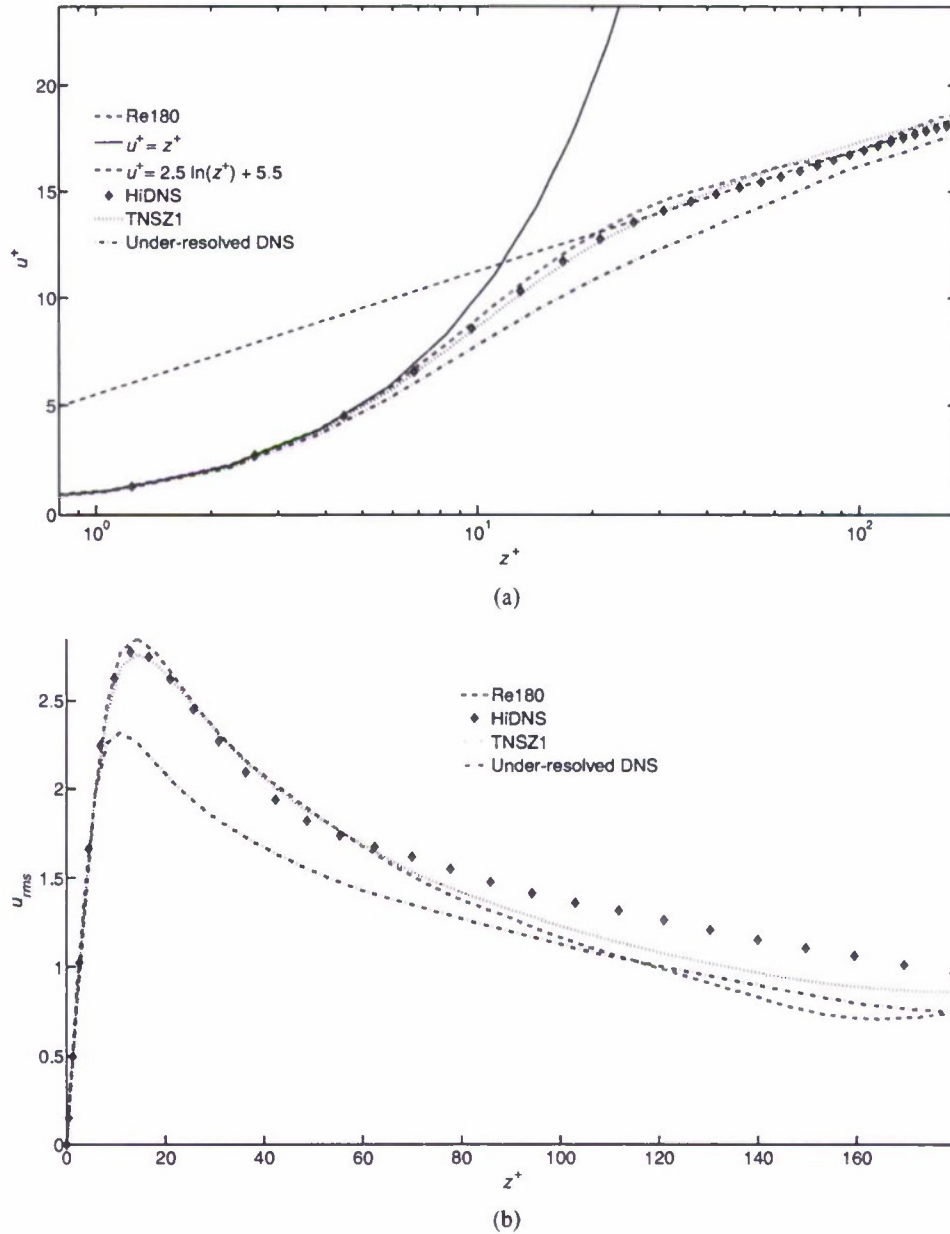
Figure 3.   Results from simulation of the case Re180. Dashed line: Re180; diamond mark: HiDNS; dotted line: TNSZ1; dash-dot line: under-resolved DNS; (a) mean velocity profiles, (b) streamwise RMS turbulent velocity, (c) spanwise RMS turbulent velocity and (d) vertical RMS turbulent velocity.

T. Tantikul and J.A. Domaradzki

(c)

(d)
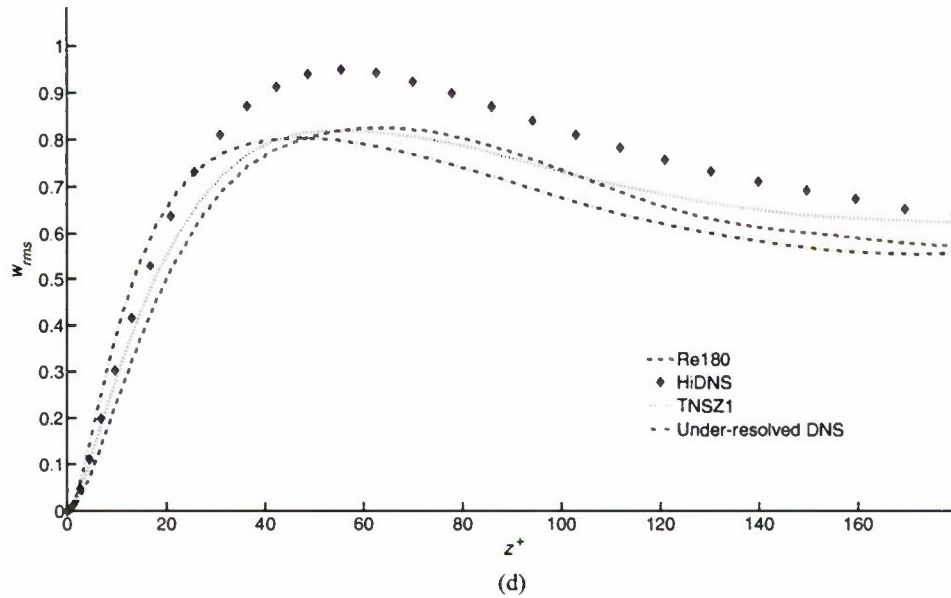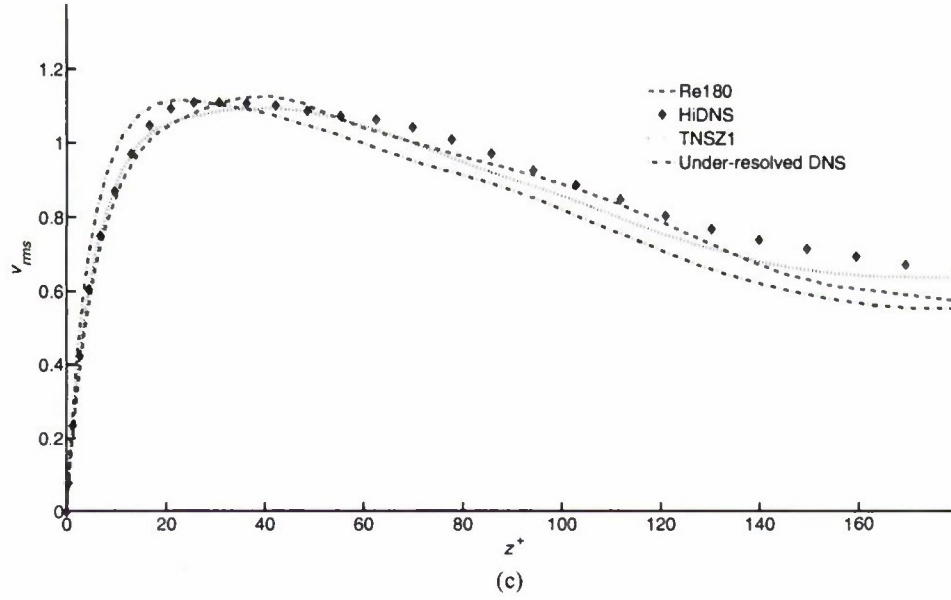
Figure 3.   (Continued)

case Re1050. The results obtained using the TNS filtering are also better than for the under-resolved case, though not much. The effective friction Reynolds number also shows the improvement in capturing the near-wall dynamics by the computational grid. However, there is still the overshoot of the streamwise component of the RMS velocity in near-wall region and the wall normal component of the RMS velocity in near-wall region is slightly under-predicted, indicating that the gird does not fully resolve the structures in the near-wall region which are significant in the turbulent energy production and for the SGS interactions. The case Re1050h2 doubles the mesh resolution in the streamwise direction to satisfy the gener-ally accepted criteria for wall-resolved LES [23–25]. The results are significantly improved

for the TNS case, but no further improvement is observed for the under-resolved case with the stability filter. The mean velocity profile and the RMS velocity plots agree very well with the DNS data as seen in the Figures 6(a)–(c). The small overshoot in the buffer region is still present but the turbulent intensities in the log region are different from the intensities in the cases Re1050 and Re1050h. There is no overshoot in near-wall region for RMS streamwise component of the velocity and the RMS wall-normal component of the velocity agrees very well with the DNS data. These results indicate that the grid resolution in the Re1050h2

Figure 4. Results from simulation of the case Re1050. Dashed line: Re1050; triangle mark: Wei & Wilmart; dash-dot line with plus mark: Piomelli; dotted line: TNSZ2; dash-dot line: under-resolved DNS; diamond mark: HiDNS3; (a) mean velocity profiles, (b) streamwise RMS turbulent velocity and (c) vertical RMS turbulent velocity.
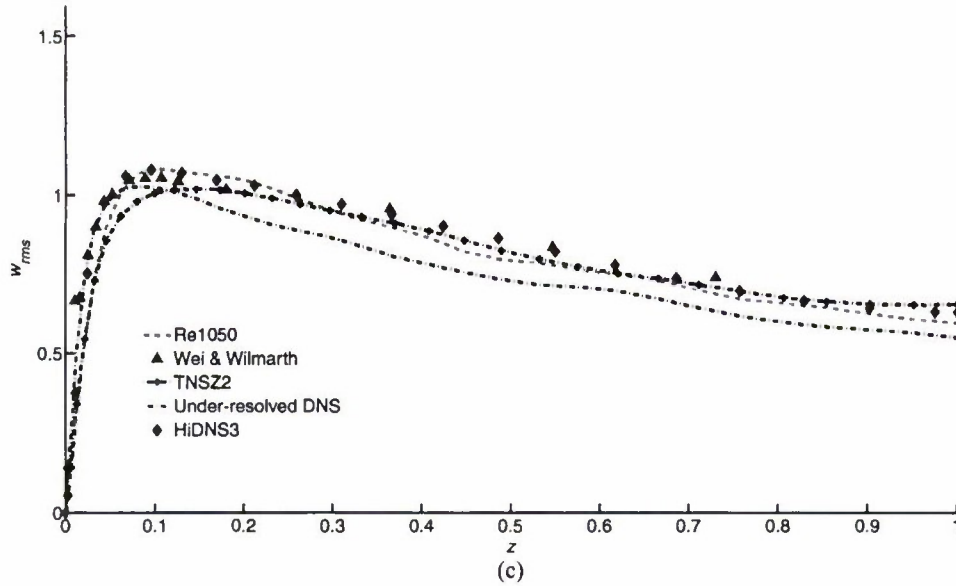
Figure 4.   (Continued)

case in conjunction with the TNS procedure is able to resolve the near-wall dynamics. However, though the application of only stability filter allows to capture the mean flow, the prediction of the rms velocities for this case does not have the same quality as the full TNS method.

Figures 7(a)–(d) show plots obtained in LES at $Re_0 = 2000$ in the domain size $2.5\pi \times 0.5\pi \times 2$, and the resolution $256 \times 128 \times 131$. The filtering criterion is set to 0.008 and the filter turns on automatically every 80 to 160 time steps. This is more frequent filtering than in previous cases, indicating that the simulations at high Reynolds number require more dissipation. The statistically steady state is reached after about $21,000$ time steps. The comparisons are made with the under-resolved DNS and the HiDNS2 case, which is the fully resolved DNS of Hoyas and Jimenez [19], but in the larger domain $8\pi \times 3\pi \times 2$. The resolution used in the Re2000Sh case is selected based on the observations from the cases Re1050h and Re1050h2 and also from the computational expense considerations. The mean velocity shown in Figure 7(a) slightly overpredicts the DNS results in the similar way as in the lower Reynolds number case Re1050h (Figure 5(a)). The quality of the prediction for the streamwise RMS velocity presented in Figure 7(b) is lower. LES overpredicts the peak of the u_{rms} from the HiDNS2 case and underpredicts the DNS results in the range $z^+ > 200$. The remaining two RMS turbulent velocity components are shown in Figures 7(c) and exhibit good agreement with the DNS data at $z^+ < 800$. The overprediction and the underprediction of the peak of u_{rms} could come from the insufficient grid resolutions in the near-wall region. Nevertheless, at this high Reynolds number, for the computational expense the quality of the low-order statistics is quite satisfactory.
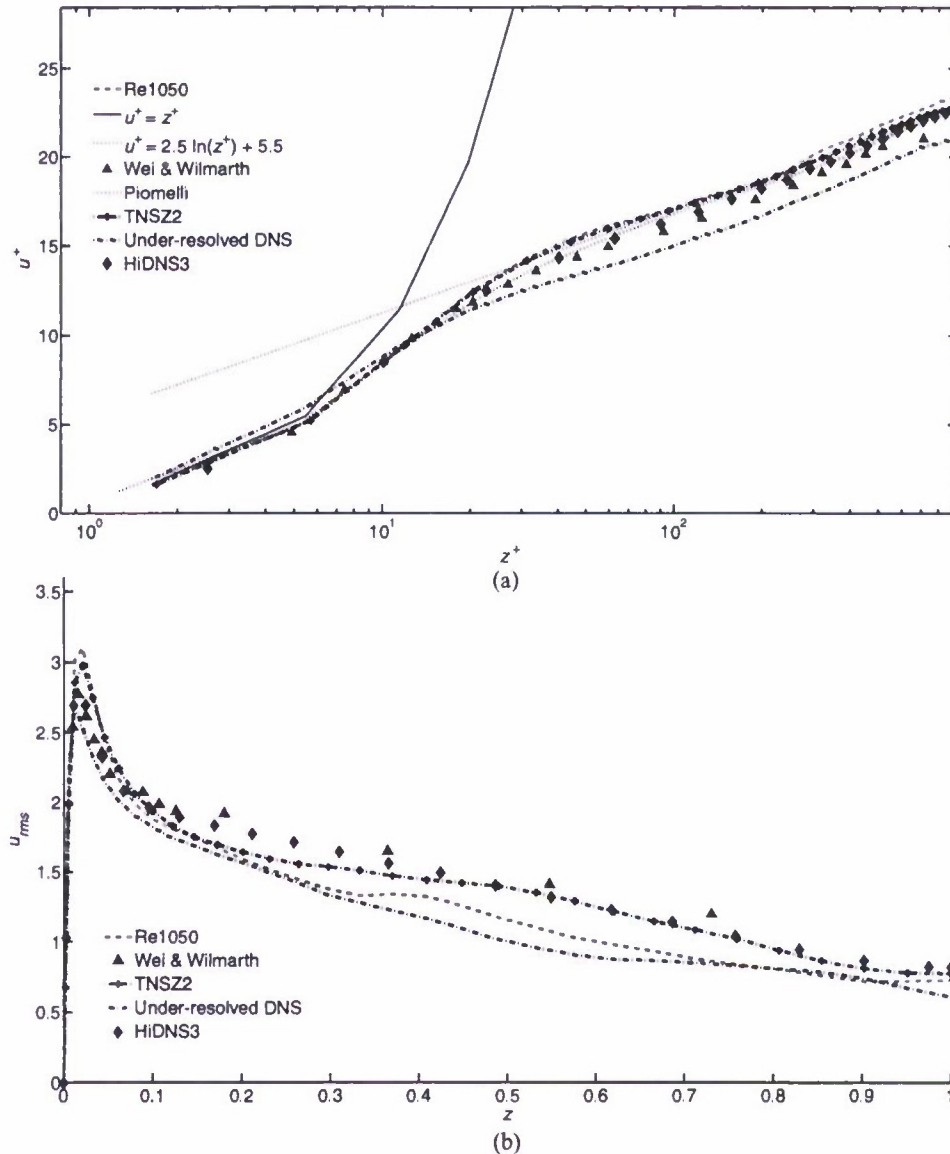
(a)

(b)
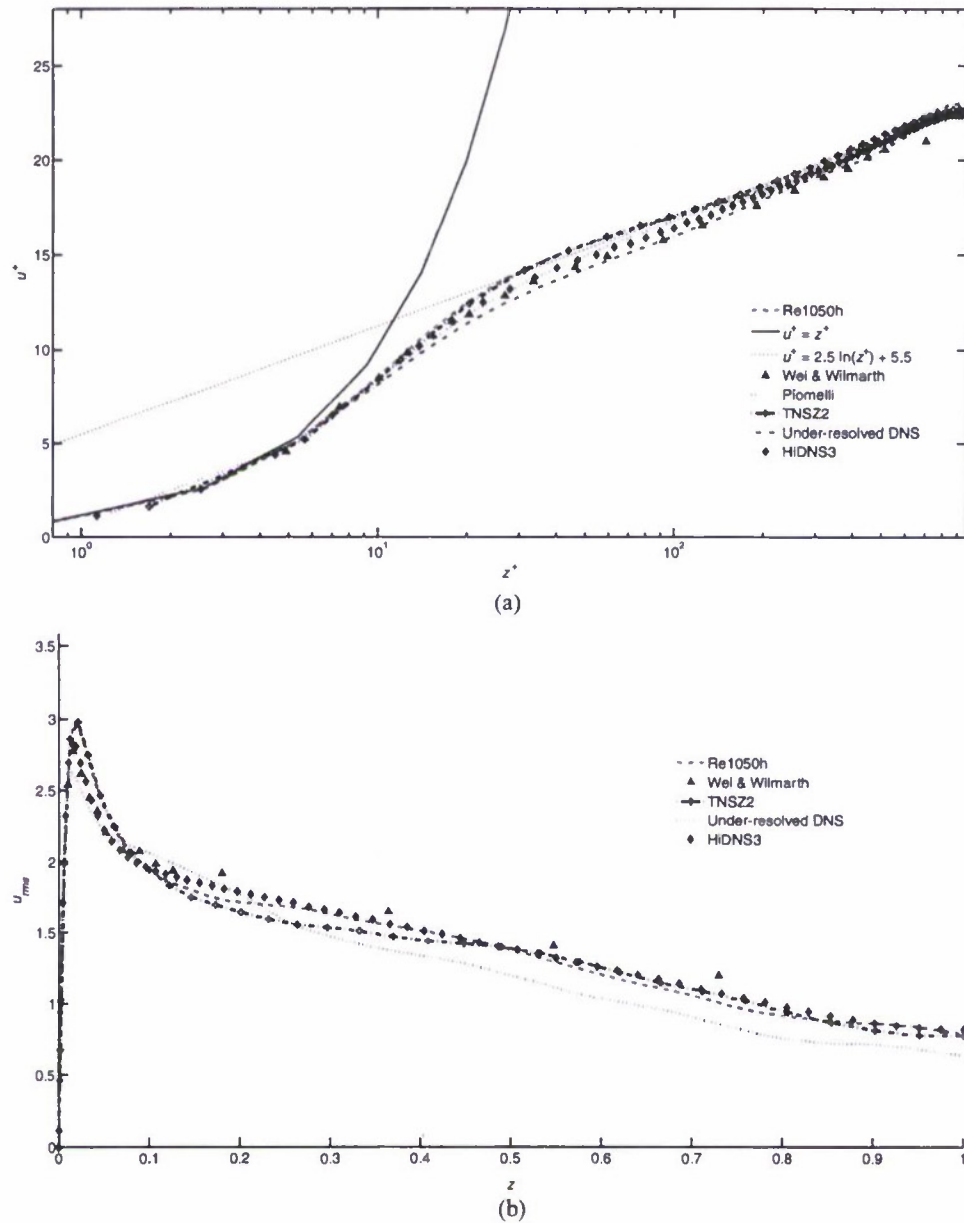
Figure 5. Results from simulation of the case Re1050h. Dashed line: Re1050h; triangle mark: Wei & Wilmart; dash-dot line with plus mark: Piomelli; dotted line: TNSZ2; dash-dot line: under-resolved DNS; diamond mark: HiDNS3; (a) mean velocity profiles, (b) streamwise RMS turbulent velocity and (c) vertical RMS turbulent velocity.
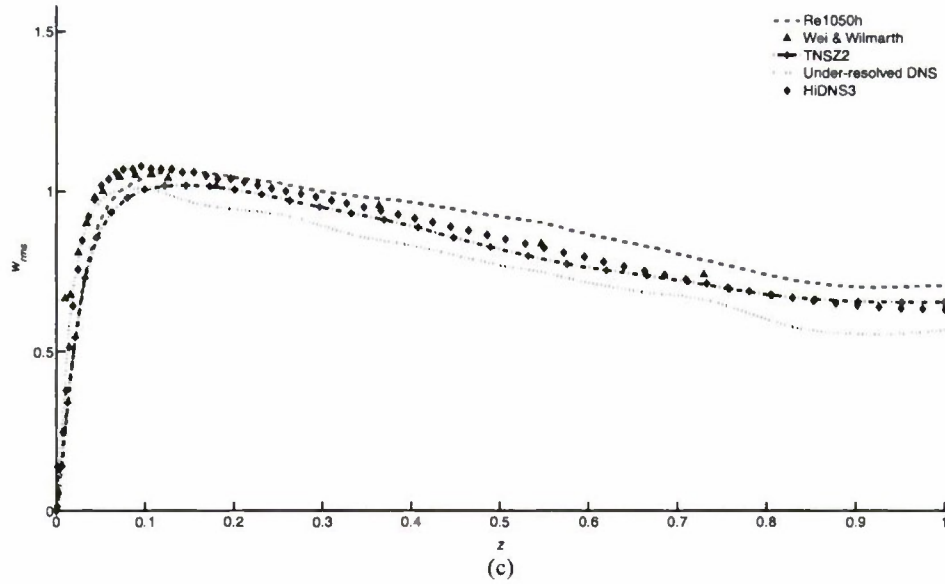
Figure 5.   (Continued)
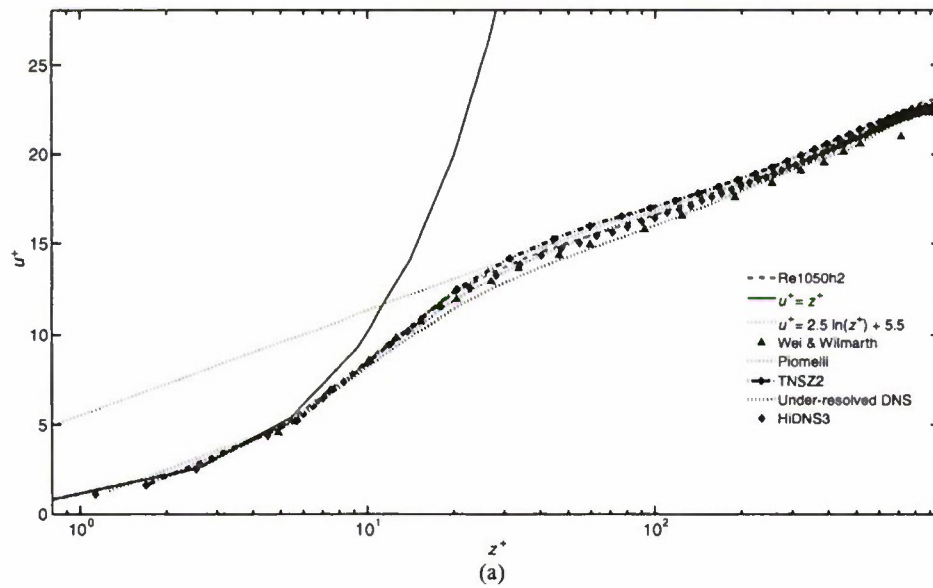
Figure 6.   Results from simulation of the case Re1050h2. Dashed line: Re1050h2; triangle mark: Wei & Wilmart; dash-dot line with plus mark: Piomelli; dotted line: TNSZ2; dash-dot line: under-resolved DNS; diamond mark: HiDNS3; (a) mean velocity profiles, (b) streamwise RMS turbulent velocity and (c) vertical RMS turbulent velocity.

Figure 6.   (Continued)

(a)

(b)

Figure 7.   Results from simulation of the case Re2000Sh. Dashed line: Re2000Sh; diamond mark: HiDNS2; dash-dot line: Under resolved DNS (a) Mean velocity profiles, (b) Streamwise rms turbulent velocity, (c) Spanwise rms turbulent velocity, and (d) Vertical rms turbulent velocity.

Figure 7. (Continued)

5. Conclusions

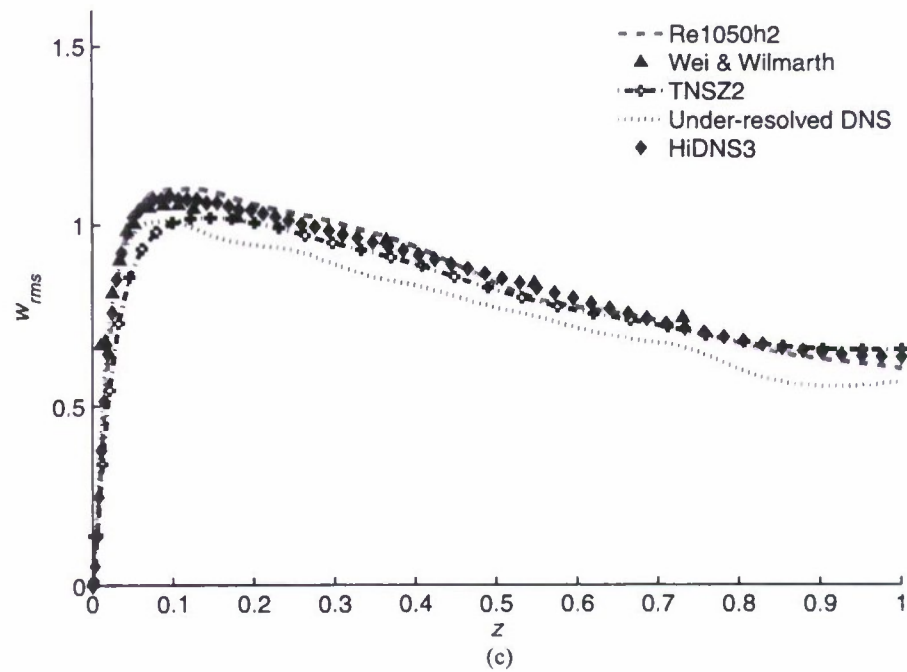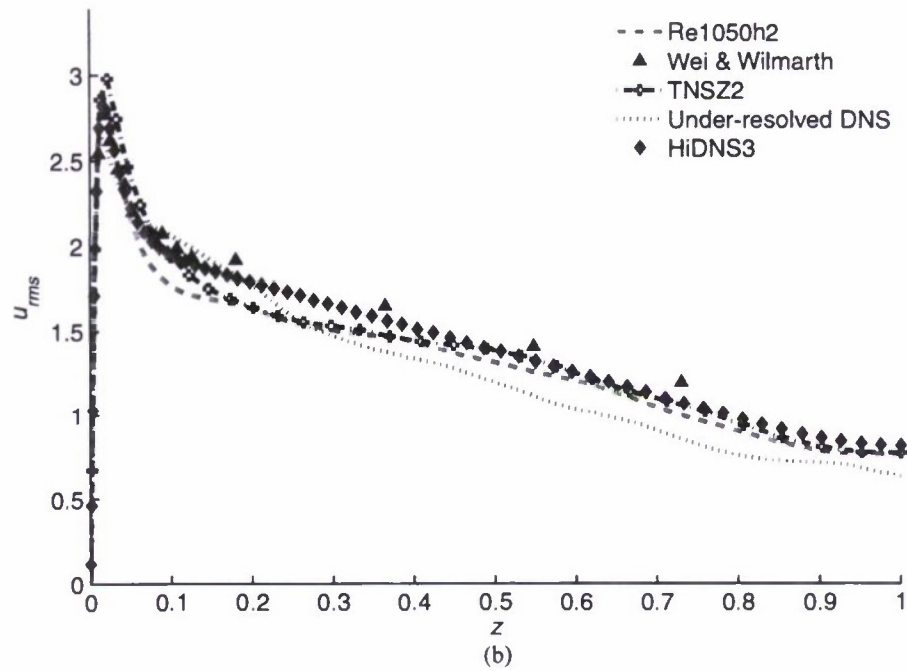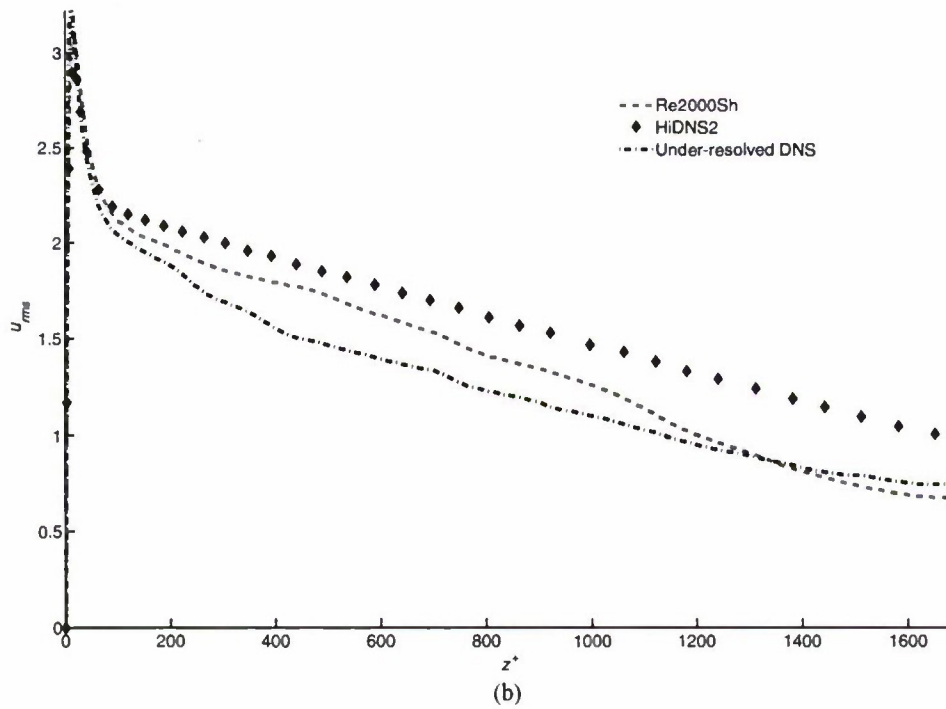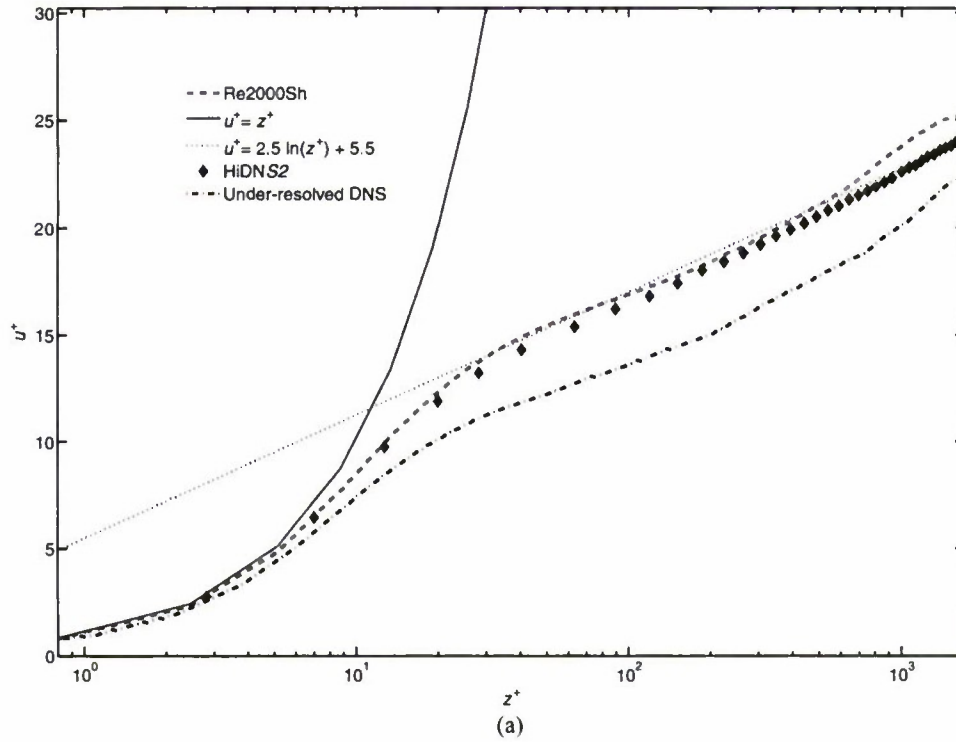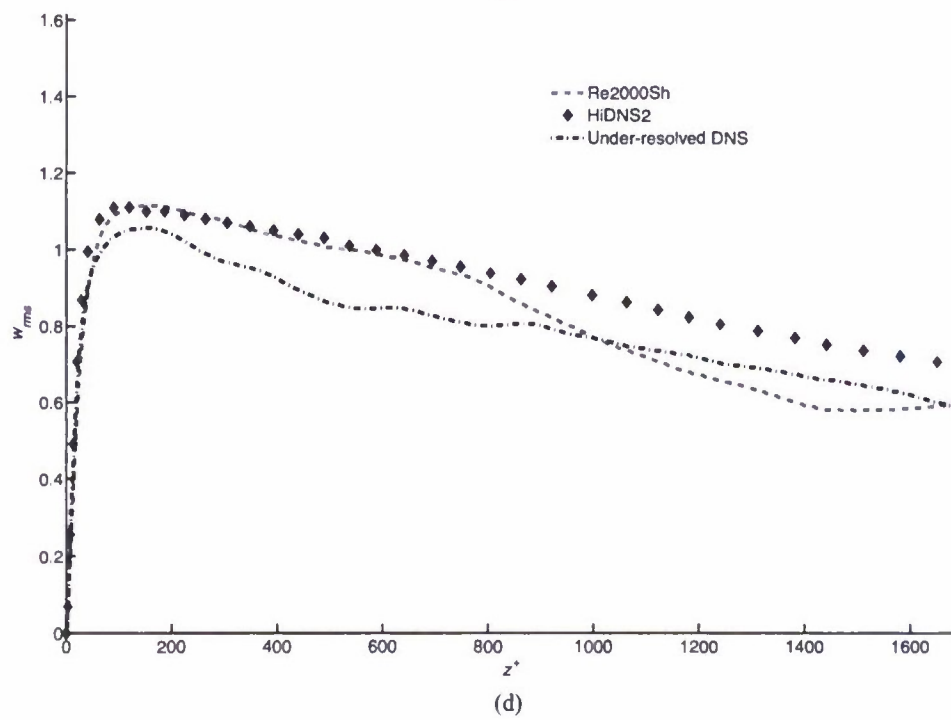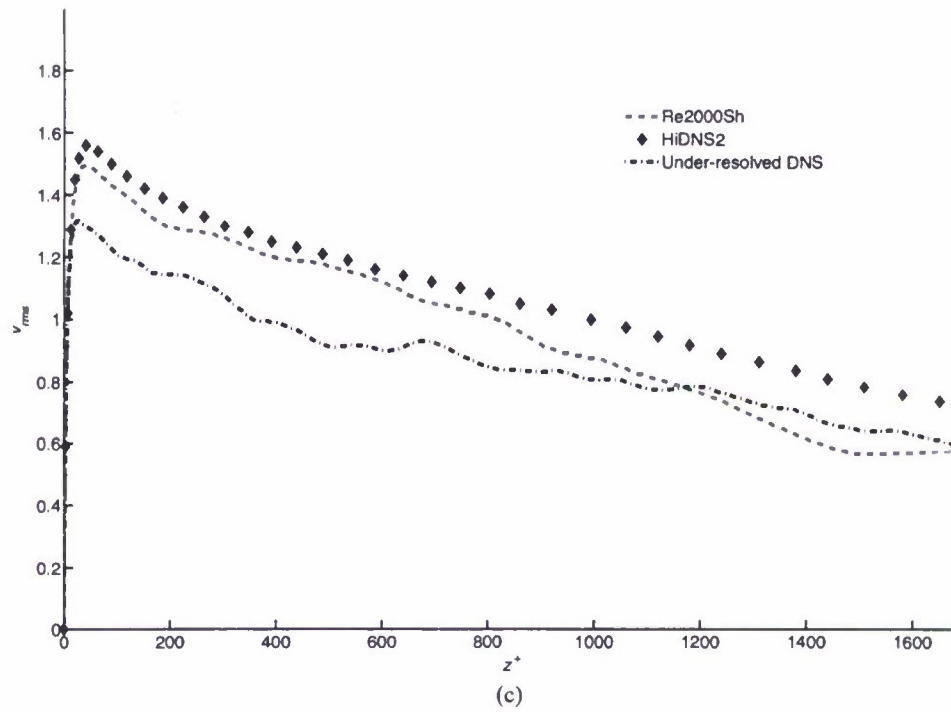The numerical code employed in this work uses spectral methods stabilized by a weak filter which allows it to run for all Reynolds numbers and resolutions considered. Despite the simulations being stable, the results from such runs do not compare well with the baseline DNS and the experimental data, as expected from under-resolved DNS, unless very high resolution is employed. It is thus clear that, beyond numerical stabilization techniques, additional turbulence modeling procedures are required to obtain physically correct results in simulations that do not resolve all relevant scales of motion. We have presented the LES model that utilizes the low-pass filtering operation as the only modeling tool. The entire procedure follows closely the previously developed TNS approach which uses the filter periodically to modify smallest resolved scales. In the present TNS implementation, the energy of these scales is monitored and the filter is turned on automatically whenever the energy exceeds a threshold defined by a specific criterion. We have tested the model on the turbulent channel flow problem at different Reynolds numbers, computational resolutions and domain sizes. Satisfactory comparisons among TNS results and various reference cases have been obtained. In particular, the quality of the results is comparable to the previous TNS procedure which uses a fixed time interval for the filtering as well as additional SGS-estimated velocity.

The main goal of LES is to predict accurately low-order statistics using the lowest possible numerical resolution. Because of that the grid resolutions used in the reported work were selected to test and study the dependency of the quality of low-order statistics' predictions on the grid resolutions, using guidelines from previous work regarding the wall-resolved LES of the channel flow. The cases Re1050 and Re2000Sh were selected to test the proposed TNS method with coarse resolution. The overpredicted wall shear stress and the overshoot in the near-wall region in u_{rms} show that the grid resolutions are not sufficient to resolve the structures near the wall. The TNS filtering that provides SGS dissipation tends to overdissipate energy in the log region as seen in the results for u_{rms} and w_{rms} for these cases. When resolution is increased, the quality of the results improves significantly. This is clearly seen in the plots of u_{rms} for the cases Re1050, Re1050h and R1050h2, where the overshoot in the near-wall region decreases when the grid resolution increases. The mean velocity profiles for these test cases also improve and this improvement makes the shear stress predictions more accurate. The case Re2000Sh was conducted to test the performance of our approach at high Reynolds number as the simulations would expect to depend more on the filtering to provide energy dissipation. Even though the simulations in these cases are done at high Reynolds number and the employed grid resolutions are marginal, the predictions of the mean velocity profiles are reasonable. The improvement in the quality of the predictions using this approach at high Reynolds numbers should be expected as the grid resolution is increased further.

In summary, we have shown that the TNS method is capable to produce quality LES results despite a lack of an explicit SGS model. In TNS, the smallest scales resolved by the mesh provide a model of SGS. They are modified periodically by the explicit filtering operation, which is triggered by a condition based on the analysis of the energy spectra in developed turbulence. We believe that the simplicity and the flexibility are the features of the method that should be appreciated. Like with any modeling procedure, there is always room for improvement. For instance, it is rather obvious that the filtering criterion will depend on the filter's form. However, one may conjecture that TNS results should be independent of the filter's form as long as the filter's effect is to substantially attenuate small scales while leaving the large scales unchanged and if the filtering criterion is derived for the specific filter used. We will investigate the dependence of the model on the filter form in the subsequent work.

Acknowledgements

References

[1] J.A. Domaradzki and N.A. Adams, *Direct modeling of subgrid scales of turbulence in large eddy simulations*, J Turbulence 3:1 (2002), p. 1.

[2] J.A. Domaradzki and E.M. Saiki, *A subgrid-scale model based on the estimation of unresolved scales of turbulence*, Phys. Fluids 9 (1997), p. 2148.

[3] J.A. Domaradzki, K.C. Loh, and P.P. Yee, *Large eddy simulation using the subgrid-scale estimation model and truncated Navier–Stokes dynamics*, Theor. Comput. Fluid Dyn. 15 (2002), p. 421.

[4] S. Stolz, N.A. Adams, and L. Kleiser, *An approximate deconvolution model for large eddy simualtion with application to incompressible wall-bounded flows*, Phys. Fluids 13 (2001), p. 997.

[5] B. Kosovic, D.I. Pullin, and R. Samtaney, *Subgrid-scale modeling for large eddy simulations of compressible turbulence*, Phys. Fluids 14 (2002), p. 1511.

[6] F.F. Grinstein, L.G. Margolin, and W.J. Rider *Implicit Large Eddy Simulation*, Cambridge University Press, Cambridge, UK, 2007.

[7] J.A. Domaradzki and K.C. Loh, *The subgrid-scale estimation model in the physical space representation*, Phys. Fluids 11 (1999), p. 2330.

[8] M.R. Visbal and D.P. Rizzetta, *Large-Eddy Simulation on General Geometries Using Compact Differencing and Filtering Schemes*, AIAA 2002-0288 (2002).

[9] M.R. Visbal and D.P. Rizzetta, *Large-eddy simulation on curvilinear grids using compact differencing and filtering schemes*, J. Fluids Eng. 124 (2002), pp. 836–847.

[10] C. Bogey and C. Bailly, *Large eddy simulations of transitional round jets: Influence of the Reynolds number on flow development and energy dissipation*, Phys. Fluids 18 (2006), p. 065101.

[11] P.J. Diamessis, J.A. Domaradzki, and J.S. Hesthaven, *A spectral multidomain penalty method model for the simulation of high Reynolds number localized incompressible stratified turbulence*, J. Comp. Phys. 202 (2005), p. 298.

[12] M. Minguez, R. Pasquetti, and E. Serre, *Spectral vanishing viscosity stabilized LES of the Ahmed body turbulent wake*, Comm. Comput. Phys. 5 (2009), pp. 635–648.

[13] P.J. Diamessis, Y.C. Lin, and J.A. Domaradzki, *Effective numerical viscosity in spectral multidomain penalty method-based simulations of localized turbulence*, J. Comp. Phys. 227 (2008), pp. 8145–8164.

[14] P.P. Yee, Ph.D. diss., University of Southern California, CA, 2000.

[15] H. Jeanmart, and G.S. Winckelmans, *Investigation of eddy-viscosity models modified using discrete filters: A simplified regularized variational multiscale model and on enhanced field model*, Phys. Fluids 19 (2007).

[16] S. Gottlieb and J.S. Hesthaven, *Spectral methods for hyperbolic problems*, J. Comput. Appl. Math 128 (2001), p. 83.

[17] R. Kerr, *Velocity, scalar and transfer spectra in numerical turbulence*, J. Fluid Mech. 211 (1990), p. 309.

[18] N. Gilbert and L. Kleiser, *Turbulence model testing with the aid of direct numerical simulation results*, in *Proceedings of 8th Symposium on turbulence shear flows*, Munich, Germany, 1991.

[19] S. Hoyas and J. Jimenez, *Scaling of the velocity fluctuations in turbulence channels up to* $Re_\tau = 2003$, Phys. Fluids 18 (2006), p. 2.

[20] J.C. Del Alamo, J. Jimenez, P. Zandonade, and R.D. Moser, *Scaling of the energy spectra of turbulent channels*, J. Fluid Mech. 500 (2004), p. 135.

[21] T. Wei and W.W. Wilmarth, *Reynolds number effects on the structure of turbulent channel flow*, J. Fluid Mech. 204 (1989), p. 57.

[22] U. Piomelli, *High Reynolds number calculation using the dynamics subgrid scale model*, Phys. Fluids A5 (1993), p. 1484.

[23] U. Piomelli *Wall-layer models for large-eddy simulations*, Prog. Aerosp. Sci. 44 (2008), p. 2.

[24] U. Piomelli and E. Balaras, *Wall-layer models for large-eddy simulations*, Annu. Rev. Fluid Mech. 34 (2002), p. 349.

[25] P. Sagaut, *Subgrid-Scale Modeling: Issues and Approaches, in Implicit Large Eddy Simulations: Computing Turbulent Fluid Dynamics*, Cambridge University Press, Cambridge, UK, 2007.

REVIEW ARTICLE

Large Eddy Simulations without Explicit Eddy Viscosity Models

J. A. Domaradzki[a]*

[a]Department of Aerospace and Mechanical Engineering,
University of Southern California,
Los Angeles, CA 90089-1191, U.S.A.

The classical approach to performing large eddy simulations of turbulent flows is to employ in the governing equations subgrid scale models based on eddy viscosity concepts. The development of the similarity model about thirty years ago led to the realization that subgrid scale models that do not use eddy viscosity concepts are possible and have many desirable properties. In this paper we review modeling approaches belonging to this category and discuss their advantages and the limitations.

Keywords: Large Eddy Simulations, Eddy Viscosity Models

---

* Email: jad@usc.edu

2

1.   Introduction

The equations for large eddy simulation (LES) are traditionally obtained by the filtering approach proposed by Leonard (1974) where a spatial filter that strongly attenuates scales of motion smaller than the prescribed filter width Δ is applied to the Navier–Stokes equations. If the filtered quantities are denoted by an overbar, the LES equations for an incompressible flow become

$$\frac{\partial}{\partial t}\overline{u}_i + \frac{\partial}{\partial x_j}\overline{u}_i\,\overline{u}_j = -\frac{1}{\rho}\frac{\partial}{\partial x_i}\overline{p} + \nu\frac{\partial^2}{\partial x_j\partial x_j}\overline{u}_i - \frac{\partial}{\partial x_j}\tau_{ij}, \tag{1}$$

$$\frac{\partial}{\partial x_i}\overline{u}_i = 0 \ , \tag{2}$$

where $u_i = (u_1, u_2, u_3) = (u, v, w)$, p, and ν are the velocity, pressure, and the kinematic viscosity, respectively, and τ_{ij} is the subgrid-scale (SGS) stress tensor

$$\tau_{ij} = \overline{u_i u_j} - \overline{u}_i\,\overline{u}_j. \tag{3}$$

The form of equations (1) and (2) requires that the filtering and differentiation commute (Ghosal and Moin (1995), Vasilyev *et al.* (1998)). In practice, however, the above equations are frequently the starting point in SGS modeling without regard to formal requirements for their derivation in the filtering framework. The important point is that the LES equations have the form of the Navier-Stokes equations for the filtered velocity $\overline{u}_i$ plus the additional force term which is the divergence of the subgrid scale stress tensor (3), and which is required to close the LES equations. Various SGS models differ in how the SGS stress tensor is expressed (or modeled) in terms of the filtered velocity $\overline{u}_i$.

Among SGS models the most important category are the eddy viscosity models. Their origin goes back to Boussinesq (1877) who proposed that the effects of turbulence can be accounted for by the viscosity increased over its value in laminar flows. With the advent of computers and attempts to perform general circulation simulations, the eddy viscosity concept was used by Smagorinsky (1963) to model "The lateral transfer of momentum and heat by the non-linear diffusion, which parametrically is supposed to simulate the action of motions of sub-grid scale,...", thus starting the modern era of LES and SGS modeling. There are a number of excellent reviews of theory and practice of SGS modeling in the eddy viscosity framework, e.g., by Galperin and Orszag (1993), Lesieur and Métais (1996), Piomelli (1999), Meneveau and Katz (2000), Pope (2000), and Sagaut (2002), and such methods are not addressed in this review.

Despite its practical utility the eddy viscosity concept has not been accepted as a fully satisfactory solution of the turbulence modeling problem because it is not consistent with some observed features of turbulence physics. For instance, a purely dissipative character of the eddy viscosity does not allow such models to describe an inverse energy transfer (backscatter) observed in actual turbulent flows. The dynamic Smagorinsky model of Germano *et al.* (1991) formally allows for the backscatter but this may lead to unstable simulations. In practice various averaging procedures for the dynamic Smagorinsky coefficient are used to render the eddy viscosity a positive quantity. Nevertheless the dynamic procedure offers a significant improvement over the eddy viscosity models with constant coefficients. This is because the modeled SGS transfer is consistent with the actual en-

ergy transfer across the test cutoff, allowing the model to better represent energy drain from the resolved scales for a wider variety of turbulent flows. Yet this desirable feature may turn into disadvantage in some situations. One such situation is turbulence with rotation. Traditional eddy viscosity models encounter a number of difficulties when applied to rotating flows (Speziale (1989), Squires and Piomelli (1995)) because the energy transfer from the large scales to the small ones is reduced, and consequently the energy dissipation decreases with rotation rate (e.g., Morinishi *et al.* (2001), Yeung and Zhou (1998), Jacquin *et al.* (1990)), requiring lower values of the Smagorinsky constant than for non-rotating flows. The dynamic procedure accounts for this effect but it also makes the Smagorinsky coefficient a spatially variable quantity. As shown by Horiuti (2001) and Kobayashi and Shimomura (2001) because of the latter feature the model violates transformation properties between inertial and rotating frame of reference. Rather than using such specific arguments sometimes more general arguments are invoked against eddy viscosity models. For instance, one may note that LES attempts to simulate scales which, by virtue of being far removed from the dissipation range, are essentially inviscid; simulating them as dissipative scales through the use of an eddy viscosity appears as the contradiction. Listing such few limitations and contradictions is not meant to disqualify the eddy viscosity models. Indeed, the experience accumulated over many decades in this field is that the single most important requirement in turbulence modeling is that a model is globally dissipative, and the eddy viscosity concept guarantees this by design. However, the recognition of the above listed difficulties serves to motivate research on other approaches to the SGS modeling that seek improvements in the fidelity of LES predictions without constraints imposed by the eddy viscosity concept. The main subject of this paper is a review of a collection of approaches to the problem of SGS modeling, which do not use explicit eddy viscosity expressions. While no single approach has emerged to displace the current eddy viscosity models, the continuing progress in this area offers hope that such approaches may eventually become successful in simplifying the task of LES and in improving its predictive capabilities.

2.   Similarity Models

In well resolved direct numerical simulations full velocity fields are available. For a prescribed filter the filtered velocity can be computed numerically from the filter definition, often represented as a convolution integral with a given smoothing kernel G,

$$\overline{u}_i(\mathbf{x}) = \int G(\mathbf{x} - \mathbf{x}'; \Delta) u_i(\mathbf{x}') d\mathbf{x}'. \tag{4}$$

Similarly, for a given u_i the exact SGS stress tensor can be computed from its definition (3). Independently, the modeled SGS tensor can be found using the known $\overline{u}_i$ and parameters of the model and both stresses can be compared, constituting the so-called *a priori* comparison. It was realized early by Clark *et al.* (1979), and later confirmed in independent investigations (Piomelli *et al.* 1988, Domaradzki *et al.* 1993, Liu *et al.* 1994), that the eddy viscosity SGS stress expressions correlate poorly with the actual stresses. This conclusion provided an original impetus for the search for the models that would improve the quality of *a priori* comparisons. The first model that offered a considerable improvement in this area has been proposed by Bardina *et al.* (1983) and is known as the similarity model. While the original reasoning leading to the model was more complicated, the final result can be viewed as the result of approximating the full, unknown

4

in LES velocity u_i, by the filtered velocity $\overline{u}_i$ which is known in LES

$$u_i \approx \overline{u}_i, \tag{5}$$

and using it in the definition (3), i.e.,

$$\tau_{ij} = \overline{u_i u_j} - \overline{u}_i \, \overline{u}_j \approx \overline{\overline{u}_i \overline{u}_j} - \overline{\overline{u}}_i \, \overline{\overline{u}}_j \ . \tag{6}$$

The similarity model proposed by Liu *et al.* (1994) and O'Neil and Meneveau (1997) also uses the known, resolved velocity $\overline{u}_i$ as an approximation to the full velocity but the modeled SGS stress tensor (3) is assumed to be proportional to the resolved stress tensor L_{ij} computed using a different filter, denoted here by a hat

$$\tau_{ij} \approx c_L L_{ij} = c_L \left(\widehat{\overline{u}_i \, \overline{u}_j} - \widehat{\overline{u}}_i \, \widehat{\overline{u}}_j \right). \tag{7}$$

The hat filter is wider than the overbar filter, therefore the expression for L_{ij} reflects qualitatively the property of the exact SGS stress (3) where the underlying velocity u_i contains smaller scales than those that are retained by the application of the filter. Both expressions, (6) and (7), show much improved correlations in numerical and experimental *a priori* tests.

However, the practical experience is that when such models are implemented in actual LES the simulation results quickly deteriorate, with the main culprit identified as an insufficient SGS dissipation (Liu *et al.* 1994). Because of that a number of so-called mixed models have been proposed that simply combine similarity models (to guarantee a good performance in *a priori* tests) and eddy viscosity models (to provide a good performance in *a posteriori* tests, i.e., in actual LES). The solution proposed by the mixed models is not entirely satisfactory. It is obvious that it is the presence of the eddy viscosity expressions that makes the mixed models work in actual LES. Since comparable LES results can be obtained with only eddy viscosity models it is not clear that the similarity component plays any useful role in LES performed with the mixed models. The stronger statement is that the need for adding the eddy viscosity expression to a similarity expression signifies the failure of the similarity concept as a SGS modeling approach. The current LES practice implicitly endorses this view through a diminishing emphasis on similarity models and *a priori* tests. Nevertheless, the understanding of the failure of the similarity modeling is useful in developing non-eddy viscosity models, to avoid similar mistakes on the one hand, and on the other to decide if the similarity concept is fundamentally flawed or if only its specific implementations are at fault.

The reasons for the failure of the similarity models can be qualitatively understood if the general formula (7) is considered for sharp spectral filters with two wavenumber cutoffs $\overline{k} > \hat{k}$, where $\overline{k}$ is also the numerical mesh cutoff. This way all active LES modes are split into two bands: band 1 for $0 < k \leq \hat{k}$ and band 2 for $\hat{k} < k \leq \overline{k}$. The physical effect of the expression $\left(\widehat{\overline{u}_i \, \overline{u}_j} - \widehat{\overline{u}}_i \, \widehat{\overline{u}}_j \right)$ has been elucidated in investigations dealing with the energy transfer in turbulent flows (Domaradzki *et al.* 1993, Kerr and Domaradzki 1996). The first term in the difference describes the effect of nonlinear interactions among all resolved LES modes (band 1 and 2) on modes in the band 1 (the widehat filter). The second term describes the effect of nonlinear interactions among modes from the band 1

on modes in band 1 and 2. Sometimes it is convenient to use the notation T^{pqm} to indicate the energy transfer to band m caused by the nonlinear interactions between bands p and q (Domaradzki and Rogallo 1990, Domaradzki *et al.* 1994). With this notation the effect of the similarity expression on the energetics of the flow is represented symbolically as

$$\left(T^{111} + T^{121} + T^{221}\right) - \left(T^{111} + T^{112}\right). \tag{8}$$

In the above expression the effects of energy redistribution within band 1 (term T^{111}) cancel. The remaining terms describe the energy transfer from the band 1 due to interactions between band 1 and 2 (T^{121}) and interactions of modes in band 2 (T^{221}); they result in the energy loss by the band 1. The last term T^{112} is normally the energy gain in band 2 due to interactions among modes in band 1; but because of the negative sign it is an effective loss term for the band 2. The interscale energy transfer caused by the complete nonlinear term in LES equations, $-\partial/\partial x_j(\overline{u}_i\,\overline{u}_j)$, accounts for all combinations of interacting bands and can be represented as follows

$$\left(T^{111} + T^{121} + T^{221}\right) + \left(T^{112} + T^{122} + T^{222}\right). \tag{9}$$

Based on observed magnitudes and signs of all terms in that expression (Domaradzki *et al.* 1994) it has an interpretation consistent with the classical picture of the turbulent energy cascade: the energy is removed from band 1 (terms T^{121} and T^{221}) and deposited into band 2 (terms T^{112} and T^{122}) while T^{111} and T^{222} have redistributive character. The principal role of a SGS model is to counteract the accumulation of the energy in the band 2 caused by this energy transfer process, i.e., to counteract the effect of terms T^{112} and T^{122}. However, the similarity expression (8) counteracts only one of the two active terms, T^{112}, and also removes the energy from band 1 through the action of T^{121} and T^{221}, essentially doubling the energy transfer from band 1 caused by the nonlinear term in LES equations. The result is that the model is deficient in removing the energy from the vicinity of the LES cutoff and unnecessarily increases the energy loss by the large scales in band 1 beyond what is already provided by the resolved nonlinear interactions. The quantitative analysis can be more complicated for different similarity expressions and because of the presence of the viscous and non-stationarity effects. Nevertheless, the above energy transfer analysis provides the qualitative explanation of the failure of the similarity concept in SGS modeling. Such a qualitative understanding may offer suggestions for improvements in this category of SGS models.

3. Deconvolution and Nonlinear Models

The deconvolution models are based on the observation that, under certain conditions, the filtering operation can be inverted, thus providing the unfiltered quantity u_i from the filtered one $\overline{u}_i$. The convolution operation (4) in the Fourier space is

$$\overline{u}_i(k) = G(k)u_i(k), \tag{10}$$

where for simplicity we assume a 1-D filter and the Fourier transform is indicated by the dependence on the wavenumber k. The inverse operation can be formally defined as

$$u_i(k) = \overline{u}_i(k)/G(k), \tag{11}$$

and is possible if the division can be performed and the result is an integrable function.

In the context of SGS modeling the inversion of filtering has been proposed first by Leonard (1974) and later by Germano (1986), though not in the form described above. Leonard (1974) showed that the SGS stress tensor can be reconstructed as an infinite series in the filtered velocity and its derivatives, with the lowest order term in the form known as the nonlinear model

$$\tau_{ij} \sim \frac{\partial \overline{u}_i}{\partial x_k} \frac{\partial \overline{u}_j}{\partial x_k}. \tag{12}$$

Germano (1986) introduced an exponential filter which has an inverse in a form of a differential operator. The inverse allows to compute the SGS stress tensor from the definition (3) and is also consistent with the nonlinear model in the first approximation. The expression (12) was first investigated as a SGS model by Clark *et al.* (1979) and subsequently also, among others, by Liu *et al.* (1994), Borue and Orszag (1998), Leonard (1997), Winckelmans *et al.* (2001), and Iliescu *et al.* (2003). In particular, Iliescu *et al.* (2003) clarified that the form of the model is a direct consequence of approximating the Fourier transform of a Gaussian filter by its Taylor polynomial expansion in filter width Δ and keeping terms up to the order Δ^2 in the expression for the SGS stress.

The modern approach to deconvolution methods in SGS modeling, including the 'de-convolution' terminology, has been introduced by Stolz and Adams (1999) (detailed review of that work is also provided by Domaradzki and Adams (2002)). These authors recognized that the conditions for the exact inverse of filtering operations are generally not satisfied, but it is possible to use an approximate or regularized deconvolution. Specifically, Stolz and Adams (1999), and Stolz *et al.* (2001a) employ a power series expansion of van Cittert (1931), which assumes that the inverse filtering operator, if it existed, could be written as $G^{-1} = \sum_{n=0}^{\infty} (I - G)^n$, where I is the identity operator. Regularized inversion is obtained if this series is truncated at a certain N which becomes the regularization parameter, giving an approximate inversion as

$$u_i \approx Q_N * \overline{u}_i \equiv \sum_{n=0}^{N} (I - G)^n * \overline{u}_i, \tag{13}$$

where the asterisk symbolizes the convolution. For a given filter the approximate inverse is easy to implement because it is obtained by a multiple application of the filter operation to the filtered function. When used in SGS modeling the inverse (13) leads to Approximate Deconvolution Model (ADM) of Stolz and Adams (1999). A similar expansion was used by Horiuti (2001), leading to a multi-level filtered model.

Other approaches to the problem of deconvolution in SGS modeling have been utilized though often without introducing explicitly an inversion operation (what may be called an 'implicit deconvolution'). Shah and Ferziger (1995) expand the unfiltered quantity in the integral (4) in the Taylor series around an LES mesh point, which leads to an expansion for the filtered quantity in terms of the derivatives of the exact quantity. These derivatives can be subsequently approximated using finite difference formulas on

the chosen discretization stencil, leading to a tridiagonal system of equations for the unfiltered quantity. The solution of the system provides the deconvolved velocity which is then used in the definition of the SGS stress (3). Geurts (1997) constructs an approximate inverse operator by requiring that polynomials up to a certain order are recovered exactly from their filtered counterparts. Domaradzki and Saiki (1997) and Kuerten *et al.* (1999) work with a Fourier representation of a grid function, i.e., with discretized version of (10). For a number of simple filters, such as the top-hat or the Gaussian, the inverse for a single Fourier mode can be easily obtained, and from this the numerical inverse for the entire filtered quantity.

The deconvolution offers a deceptively simple solution to the SGS modeling problem because it relies only on the definitions of the filter (4) and the SGS stress tensor (3) without any reference to the physics of turbulence. Since the need for the physical models is obviated this approach appears to be more promising than the classical models. The key word, however, is 'deceptively' because the closer inspection of the deconvolution concept reveals that its simplicity is only illusory. This is because the formal inversion formalism implicitly assumes infinite spectral support for both the unfiltered and filtered quantities. In such a case, if an inverse filter exists, the velocity u_i can be recovered exactly from the filtered velocity $\overline{u}_i$ and Eq. (1) can be viewed as a result of a simple change of dependent variables in the full Navier-Stokes equation from u_i to $\overline{u}_i$ and both equations are formally equivalent. This fact has long been recognized, e.g. by Zhou *et al.* (1989), Domaradzki and Loh (1999), Langford and Moser (2001), Winckelmans *et al.* (2001), and Domaradzki and Adams (2002), who provided critiques of such exact inversion procedures as a SGS modeling tool. The essence of the criticism is that the formal approach does not account for the fact that in an actual LES Eq. (1) is solved in a discretized form with the numerical resolution much less than required to represent full Navier-Stokes solution u_i. This is because, by design, the filter attenuates scales smaller than the filter width Δ and consequently the filtered velocity $\overline{u}_i$ can be accurately represented on a mesh with the mesh size $\Delta_{LES} \sim O(\Delta)$, which can be much larger than the mesh size Δ_{DNS} needed to represent the full Navier-Stokes field u_i in a direct numerical simulation. Therefore, in practical LES in addition to the explicit filter (4) an implicit projection of the field $\overline{u}_i$ is present that makes it possible to represent it on a finite mesh with the mesh size $\Delta_{LES} \gg \Delta_{DNS}$. In Fourier methods the LES projection is equivalent to an implicit sharp spectral filter with the cutoff wavenumber $k_c = \pi/\Delta_{LES}$. Because of the implicit filter the spectral support for the LES velocity $\overline{u}_i$ is much less than for the full velocity u_i and the formal inversion of the filtering operation can only recover the full velocity only up to the same truncation wavenumber k_c as the original LES field $\overline{u}_i$.

The traditional notation in LES usually combines the effects of the explicit spatial filtering and of the implicit projection onto a grid into one symbol, the overbar, creating a potential for misunderstanding of the deconvolution formalism in the SGS modeling. In discussing the deconvolution approaches it is thus beneficial to separate both operations using an explicit notation as proposed, for instance, by Winckelmans *et al.* (2001), Carati *et al.* (2001), and Domaradzki and Adams (2002). The latter reference reserves the overbar for the explicit, spatial filtering and the spectral LES truncation is denoted by the superscript '$\mathcal{L}$' and its complement by '$\mathcal{S}$', i.e., the full velocity field is decomposed as

$$u_i = u_i^{\mathcal{L}} + u_i^{\mathcal{S}} . \tag{14}$$

Assuming that the spatial filtering and the spectral truncation commute, both opera-

8

tions are applied to the Navier-Stokes equation giving

$$\frac{\partial}{\partial t}\overline{u_i}^{\mathcal{L}} + \frac{\partial}{\partial x_j}\overline{(u_i u_j)}^{\mathcal{L}} = -\frac{1}{\rho}\frac{\partial}{\partial x_i}\overline{p}^{\mathcal{L}} + \nu\frac{\partial^2}{\partial x_j \partial x_j}\overline{u_i}^{\mathcal{L}}.\tag{15}$$

The filtered and truncated product of velocities in (15) can be rewritten as follows

$$\overline{(u_i u_j)}^{\mathcal{L}} = (\overline{u_i}^{\mathcal{L}}\,\overline{u_j}^{\mathcal{L}})^{\mathcal{L}} + \left[\overline{(u_i^{\mathcal{L}} u_j^{\mathcal{L}})}^{\mathcal{L}} - (\overline{u_i}^{\mathcal{L}}\,\overline{u_j}^{\mathcal{L}})^{\mathcal{L}}\right] + \overline{\left[u_i^{\mathcal{L}} u_j^{\mathcal{S}} + u_i^{\mathcal{S}} u_j^{\mathcal{L}} + u_i^{\mathcal{S}} u_j^{\mathcal{S}}\right]}^{\mathcal{L}},\tag{16}$$

giving the following form of the LES equation

$$\frac{\partial}{\partial t}\overline{u_i}^{\mathcal{L}} + \frac{\partial}{\partial x_j}\left(\overline{u_i}^{\mathcal{L}}\,\overline{u_j}^{\mathcal{L}}\right)^{\mathcal{L}} = -\frac{1}{\rho}\frac{\partial}{\partial x_i}\overline{p}^{\mathcal{L}} + \nu\frac{\partial^2}{\partial x_j \partial x_j}\overline{u_i}^{\mathcal{L}} - \frac{\partial}{\partial x_j}(\tau_{ij}^{rep} + \tau_{ij}^{nrp}),\tag{17}$$

where

$$\tau_{ij}^{rep} = \overline{(u_i^{\mathcal{L}} u_j^{\mathcal{L}})}^{\mathcal{L}} - \left(\overline{u_i}^{\mathcal{L}}\,\overline{u_j}^{\mathcal{L}}\right)^{\mathcal{L}},\tag{18}$$

and

$$\tau_{ij}^{nrp} = \overline{\left(u_i^{\mathcal{L}} u_j^{\mathcal{S}} + u_i^{\mathcal{S}} u_j^{\mathcal{L}} + u_i^{\mathcal{S}} u_j^{\mathcal{S}}\right)}^{\mathcal{L}}.\tag{19}$$

The above form of the LES equations shows that the SGS stress tensor consists of two parts: τ_{ij}^{rep}, which results from the nonlinear interactions among scales represented on a numerical grid and τ_{ij}^{nrp}, which accounts for the the nonlinear interactions that involve scales that are not represented on a grid.

If the spatial filtering operation is invertible, $u_i^{\mathcal{L}}$ can be obtained from $\overline{u_i}^{\mathcal{L}}$, and τ_{ij}^{rep} can be evaluated without any SGS modeling. However, in such a case the term τ_{ij}^{nrp} vanishes because defiltering does not recover subgrid scales $\mathcal{S}$ lost due to the projection of all quantities onto a coarse LES grid. Therefore, τ_{ij}^{rep} would be the total SGS stress that can be obtained from a known LES velocity using the exact deconvolution. If τ_{ij}^{nrp} is neglected in the LES equation (15), the entire equation can be deconvolved giving

$$\frac{\partial}{\partial t}u_i^{\mathcal{L}} + \frac{\partial}{\partial x_j}(u_i^{\mathcal{L}} u_j^{\mathcal{L}})^{\mathcal{L}} = -\frac{1}{\rho}\frac{\partial}{\partial x_i}p^{\mathcal{L}} + \nu\frac{\partial^2}{\partial x_j \partial x_j}u_i^{\mathcal{L}},\tag{20}$$

which is the Navier-Stokes equation for the resolved velocity $u_i^{\mathcal{L}}$. Therefore the application of such an exact deconvolution in LES is no different from solving the equivalent, Navier-Stokes equation for the de-filtered velocity on a domain truncated to the LES cutoff. In terms of numerical simulations it means that LES is equivalent to DNS performed on the coarse LES mesh and the LES results can be simply obtained from the coarse-mesh DNS data by the spatial filtering. At higher Reynolds numbers such DNS are generally under-resolved. In the case of isotropic turbulence at very high Reynolds numbers the dynamics of the resolved modes in such simulations will be essentially inviscid, leading to the equipartition of energy. In such a state the energy flux between different modes vanishes on average and so does the associated SGS dissipation in the equivalent LES.

Therefore, the pure deconvolution formalism, when implemented on a coarse LES mesh will fail as a subgrid scale modeling tool for high Reynolds number flows.

The main reason why the deconvolution models in actual numerical implementations seem to work is because they do not evaluate τ_{ij}^{rep} exactly but rather approximate it, in the process generating an implicit expression of the similar form as (19). For instance, the approximate deconvolution model (ADM) of Stolz and Adams (1999) in its first formulation did not provide an explicit model for the term τ_{ij}^{nrp} and yet excellent results were obtained for decaying compressible isotropic turbulence. In ADM an approximation for u_i is obtained from (13)

$$u_i \approx \tilde{u}_i^{\mathcal{L}} \equiv \sum_{n=0}^{N} (I - G)^n * \overline{u}_i^{\mathcal{L}} = Q_N * \overline{u}_i^{\mathcal{L}} \; , \tag{21}$$

where tilde in $\tilde{u}_i^{\mathcal{L}}$ indicates the approximation to the actual large scale component of the velocity $u_i^{\mathcal{L}}$ that would be obtained from the exact deconvolution. The leading-order term of the deconvolution error is

$$\delta u_i^{\mathcal{L}} = \tilde{u}_i^{\mathcal{L}} - u_i^{\mathcal{L}} = \mathcal{C}_j (-1)^{(N+1)} \Delta^{r(N+1)} \frac{\partial^{r(N+1)} u_i^{\mathcal{L}}}{\partial x_j^{r(N+1)}} \tag{22}$$

where $\mathcal{C}_j$ depends on the filter kernel which is of order r, and a tensorial extension of (4) to multiple dimensions is assumed (Domaradzki and Adams 2002). Inserting $\tilde{u}_i^{\mathcal{L}}$ for $u_i^{\mathcal{L}}$ into (18) results in

$$\tau_{ij}^{rep} = \overline{(u_i^{\mathcal{L}} u_j^{\mathcal{L}})}^{\mathcal{L}} - \left(\overline{u_i}^{\mathcal{L}} \, \overline{u_j}^{\mathcal{L}} \right)^{\mathcal{L}} + \overline{\left(u_i^{\mathcal{L}} \delta u_j^{\mathcal{L}} + \delta u_i^{\mathcal{L}} u_j^{\mathcal{L}} + \delta u_i^{\mathcal{L}} \delta u_j^{\mathcal{L}} \right)}^{\mathcal{L}} \tag{23}$$

with the last term, which is due to the regularized deconvolution, providing a model for τ_{ij}^{nrp}. Clearly, such a model will depend on the primary filter and details of the deconvolution, e.g., parameter N, and thus lacks a physical basis. In high Reynolds number flows ADM suffers from insufficient dissipation and must be supplemented by a dissipative model for the term τ_{ij}^{nrp} in (17), a problem similar to that faced by the classical similarity models. ADM with the relaxation term designed to provide additional dissipation has been proposed and evaluated by Stolz *et al.* (2001a,b).

Thus the primary conclusion concerning defiltering procedures in LES is that such LES are fundamentally equivalent to under-resolved DNS because they neglect the term τ_{ij}^{nrp} in Eq. (17) which is the only term that provides a physically realistic mechanism for the SGS dissipation. This term accounts for interactions with the subgrid scales with sizes below those that can be represented on the LES mesh and which cannot be recovered by the deconvolution procedures. In practical LES this equivalence may be obscured by additional numerical effects, e.g., an approximate deconvolution may provide a dissipation mechanism absent for the exact deconvolution. Nevertheless the subgrid scales not represented on the numerical grid cannot be produced by the formal inversion of a filter, either exact or approximate and, in general, there is no substitute for modeling their effects. In that respect the deconvolution models are no different from the similarity models: both do not contain information about actual subgrid scales and because of that require extraneous dissipation mechanisms, provided by eddy viscosity or relaxation expressions.

A different application of an explicit, convolution filter and its approximate inversion is regularization of the Navier-Stokes equations obtained by filtering not the full equations but only the advective velocity, known as the alpha-model (Foias *et al.* (2001)). Holm and Domaradzki (2001) and Geurts and Holm (2003) showed that the regularized Navier-Stokes equations can be transformed into the usual LES form with the specific expressions for the SGS stress tensor. These expression are reminiscent of the generalized similarity/deconvolution models and thus both types of models are expected to behave in the same manner in actual LES.

4.   Subgrid Scale Estimation Models

In order to obtain nonvanishing τ_{ij}^{nrp} the estimation procedures provide expressions for the the subgrid velocity u_j^S in terms of the large scale velocity $u_j^{\mathcal{L}}$. Such a modeled velocity is sometimes called the estimated subgrid scale velocity or the synthetic velocity. The total modeled velocity is then simply a sum of the known $u_j^{\mathcal{L}}$ and the estimated SGS velocity u_j^S and is used to compute the SGS stress tensor from its definition (3).

Scotti and Meneveau (1999) construct the subgrid scales from the known resolved scales using the fractal interpolation technique. The simplest application of the procedure gives the model that does not produce enough SGS dissipation. This deficiency can be corrected by tuning model parameters to get the best alignment of the computed SGS stress with the resolved rate-of-strain. Enforcing the best alignment is similar to the assumption underlying the eddy viscosity models. Another example of using synthetic fields is the so-called additive turbulent decomposition proposed by Hylin and McDonough (1999). Separate equations are written for large and small scales in the decomposition and the equations for the large scales depend explicitly on the small scales. The small, synthetic scales are constructed as stochastic variables determined from one-dimensional chaotic maps, substituted into equations for the large scales, and the equations are advanced in time. Kerstein (1999) developed the one-dimensional turbulence (ODT) model which has been evaluated in LES of free shear flows and wall bounded flows (Kerstein *et al.* 2001, Kemenov and Menon 2002). The essence of ODT is to represent a three-dimensional turbulent field through a one dimensional line of data, which in LES extends across a volume determined by the neighboring LES mesh points. The flow variables are defined along the line with the numerical resolution sufficient to explicitly account for viscous effects and provide a model for SGS quantities. The modeled SGS quantities are then used to calculate SGS fluxes needed to advance in time the LES equations.

Rather than using one dimensional procedures, other approaches work with three dimensional models of subgrid scales. Pullin and Saffman (1994) proposed that subgrid scales are a collection of vortical structures with prescribed properties. Stretching of these vortices by the resolved field provides the mechanism for the energy transfer from the resolved to subgrid scales, i.e., the mechanism for the SGS dissipation. With additional assumptions the analytical formulas for the SGS vortices allow to derive an expression for the SGS stress tensor which can be used in the LES equations. The model has been implemented in the spectral space by Misra and Pullin (1997) and in the physical space representation by Voelkl *et al.* (2000), and also applied to a passive scalar mixing by Pullin (2000). Modeling of subgrid-scale vorticity has been also explored by Kerr and Domaradzki (1996). In that work the subgrid-scale vorticity is confined to a range of wavenumbers outside the resolved range, used for de-aliasing of pseudo-spectral simulations. The model is based on the vorticity production in that range by the resolved

scales. The modeled subgrid-scale vorticity was used to compute the SGS quantities which compared favorably with the exact quantities in *a priori* tests.

The subgrid-scale estimation model introduced by Domaradzki and Saiki (1997) attempts to model, or estimate, the unfiltered velocity field appearing in the definition of the subgrid-scale stress tensor. It consists of two steps. In the kinematic step an approximate inversion of the filtering operation is performed producing defiltered field $\tilde{u}_i^{\mathcal{L}}$. The next, dynamic, or nonlinear, step, generates the subgrid scales twice smaller than the smallest scales resolved on the LES mesh, producing a perturbation velocity $\tilde{u}_i^{\mathcal{S}}$. In order to be able to represent these subgrid scales a mesh finer than the LES mesh is explicitly introduced by halving the coarse LES mesh in each Cartesian direction. The full velocity u_i is approximated by the estimated velocity $\tilde{u}_i$

$$u_i \approx \tilde{u}_i = \tilde{u}_i^{\mathcal{L}} + \tilde{u}_i^{\mathcal{S}}. \tag{24}$$

The estimated velocity on the fine mesh is used to compute the SGS stress directly from the definition on the coarser LES mesh. The SGS estimation model was applied to LES of low Reynolds number incompressible turbulence in channel flow by Domaradzki and Saiki (1997), Domaradzki and Loh (1999), Loh and Domaradzki (1999), to spatially evolving compressible turbulence by Domaradzki *et al.* (1998), Dubois *et al.* (2002), and to Rayleigh-Bénard convection by Kimmel and Domaradzki (2000).

The models described above share frequently with the similarity and deconvolution models the same problem of the insufficient SGS dissipation. The reason for that can be understood by noting that the SGS dissipation reflects coupling between resolved and subgrid scales which is induced by the Navier-Stokes dynamics. For instance, it is known that velocity fields obtained in spectral DNS lose the ability to sustain the energy flux characteristic of turbulence if phases of the complex velocity modes are randomized, even if their amplitudes are preserved. Only the dynamics through Navier-Stokes equations, acting over sufficiently long time, will induce the proper phase relationships between resolved and subgrid scales that are required for the turbulent energy cascade. Therefore, the insufficient SGS dissipation in the estimation models implies that the estimated subgrid scale quantities are deficient in modeling the phase relationships that are consistent with the Navier–Stokes dynamics. In the next section we describe models that address this deficiency.

5. Explicit Filtering, Implicit Dissipation, and Constrained SGS Models

Domaradzki and Yee (2000) proposed an approach that addresses the insufficient SGS dissipation in the original estimation model at high Reynolds numbers without introducing eddy viscosity expressions. The method is based on the observation that in the original estimation procedure a single act of nonlinear interactions among large scale, obtained through a single time step computation of the nonlinear term, determines the modeled perturbation velocity $\tilde{u}_i^{\mathcal{S}}$. However, the actual process of generation of subgrid scales involves much larger number of nonlinear interactions, i.e. involving multiple computations of nonlinear term over many time steps, covering approximately one large eddy turnover time. This suggests that the realism of the modeled velocity field can be improved by allowing additional nonlinear interactions in its generation. This goal is

accomplished by allowing the total estimated velocity $\tilde{u}_i$, Eq. (24) to evolve according to the truncated Navier-Stokes (TNS) equations on the fine mesh

$$\frac{\partial}{\partial t}\tilde{u}_i + \frac{\partial}{\partial x_j}\tilde{u}_i\,\tilde{u}_j = -\frac{1}{\rho}\frac{\partial}{\partial x_i}\tilde{p} + \nu\frac{\partial^2}{\partial x_j\partial x_j}\tilde{u}_i \tag{25}$$

$$\frac{\partial}{\partial x_i}\tilde{u}_i = 0. \tag{26}$$

The term 'truncated' applied to equations (25)-(26) refers not to the form of the equations, which is no different from the form of the full Navier-Stokes equations, but to the limited numerical resolution used to solve these equations. The procedure consists of several steps, symbolically represented as follows

$$\overline{u}_i(t) \overset{deconv.}{\to} \tilde{u}_i^{\mathcal{C}}(t) \to \left[\tilde{u}_i^{\mathcal{C}}(t) + \tilde{u}_i^{\mathcal{S}}(t)\right] \overset{N-S}{\to} \tilde{u}_i(t+T) \to \left[\tilde{u}_i(t+T) - \tilde{u}_i^{\mathcal{S}}(t)\right] \overset{filter}{\to} \overline{u}_i(t+T). \tag{27}$$

The LES velocity $\overline{u}_i$ at time t is given on a coarse mesh and is first defiltered through an exact or approximate deconvolution, giving $\tilde{u}_i^{\mathcal{C}}$. This field is interpolated to a finer mesh, obtained normally by halving a mesh size for the coarse mesh, and the SGS velocity $\tilde{u}_i^{\mathcal{S}}$ is generated using the velocity estimation model. The combined field is then advanced over time T using truncated Navier-Stokes equations (25)-(26), which results in enhancing nonlinear couplings between large and small scales. The purpose of the remaining two steps is to obtain the filtered LES velocity after the time period T. Note that rather than simply filtering the Navier-Stokes solution $\tilde{u}_i(t+T)$, the original perturbation velocity at time t, $\tilde{u}_i^{\mathcal{S}}(t)$, is first subtracted, followed by filtering and sampling of the result on the coarse mesh. The subtraction is introduced to avoid spurious dynamics by the combination of the estimation step and the reduction step. This way if the procedure is applied without the Navier-Stokes evolution the initial field $\overline{u}_i$ is recovered exactly at the end of the reduction step, i.e., modifications of the filtered field $\overline{u}_i$ are caused only by the truncated Navier-Stokes dynamics of the estimated velocity $\tilde{u}_i$. For flows at high Reynolds numbers the fine mesh used is still far too coarse to resolve all relevant scales and the truncated Navier-Stokes equations would eventually lead to the unphysical equipartition of energy at large wavenumbers. The filtering and sampling to a coarse LES mesh, applied every period T, prevents the accumulation of the energy in the small scales. Therefore, the time T must be short enough to prevent equipartition but long enough to allow the sufficient nonlinear couplings between large and small scales to develop. It was found that the time T can be chosen as the eddy turnover time for the smallest resolved scales. Because the Navier-Stokes equations are used to induce nonlinear couplings between the large and small scales and thus the corresponding energy flux, the method is less dependent on the accuracy of the prediction for the initial estimated velocity $\tilde{u}_i^{\mathcal{S}}(t)$. Even setting $\tilde{u}_i^{\mathcal{S}}(t)$ simply to zero and allowing the truncated Navier-Stokes equations to generate subgrid scales over time T can often be sufficient to obtain accurate LES results as shown by Domaradzki and Horiuti (2001) and Yang and Domaradzki (2004).

Operationally, the LES procedure (27) consists of a number of Navier-Stokes runs performed on the fine mesh without any explicit model and re-initialization, involving filtering and sampling to the coarser LES mesh, every time period T. Since all quantities between defiltering and filtering steps are represented on the fine mesh, and the Navier-Stokes equations are solved on the same mesh, the method can be further simplified by

removing the deconvolution part of the procedure entirely as suggested by Domaradzki *et al.* (2002). This modification uses only the large scale velocity $\tilde{u}_i^{\mathcal{L}}$ obtained from the TNS solution by the appropriate filtering, symbolically

$$\tilde{u}_i^{\mathcal{L}}(t) \rightarrow [\tilde{u}_i^{\mathcal{L}}(t) + \tilde{u}_i^{\mathcal{S}}(t)] \stackrel{N-S}{\rightarrow} \tilde{u}_i(t+T) \stackrel{filter}{\rightarrow} \tilde{u}_i^{\mathcal{L}}(t+T). \tag{28}$$

In simulations using (28) only a single, fine mesh is employed. For high Reynolds number flows the TNS method is thus equivalent to a sequence of under-resolved Navier Stokes simulations with periodic filtering of the numerical solution. There are several advantages of such an approach: since only a solution is periodically modified, an underlying Navier-Stokes solver can be used in the same form for DNS and LES; the method is easily generalized to model other nonlinear phenomena, e.g., convective or compressible turbulent flows, by periodically filtering corresponding flow variables; the difficulties with transformation properties for the modeled SGS stresses (Horiuti 2001) are avoided. The obvious problem with this approach is that the periodic filtering generates a discontinuous in time solution $\tilde{u}_i$. This problem is less serious than it appears because in LES one is interested only in the large scale component $\tilde{u}_i^{\mathcal{L}}$, while the small scale component $\tilde{u}_i^{\mathcal{S}}$ is considered to be a model; by design, typical filters used affect only the small scales in the method and discontinuity in the large scales is minimized. The discontinuity can be entirely removed if the procedure is formulated in the framework of the LES equations coupled with the TNS (Domaradzki *et al.* 2002)). The TNS equations are advanced in time and at each time step a SGS stress tensor is calculated using the velocity $\tilde{u}_i$

$$\tau_{ij}^{(LES)} = \left[\overline{(\tilde{u}_i \tilde{u}_j)} - \overline{\tilde{u}}_i \, \overline{\tilde{u}}_j \right]^{(LES)}, \tag{29}$$

where the notation indicates that the SGS stress is computed from the estimated velocity $\tilde{u}_i$ given on the fine mesh, using the overbar filter and sampling on a coarser LES mesh. The SGS stress computed this way is used as the approximation to the actual SGS stress to advance in time the LES equations (1) discretized on the LES mesh. The discontinuity in $\tilde{u}_i$, introduced by the periodic in time filtering, is considerably reduced by the overbar filtering and sampling involved in computing (29). This results in a smooth evolution of the LES velocity $\overline{\tilde{u}}_i$, more so that the SGS term in LES equations is much smaller than the resolved nonlinear term. Such considerations imply that the implementation of TNS described above is preferred; however, it is quite cumbersome and costly because two sets of equations on two different meshes must be solved numerically. Because of that, in practice the implementation (28) on a single, fine mesh is used and the discontinuity in the numerical solution is tolerated.

The TNS method depends formally on the filter used and the filtering interval T. The filter dependence has not been investigated in detail but the dependence appears weak for filters that affect only the small scales, determined by wavenumbers between $1/2k_c$ and k_c, where k_c is the mesh cutoff. The filtering interval is a free parameter, normally chosen by trial and error, using the physical guideline that it is determined by the eddy turnover time of the subgrid scales. Once the optimal selection is made, the results of LES are only weakly dependent on the filtering interval; the variation within a factor of two gives acceptable results. Recently, Tantikul and Domaradzki (2010) have shown that for a prescribed filter, the filtering interval T can be determined automatically in the course of the simulations using a criterion based on the energetics of the modeled subgrid scales. This way, for a given filter, the method becomes parameter-free.

14

Another way of modifying the estimation concept to produce sufficient SGS dissipa-
tion was used by Park and Mahesh (2008). They proposed the resolved subgrid scale
estimation model (RSEM) which constraints the SGS stress to match, in the mean or
least squares sense, the SGS dissipation of the dynamic Smagorinsky model for the same
velocity field. The model does not have the eddy viscosity form, but the extraneous con-
straint guarantees that the total SGS dissipation is comparable to that produced by a
selected eddy viscosity model.

The fact that TNS solves Navier-Stokes equations without any modeling terms is su-
perficially similar to the so-called implicit LES, the approach that was originally proposed
by Boris *et al.* (1992) and reviewed recently in the monograph edited by Grinstein *et al.*
(2007). In ILES the Navier-Stokes equations, also without any SGS models, are solved
numerically on a coarse LES mesh using higher-order nonoscillatory methods, such as
total variation diminishing (TVD), flux-corrected-transport (FCT) and flux-limited and
sign-preserving schemes (Sweby 1984, Zalesak 1979, Harten *et al.* 1987)), originally de-
veloped to control numerical oscillations in problems involving steep gradients and/or
discontinuities such as shocks. The ILES methodology was initially justified on the basis
of a practical observation that truncation errors in such discretizations of Navier-Stokes
equations introduce numerical dissipation and its effect is qualitatively similar to the
effects of the explicit SGS models. For instance, Porter and Woodward (1994) report the
development of the $k^{-5/3}$ energy spectrum in numerical simulations of decaying isotropic
turbulence performed using piecewise parabolic method (PPM) implemented in an Euler
solver, i.e., for equations without any explicit viscous terms. While such results can be
used to support the ILES methodology, it is also possible to find counterexamples. For
instance, Garnier *et al.* (1999) analyzed several different shock-capturing Euler schemes
applied to decaying isotropic turbulence and the conclusions were less favorable. While
it was possible to obtain the inertial subrange, the other results, e.g, pdfs of the velocity
derivatives and pressure showed a behavior typical of low Reynolds number flows rather
than expected from high Reynolds number LES. This behavior was attributed to the
fact that the numerical dissipation was often much greater than the SGS dissipation
computed for the same field using the Smagorinsky model. Based on these results ILES
may provide substantially more numerical dissipation than expected based on the physics
of turbulent cascade. Similar conclusions were reached by Domaradzki and Radhakrish-
nan (2005) who showed that the ILES results for rotating and non-rotating turbulence
were sensitive to the time step and the method failed to produce theoretically expected
results for certain initial conditions and for rotating turbulence. Therefore, while ILES
offers the ease of implementation because only Navier-Stokes equations are being solved,
the uncertainty regarding the numerical dissipation may negate potential advantages.

Recently, Hickel *et al.* (2006) demonstrated that the ILES methodology can be made
viable by developing a specific method that respects the physical requirements for the
energy transfer in turbulence. The method is based on a new nonlinear discretization
scheme, the adaptive local deconvolution method (ALDM), which contains several free
deconvolution parameters that allow to control the truncation error of the scheme. The
free parameters are constrained such that the numerical viscosity optimally matches the
theoretical eddy viscosity predicted by the analytical theories of turbulence. While the
optimization was performed for isotropic turbulence, the parameters of the scheme can
be used to simulate other turbulent flows without explicit SGS models.

ILES and TNS are related to other procedures for underresolved simulations of tur-
bulence that rely on purely numerical techniques to achieve stable simulations. In the
so-called stabilized spectral LES (Minguez *et al.* 2009) the numerical stability is not pro-

vided by the truncation error of the numerical discretization (which is exponentially small for a spectral method (Boyd 2001)) but by the spectral filter applied at each time step that strongly attenuates the small resolved scales. In the same spirit Bogey and Bailly (2006) use an explicit filter applied every few time steps as a substitute for a SGS model in LES of a turbulent jet flow. However, one must be aware that simply guaranteeing numerical stability does not guarantee physically correct dynamics of the resolved scales. Therefore, the results from such LES have to be always compared with experiments and simulations, either fully resolved DNS, or LES performed with other models, to gain confidence that the method is not only numerically stable but also physically correct.

In this section we have focused on procedures that use either explicit filters or implicit dissipation and/or constraints that result in the SGS dissipation of a model to be consistent with the turbulence dynamics. It appears that such approaches offer greatest promise in developing viable methods that are sufficiently dissipative and do not incorporate explicit eddy viscosity expressions in the governing LES equations.

6. Conclusions

The traditional models of subgrid scale terms such as a stress tensor or a heat flux usually employ eddy viscosity concepts. The primary contribution of the eddy viscosity models is to provide the mean SGS dissipation, which can represent accurately the global energy flux if the model constants are properly chosen. However, many other features of SGS terms are poorly represented by the eddy viscosity models, providing a motivation for research on alternative approaches. In this paper we have focused on those modeling approaches that specifically exclude any use of the explicit eddy viscosity expressions in the LES equations, either in the main or in the supporting role. Such an exclusion allows to evaluate merits of each approach in its own right. We have discussed the similarity models, the deconvolution and nonlinear models, the estimation models, the implicit (numerical) models, and the explicit filtering of a numerical solution. There are a number of advantages offered by such methods. For instance, most of these models naturally provide both the dissipative forward transfer and the anti-dissipative backscatter of energy, contrary to the eddy viscosity models that are purely dissipative. Such modeling procedures are good candidates for modeling strongly anisotropic flows because often their derivations do not require assumptions of local isotropy and of the inertial range. Moreover, the modeling principles can be extended without difficulty to model additional physical effects, e.g. the density variations in convective, stably stratified, and compressible turbulence. Finally, such methods also avoid difficulties associated with the transformation properties between different frames of reference encountered by the classical eddy viscosity models.

Despite the potential advantages listed above, many non-eddy viscosity approaches suffer from the insufficient subgrid scale dissipation, often leading to their failure in actual LES. When faced with the insufficient SGS dissipation the temptation is to add an eddy viscosity model. This, of course, largely defeats the idea of developing new SGS models because it is clear that it is the presence of the eddy viscosity expressions that makes the combined models work in actual LES. A better approach might be to try to understand the fundamental reasons for observed failures in the hope that they can be corrected. However, the reasons for the observed failures are not always clear in the literature on the subject. One of the goals of this paper was to provide heuristic explanations. The similarity model was shown to be deficient in removing the energy from the vicinity of the LES

cutoff and compounding the problem by increasing the energy loss by the large scales. In a particular case of an exact deconvolution the insufficient SGS dissiption was shown to be a result of the fundamental equivalence between the model and under resolved direct numerical simulations. The estimation model includes scales beyond the resolution of an LES mesh which, in principle, should provide a physically viable mechanism for the SGS energy transfer. However, even in this case the estimation models were found not to provide enough SGS dissipation for flows at high Reynolds numbers. In the algorithmic estimation procedures the source of insufficient SGS dissipation usually is attributed to an inability of the models to predict the proper phase relationship between known, resolved scales and unknown subgrid scales. This relationship is a result of a complicated process, involving multiple nonlinear interactions between resolved and subgrid scales, acting over at least one large eddy turnover time, as well as of the pressure effects. These effects can only be captured using the dynamic equations for the subgrid scales as is done in the TNS approach. It is also possible to design an estimation-like model with the sufficiently high SGS dissipation if an extraneous condition is used that constrains the SGS dissipation of the model by the SGS dissipation of the eddy viscosity model for the same velocity field. ILES is another class of models that do not use explicit eddy viscosity expressions. In ILES only Navier-Stokes equations are being solved, thus offering a relative ease of the implementation, but this advantage is largely negated by the uncertainty how the numerical dissipation is related to the actual SGS energy flux. The promising way around this problem is to constrain the numerical dissipation to be consistent with the eddy viscosity predicted by the analytical theories of turbulence. Finally, we have reviewed approaches that rely on the explicit filtering of a numerical solution. They fall into two classes. One uses explicit filtering to simply stabilize the numerics and counts on the correct energy removal rate from the system as a byproduct, making such approaches similar to ILES. Another, employs filtering coupled with the physical considerations of the energy transfer in turbulence to determine the filter strength and/or frequency of its application. The example of such an approach is TNS.

In this review we have focused on general concepts of non-eddy viscosity approaches to subgrid-scale modeling without discussing results of specific LES performed with these SGS models. Such results are available in the quoted references and mostly deal with fully turbulent flows though transition to turbulence is sometimes addressed (Schlatter *et al.* (2004)). The non-eddy viscosity models are tested as any turbulence models using comparisons with available experimental and DNS data. Additionally, since the motivation is to replace eddy viscosity models, comparisons against benchmark LES results obtained with eddy viscosity models are common. The latter dictates that the numerical resolution and the time step are the same or comparable for both types of models. For instance, tests of TNS reported recently by Tantikul and Domaradzki (2010) for turbulent channel flow for Re_τ varying from around 200 to 2000 use a grid that is appropriate for LES performed with the dynamic Smagorinsky model (Piomelli (1993)) and consistent with the requirements for wall resolved LES (Sagaut (2002)). The total number of mesh points used in such LES can be as low as a few tenths of one percent of a DNS resolution, giving significant savings in terms of computational effort.

Acknowledgements

References

Bardina, J., Ferziger, J., and Reynolds, W., Improved turbulence models based on large eddy simulation of homogeneous incompressible turbulence. , 1983. , Technical report TF-19, Stanford University.

Bogey, C. and Bailly, C., 2006. Large eddy simulations of transitional round jets: influence of the Reynolds number on the flow development and energy dissipation. *Phys. Fluids*, 18, 065101.

Boris, J., *et al.*, 1992. New insights into large eddy simulation. *Fluid Dyn. Res.*, 10, 199–228.

Borue, V. and Orszag, S., 1998. Local enegy flux and subgrid-scale statistics in three-dimensinal turbulence. *J. Fluid Mech.*, 366, 1–31.

Boussinesq, J., 1877. Essai sur la théorie des eaux courantes. *Mém. prés. par div. savants a l'Acad. Sci. Paris*, 23, 1–680.

Boyd, J.P., 2001. *Chebyshev and Fourier Spectral Methods*. Mineola, New York: Dover.

Carati, D., Winckelmans, G., and Jeanmart, H., 2001. On the modelling of the subgrid-scale and filtered-scale stress tensors in large-eddy simulation. *J. Fluid Mech.*, 441, 119–138.

Clark, R.A., Ferziger, J.H., and Reynolds, W.C., 1979. Evaluation of subgrid-scale models using an accurately simulated turbulent flow. *Journal of Fluid Mechanics*, 91 (01), 1–16.

Domaradzki, J.A. and Adams, N.A., 2002. Direct modelling of subgrid scales of turbulence in large eddy simulations. *J. Turbulence*, 3, 1–19.

Domaradzki, J.A., Dubois, T., and Honein, A., 1998. The Subgrid-Scale Estimation Model Applied to Large Eddy Simulations of Compressible Turbulence. *In: Proceedings of the 1998 Summer Program*, p. 351.

Domaradzki, J.A. and Horiuti, K., 2001. Similarity modeling on an expanded mesh applied to rotating turbulence. *Phys. Fluids*, 13, 3510–3512.

Domaradzki, J.A., Loh, K., and Yee, P.P., 2002. Large eddy simulations using the subgrid-scale estimation model and truncated Navier-Stokes dynamics. *Theor. Comput. Fluid Dyn.*, 15, 421–450.

Domaradzki, J.A. and Saiki, E.M., 1997. A subgrid-scale model based on the estimation of unresolved scales of turbulence. *Phys. Fluids*, 9, 2148–2164.

Domaradzki, J.A. and Yee, P.P., 2000. The subgrid-scale estimation model for high Reynolds number turbulence. *Phys. Fluids*, 12, 193–196.

Domaradzki, J., Liu, W., and Brachet, M., 1993. An analysis of subgrid-scale interactions in numerically simulated turbulence. *Phys. Fluids A*, 5, 1747.

Domaradzki, J., *et al.*, 1994. Energy transfer in numerically simulated wall-bounded turbulent flows. *Phys. Fluids*, 6, 1583–1599.

Domaradzki, J. and Loh, K., 1999. The subgrid-scale estimation model in the physical space. *Phys. Fluids*, 11, 2330.

Domaradzki, J. and Radhakrishnan, S., 2005. Effective eddy viscosities in implicit modeling of decaying high Reynolds number turbulence with and without rotation. *Fluid Dyn. Res.*, 36, 385–406.

Domaradzki, J. and Rogallo, R., 1990. Local energy transfer and nonlocal interactions in homogeneous, isotropic turbulence. *Phys. Fluids A*, 2, 413–426.

Dubois, T., Domaradzki, J.A., and Honein, A., 2002. The Subgrid-Scale Estimation Model Applied to Large Eddy Simulations of Compressible Turbulence. *Phys. Fluids*, 14, 1781–1801.

Foias, C., Holm, D., and Titi, E., 2001. The Navier-Stokes-alpha model of fluid turbu-
lence. *Physica D*, 152, 505.

Galperin, B. and Orszag, S.A., 1993. *Large eddy simulation of complex engineering and
geophysical flows*. Cambridge: Cambridge University Press.

Garnier, E., *et al.*, 1999. On the use of shock-capturing schemes for large-eddy simulation.
J. Comput. Phys., 153, 273–311.

Germano, M., 1986. Differential filters of elliptic type. *Phys. Fluids*, 29, 1757.

Germano, M., *et al.*, 1991. A dynamic subgrid-scale eddy viscosity model. *Phys. Fluids*,
3, 1760.

Geurts, B., 1997. Inverse modeling for large-eddy simulation. *Phys. Fluids*, 9, 3585–3587.

Geurts, B. and Holm, D., 2003. Regularization modeling for large-eddy simulation. *Phys.
Fluids*, 15, L13–L16.

Ghosal, S. and Moin, P., 1995. The basic equations of the large eddy simulation of
turbulent flows in complex geometry. *J. Comp. Phys.*, 118, 24.

Grinstein, F., Margolin, L., and Rider, W., 2007. *Implicit large eddy simulation*. Cam-
bridge University Press.

Harten, A., *et al.*, 1987. Uniformly high-order accurate essentially non-oscillatory schemes
III. *J. Comp. Phys.*, 71, 231.

Hickel, S., Adams, N.A., and Domaradzki, J.A., 2006. An adaptive local deconvolution
method for implicit LES. *J. Comp. Phys.*, 213, 413–436.

Holm, D. and Domaradzki, J., 2001. Modern Simulation strategies for Turbulent Flow*In:
Navier-Stokes alpha model: LES equations with nonlinear dispersion.*, 107–122
Philadelphia: R.T. Edwards.

Horiuti, K., 2001. Rotational transformation and geometrical correlation of SGS models..
In: B. Geurts, ed. *Modern Simulations Strategies for Turbulent Flow* Philadelphia:
R.T. Edwards, Inc., 123–140.

Hylin, E. and McDonough, J., 1999. Chaotic small-scale velocity fields as prospective
models for unresolved turbulence in an additive decomposition of Navier-Stokes
equations. *Int. J. Fluid Mech. Res.*, 26, 539–567.

Iliescu, T., *et al.*, 2003. A numerical study of a class of LES models. *Int. J. Comput.
Fluid Dyn.*, 17, 75–85.

Jacquin, L., *et al.*, 1990. Homogeneous turbulence in the presence of rotation. *J. Fluid
Mech.*, 220, 1.

Kemenov, K. and Menon, S., 2002. TLS: a new two level simulation methodology for
high-Reynolds LES. *AIAA paper*, 0287.

Kerr, R. and Domaradzki, J.and Barbier, G., 1996. Small-scale properties of nonlinear
interactions and subgrid-scale energy transfer in isotropic turbulence. *Phys. Fluids*,
8, 197.

Kerstein, A., 1999. One-dimensional turbulence: model formulation and application to
homogeneous turbulence, shear flows, and buoyant stratified flows. *J. Fluid Mech.*,
392, 277 – 334.

Kerstein, A., *et al.*, 2001. One-dimensional turbulence: vector formulation and application
to free shear flows. *J. Fluid Mech.*, 447, 85–109.

Kimmel, S. and Domaradzki, J., 2000. Large Eddy Simulations of Rayleigh-Bénard Con-
vection Using Subgrid Scale Estimation Model. *Phys. Fluids*, 12, 169.

Kobayashi, H. and Shimomura, Y., 2001. The performance of dynamic subgrid-models
in the large eddy simulation of rotating homogeneous turbulence. *Phys. Fluids*, 13,
2350 – 2360.

Kuerten, J., *et al.*, 1999. Dynamic invrse modeling and its testing in large-eddy simula-

tions of the mixing layer. *Phys. Fluids*, 11, 3778.

Langford, J.A. and Moser, R.D., 2001. Optimal LES formulations for isotropic turbu-
lence. *J. Fluid Mech.*, 398, 321–346.

Leonard, A., 1974. Energy cascade in large eddy simulations of turbulent fluid flows.
Adv. Geophys., 18A, 237–248.

Leonard, A., 1997. Large-eddy simulation of chaotic convection and beyond. *AIAA paper*,
97-0204.

Lesieur, M. and Métais, O., 1996. New trends in large-eddy simulations of turbulence.
Annu. Rev. Fluid. Mech., 28, 45–82.

Liu, S., Meneveau, C., and Katz, J., 1994. On the properties of similarity subgrid-scale
models as deduced from measurements in a turbulent jet. *J. Fluid Mech.*, 275, 83–
119.

Loh, K. and Domaradzki, J., 1999. The subgrid-scale estimation model on non-uniform
grids. *Phys. Fluids*, 11, 3786.

Meneveau, C. and Katz, J., 2000. Scale-invariance and turbulence models for large eddy
simulations. *Annu. Rev. Fluid Mech.*, 32, 1–32.

Minguez, M., Pasquetti, R., and Serre, E., 2009. Spectral vanishing viscosity stabilized
LES of the Ahmed body turbulent wake. *J. Comp. Phys.*, 5, 635–648.

Misra, A. and Pullin, D., 1997. A vortex-based subgrid stress model for large-eddy sim-
ulation. *Phys. Fluids*, 9, 2443.

Morinishi, Y., Nakabayashi, K., and Ren, S.Q., 2001. A new DNS algorithm for rotating
homogeneous decaying turbulence. *Int. J. Heat and Fluid Flow*, 22, 30–38.

O'Neil, J. and Meneveau, C., 1997. Subgrid-scale stresses and their modeling in a turbu-
lent plane wake. *J. Fluid Mech.*, 349, 253–293.

Park, N. and Mahesh, K., 2008. A velocity-estimation subgrid model constrained by
subgrid scale dissipation. *J. Comp. Phys.*, 227, 4190–4206.

Piomelli, U., 1993. High Reynolds number calculations using the dynamics subgrid scale
model. *Phys. Fluids*, 5, 1484–1490.

Piomelli, U., 1999. Large-eddy simulations: achievements and challenges. *Prog. Aero.
Sci.*, 35, 335.

Piomelli, U., Moin, P., and Ferziger, J., 1988. Model consistency in large eddy simulation
of turbulent channel flows. *Phys. Fluids*, 31, 1884.

Pope, S., 2000. *Turbulent Flows*. Cambridge: Cambridge University Press.

Porter, D. and Woodward, P., 1994. High resolution simulations of compressible convec-
tion using the piecewise-parabolic method. *Astrophys. J.*, 93, 309–349.

Pullin, D., 2000. A vortex-based model for the subgrid flux of a passive scalar. *Phys.
Fluids*, 12, 2311–2319.

Pullin, D. and Saffman, P., 1994. Reynolds stresses and one-dimensional spectra for a
vortex model of homogeneous anisotropic turbulence. *Phys. Fluids*, 6, 1787–1796.

Sagaut, P., 2002. *Large-Eddy Simulation for Incompressible Flows*. 2nd Berlin Heidelberg:
Springer-Verlag.

Schlatter, P., Stolz, S., and Kleiser, L., 2004. LES of transitional flows using the approx-
imate deconvolution model. *Int. J. Heat Fluid Flow*, 25 (3), 549 – 558.

Scotti, A. and Meneveau, C., 1999. A fractal model for large eddy simulation of turbulent
flow. *Physica D*, 127, 198–232.

Shah, K.B. and Ferziger, J., 1995. A new non-eddy viscosity subgrid-scale model and
its application to channel flow. *In: CTR Annual Research Briefs 1995* Stanford,
California: Center for Turbulence Research, Stanford University and NASA Ames
Research Center.

Smagorinsky, J., 1963. General circulation experiments with the primitive equations. *Mon. Weath. Rev.*, 93, 99.

Speziale, C.G., 1989. Turbulence modeling in non-inertial frames of reference. *Theor. Comput. Fluid. Dyn.*, 1, 3.

Squires, K.D. and Piomelli, U., 1995. Dynamic modeling of rotating turbulence. *In:* F. Durst, N. Kasagi, B.E. Launder, F.W. Schmidt and J.H. Whitelaw, eds. *Turbulent Shear Flows*, Vol. 9 New York: Springer, p. 73.

Stolz, S. and Adams, N.A., 1999. An Approximate Deconvolution Procedure for Large-Eddy Simulation. *Phys. Fluids*, 11, 1699–1701.

Stolz, S., Adams, N.A., and Kleiser, L., 2001a. An approximate deconvolution model for large-eddy simulation with application to incompressible wall-bounded flows. *Phys. Fluids*, 13, 997–1015.

Stolz, S., Adams, N.A., and Kleiser, L., 2001b. The approximate deconvolution model for LES of compressible flows and its application to shock-turbulent-boundary-layer interaction. *Phys. Fluids*, 13, 2985–3001.

Sweby, P., 1984. High resolution schemes using flux limiters for hyperbolic conservation laws. *SIAM J. Numer. Anal.*, 21, 995.

Tantikul, T. and Domaradzki, J., 2010. Large eddy simulations using Truncated Navier-Stokes equations with the automatic filtering criterion. *J. Turbulence*, 11 (21), 1–24.

van Cittert, P.H., 1931. Zum Einfluß der Spaltbreite auf die Intensitätsverteilung in Spektrallinien II. *Z. Phys.*, 69, 298–308.

Vasilyev, O., Lund, T., and Moin, P., 1998. A general class of commutative filters for LES in complex geometries. *J. Comp. Phys.*, 146, 82–104.

Voelkl, T., Pullin, D., and Chan, D., 2000. A physical-space version of the stretched-vortex subgrid-stress model for large-eddy simulation. *Phys. Fluids*, 12, 1810–1825.

Winckelmans, G.S., *et al.*, 2001. Explicit-filtering large-eddy simulation using the tensor-diffusivity model supplemented by a dynamic Smagorinsky term. *Phys. Fluids*, 13, 1385–1403.

Yang, X. and Domaradzki, J., 2004. Large eddy simulations of decaying rotating turbulence. *Phys. Fluids*, 16, 4088–4104.

Yeung, P. and Zhou, Y., 1998. Numerical study of rotating turbulence with external forcing. *Phys. Fluids*, 10, 2895–2909.

Zalesak, S., 1979. Fully multidimensional flux-corrected transport algorithms for fluids. *J. Comp. Phys.*, 31, 335.

Zhou, Y., Hossain, M., and Vahala, G., 1989. A critical look at the use of filters in large eddy simulations. *Phys. Lett. A*, 139, 330.